Ion Irradiation-Induced Nanoscale Porous Structures in Semiconductors

by

Alejandro Gabriel Pérez-Bergquist

A dissertation submitted in partial fulfillment
of the requirements for the degree of
Doctor of Philosophy
(Nuclear Engineering and Radiological Sciences)
in The University of Michigan
2010

Doctoral Committee:

Professor Lumin Wang, Chair
Professor Michael Atzmon
Professor Gary S. Was
Research Scientist Kai Sun

© Alejandro Gabriel Pérez-Bergquist
2010

To my devoted father, Francisco, my wonderful wife, Sara,

and in loving memory of my mother, Ines.

Acknowledgements

I would like to thank Rackham Graduate School, the Department of Nuclear Engineering and Radiological Sciences, and the US Department of Energy for financial support throughout my schooling. I would also like to thank all my research project collaborators, the staffs of the Electron Microbeam Analysis Laboratory and the Michigan Ion Beam Laboratory, my research group members, and all my family and friends for their personal and professional support. In particular, I would like to thank Dr. Kundar Li for his collaborative efforts on computer modeling studies, Dr. Kai Sun for his continued assistance with electron microscopy techniques, and Professors Michael Atzmon and Gary Was for their insightful comments that improved the quality of this dissertation. Lastly, I would like to give a special thanks to my advisor, Professor Lumin Wang, for his guidance and mentorship throughout my graduate studies.

Table of Contents

Dedication ii
Acknowledgements iii
List of Figures vii
List of Tables xi
List of Appendices xiii
List of Abbreviations xiv
Abstract xvi
Chapter
1. Introduction to Irradiation-Induced Structures and Porous Networks 1
Irradiation-induced Structures 2
Irradiation-induced Nanodots 3
Irradiation-induced Ripples 5
Irradiation-induced Bubbles and Pores 6
Irradiation-induced Void Lattices 8
Irradiation-Induced Porous Networks in Semiconductors 9
Irradiation-Induced Porous Networks in Germanium 11
Irradiation-Induced Porous Networks in Gallium Antimonide 14
Irradiation-Induced Porous Networks in Indium Antimonide 15
Irradiation-Induced Porous Networks in Silicon 17
Amorphization of Irradiated Semiconductors 18
Point Defect Reactions in Crystalline and Amorphous Materials 21
Displacement Reactions in Crystalline Materials 21
Point Defect Reactions in Crystalline Materials 23
Void Growth and Coalescence in Crystalline Materials 25
Point Defects in Amorphous Materials 27
2. Statement of Research Objectives 35
3. Experimental Procedures 38
Sample Irradiation 38
Irradiation Experiments Performed at EMSL 40
Irradiation Experiments Performed at MIBL 41
Irradiation Experiments Performed at EMAL 44
Si MEEVA Experimental Procedures 46
Estimations of Sample Temperature During Irradiation 47
Sample Preparation for Analysis 53
Sample Analysis 57

TRIM Simulations 59
4. Ion Irradiation of GaSb 63
High Energy Ion Irradiation 63
Embedded GaSb Nanofibers 63
Surface Layer Response Under Irradiation 69
FIB Irradiation 73
Surface and Embedded Structures 73
Size and Pattern Control 75
5. Ion Irradiation of Ge 79
High Energy Ion Irradiation 79
Formation of Nanocellular Structures 79
FIB Irradiation 83
Ge Surface Evolution under FIB 83
Size and Pattern Control 85
6. Ion Irradiation of InSb 89
High Energy Ion Irradiation 89
Embedded InSb Nanofibers 89
Surface Layer Evolution Under Irradiation 92
FIB Irradiation of InSb 102
Nanocone Formation 102
7. Ion Irradiation of Si 106
High Energy Ion Irradiation 106
Porous Silicon from High Dose Irradiation 106
Effects of Sputter Shields on Formation of Porous Structures 112
FIB Irradiation of Si 113
Hole Milling and Ripple Formation 113
MEVVA Ion Irradiation 115
Surface Structure Formation and Analysis 115
8. Analysis of Porous Network Formation and Growth 120
Irradiation Parameter-related Effects 120
Influence of Ion Fluence 120
Influence of Atomic Number and Ion Energy 125
Influence of Ion Flux and Implantation Temperature 128
Materials Parameter-related Effects 130
Melting Temperature, Bond Strength, and Displacement Energy 130
Self-Diffusion Rates and Electron/Hole Mobility 131
Porous Network Formation Mechanics in Semiconductors 132
Displacement Cascades and Material Amorphization 132
Vacancy Accumulation and Void Growth 135
Stabilization of Nanostructure 138
9. Materials Properties of Nanoporous Semiconductors 143
Thermally-induced Phase Decomposition of GaSb 144
Core-Shell Nanofiber Analysis 144
Mechanism of Phase Decomposition 150
Optical Properties of Nanoscale Semiconductors 155

Changes in Luminescent Intensity 156
10. Conclusions and Future Work 161
Conclusions 161
Future Work and Implications 165
Future Experimentation 165
Potential Applications for Nanoporous Materials 167
Appendices 171

List of Figures

Figure

1.1 Schematic of an incident ion striking a) a trough versus b) a hillock. 4

1.2 SAED patterns of Ge a) before irradiation and after irradiation with 1.5 MeV Kr^+ ions to a) 1×10^{14} ions/cm^2 and c) 1.2×10^{14} ions/cm^2. 12

1.3 TEM micrographs of porous network formation in amorphous Ge following irradiation at room temperature to doses of a) 7×10^{14}, b) 3×10^{15}, c) 6×10^{15}, d) 1×10^{16}, e) 2×10^{16}, and f) 2.7×10^{16} ions/cm^2. 13

1.4 TEM micrograph of Ge implanted with 200 keV Kr^+ ions to 7×10^{15} ions/cm^2 at room temperature. 13

1.5 2-D schematic of ion irradiation in GaSb. 15

1.6. Temperature dependence of amorphization dose for 1.5 MeV Kr^+-irradiated Ge. 20

4.1 Cross-sectional SEM image of GaSb fiber layers irradiated with 1 MeV Au^+ to 1×10^{14} ions/cm^2. 64

4.2 SEM and TEM images of GaSb fibers. 66

4.3 Nanofiber formation mechanism for higher energy ions, with a 2-D GaSb cross-section shown under ion irradiation. 67

4.4 Plan view SEM images of GaSb irradiated with 1 MeV Au^+ at fluences of a) 1×10^{14} ions/cm^2, b,c) 4×10^{14} ions/cm^2, d) 6×10^{14} ions/cm^2, e,f) and 6×10^{15} ions/cm^2. 70

4.5 Surface layer removal process for 1 MeV Au^+ irradiated GaSb shown in a top-down view. 71

4.6 *In situ* SEM observation of GaSb surface under FIB irradiation with 30 keV Ga^+ ions. 74

4.7 Plan view and XSEM images of GaSb irradiated to a) 1×10^{15}, b) 1.5×10^{15},

and c) 3×10^{15} ions/cm^2. 75

4.8 SEM images of FIB milled GaSb irradiated to ~ 5×10^{15} ions/cm^2. 76

5.1 Plan view SEM image of Ge irradiated with 3 MeV Au^+ ions at a fluence of 1×10^{15} ions/cm^2, resulting in formation of a nanocellular structure. 80

5.2 XSEM images of Ge irradiated with 1 MeV Au^+ ions at ion fluences of a) 1×10^{15}, b) 2×10^{15}, and c) 6×10^{15} ions/cm^2. 81

5.3 TEM images of irradiation-induced Ge fibers fabricated by 1 MeV Au^+ ion irradiation of Ge to a fluence of 2.2×10^{15} ions/cm^2. 82

5.4 Plan view SEM images of Ge irradiated *in situ* with 30 keV Ga^+ to doses of a) 1.875, b) 3.175, c) 5.625, d) 6.25, e) 9.375, f) 18.75, g) 25, and h) 50×10^{15} ions/cm^2. 84

5.5 Ge fibers formed by FIB irradiation. 85

5.6 SEM images of FIB milled Ge irradiated to ~ 2×10^{16} ions/cm^2. 87

6.1 XSEM image of an InSb sample irradiated with 1 MeV Au^+ to a fluence of 1.25×10^{14} ions/cm^2. 90

6.2 TEM images of InSb fibers. 90

6.3 XSEM images of InSb nanofibers after 1 MeV Au^+ irradiation to a) 1.25×10^{14} ions/cm^2 and b) 8.4×10^{14} ions/cm^2 showing fiber size as a function of ion fluence 93

6.4 Plan-view SEM images of InSb samples irradiated with 1 and 3 MeV Au^+ ions. 94

6.5 Plan-view SEM image of an InSb sample irradiated with 3 MeV Au^+ ions to 1×10^{14} ions/cm^2. 94

6.6 XSEM images of the interface between the surface layer and porous layer in InSb samples irradiated with a) 1 MeV and b) 3 MeV Au^+ ions at 5×10^{13} ions/cm^2. 96

6.7 AFM micrographs of InSb surfaces irradiated with a) 1 MeV Au^+ ions at 1.25×10^{14} ions/cm^2 and b) 3 MeV Au^+ ions at 5×10^{13} ions/cm^2. 96

6.8 Porous layer thickness vs. surface roughness for InSb samples exhibiting both a porous layer and a discrete surface layer. 98

6.9 Schematic showing observed porous layer placement and outwards expansion

of energetic ion implantation of InSb as reported by Destefanis *et. al.* 98

6.10 Log-log plot of power spectral densities (PSD) for irradiated InSb with a) 1 MeV Au^+ and b) 3 MeV Au^+ calculated from the images shown in Figure 6.4. 101

6.11 SEM images of InSb irradiated with 30 keV Ga^+ ions at normal incidence to fluences of a) 6.25×10^{15} ions/cm^2, b) 2.5×10^{16} ions/cm^2, c) 9.375×10^{16} ions/cm^2, and d) 1.875×10^{17} ions/cm^2. 102

7.1 Composite XTEM image of Si irradiated with 10 MeV Au^+ to a fluence of 7.8×10^{16} ions/cm^2. 108

7.2 Si implanted with 280 keV Si^+ to ~ 6 - 8 × 10^{18} ions/cm^2 at a surface temperature of ~450°C. 109

7.3 Images of Si nanocaves and related structures. 111

7.4 Plan view SEM images of Si implanted with 280 keV Si^+ to a) 4×10^{18} and b) 8×10^{18} ions/cm^2 with a surface temperature of ~650°C. 112

7.5 a) Plan view and b) XSEM images of Si with a 36 nm SiO_2 surface layer irradiated with 280 keV Si^+ to ~ 8×10^{18} ions/cm^2 at a surface temperature of ~650°C. 113

7.6 Ultra-high dose FIB milled Si. 115

7.7 Plan view SEM images of 40 keV Co^+-irradiated (100) Si at fluences of a) 5×10^{17} ions/cm^2 and b) 1×10^{18} ions/cm^2. 116

8.1 Log-log plot of porous layer thickness versus implantation ion fluence showing near linear relationships between the parameters. 121

8.2 Fiber or cell wall thickness as a function of ion fluence for InSb, GaSb, and Ge irradiated with 1 MeV Au^+ ions. 123

8.3 Vacancy production curves in silicon for 1 MeV a) H^+, b) B^+, and c) Ru^+ ions in terms of vacancies produced per ion per Å as a function of target sample depth. 126

8.4 Vacancy production curves in silicon for 10 keV, 100 keV, 1 MeV, and 10 MeV Si^+ ions in terms of vacancies produced per ion per Å as a function of target sample depth. 127

8.5 Steady-state point defect concentrations in an irradiated solid. 129

8.6 Molten zones in Si, Ge, Al, and Au caused by 10 keV lattice recoils (at left)

and final defects created by the recoils (at right). 134

9.1 Crystallinity and composition of unannealed GaSb fibers. 145

9.2 Crystallinity and composition of annealed GaSb fibers. 147

9.3 SAED pattern of the annealed GaSb nanofiber volume. 149

9.4 GaSb phase diagram, from Reference 7. 150

9.5 Schematic of the core-shell formation mechanism, shown by fiber cross-sections at different intervals of the process. 154

9.6 Luminescent intensity versus photon wavelength for irradiated a) Ge, b) GaSb, c) InSb, and d) Si samples. 157

List of Tables

Table

3.1 Irradiation conditions of samples irradiated at EMSL. 42

3.2 Irradiation conditions of samples irradiated at MIBL. 45

3.3 Irradiation conditions of samples irradiated at EMAL. 46

3.4 Relevant thermal materials properties for Si, Ge, GaSb, and InSb. 48

3.5 Thermal conductivity and diffusivity of Si, Ge, GaSb, and InSb as a function of temperature, given in units of W/mK and $s^{1/2}$/m, respectively. 48

3.6 Relevant thermal materials properties for Si, Ge, GaSb, and InSb where the material is assumed to be 90% porous, resulting in an order of magnitude decrease in density and thermal conductivity. 49

3.7 Thermal conductivity and diffusivity of Si, Ge, GaSb, and InSb as a function of temperature, given in units of W/mK and $s^{1/2}$/m, respectively. 49

3.8 Temperature rise calculations for irradiated Si, Ge, GaSb, and InSb. 50

3.9 Temperature rise calculations for irradiated Si, Ge, GaSb, and InSb using Eq. 3.2. 52

3.10 Materials parameters used for TRIM calculations. 60

3.11 Displacement energies for Si, Ge, GaSb, and InSb. 60

8.1 Porous layer thickness and fiber/cell wall thickness as a function of ion fluence in 1 MeV Au^+ irradiated InSb, GaSb, and Ge. 124

8.2 Material bonding related data for Si, Ge, GaSb, and InSb. 131

8.3 Self-diffusion data and electron hole mobility data for Si, Ge, GaSb, and InSb. 132

9.1 Measured d-spacing values for ring pattern shown in Figure 10.3. 149

9.2 Measured d-spacing values for rhombohedral Sb. 149

List of Appendices

Appendix

1 Irradiation-induced Fiber, Cell Wall, and Pore Sizes 171

2 Porous Layer Thicknesses 177

3 Analysis of GaSb Surface Layers at Increasing Ion Fluence 183

4 Surface Roughness Measurements of Ion Irradiated InSb 186

5 Power Spectral Density Data Acquisition 190

List of Abbreviations

AFM	Atomic Force Microscopy
BCC	Body-Centered Cubic
BF	Bright Field
BH	Bradley-Harper Model
dpa	Displacements per Atom
EDS	Energy Dispersive X-ray Spectroscopy
EELS	Electron Energy Loss Spectroscopy
EMAL	Electron Microbeam Analysis Laboratory
EMSL	Environmental Molecular Sciences Laboratory
FCC	Face-Centered Cubic
FIB	Focused Ion Beam
GIF	Gatan Image Filter
HAADF	High-Angle Annular Dark Field Microscopy
HCP	Hexagonal Close-Packed
HRTEM	High Resolution Transmission Electron Microscopy
IC	Integrated Circuit
LMIS	Liquid Metal Ion Source
MD	Molecular Dynamics

MEMS	Microelectromechanical Systems
MEVVA	Metal Vapor Vacuum Arc
MIBL	Michigan Ion Beam Laboratory
NEC	National Electrostatics Corporation
NSOM	Near-field Scanning Optical Microscopy
PIPS	Precision Ion Polishing System
PKA	Primary Knock-on Atom
PL	Photoluminescence
PNNL	Pacific Northwest National Laboratory
RBS	Rutherford Backscattering Spectrometry
RED	Radiation-Enhanced Diffusion
RT	Room Temperature
SAED	Selected Area Electron Diffraction
SEM	Scanning Electron Microscopy
SHI	Swift Heavy Ions
SIMOX	Separation by Implantation of Oxygen
STEM	Scanning Transmission Electron Microscopy
TEM	Transmission Electron Microscopy
TRIM	Transport and Range of Ions in Matter
XSEM	Cross-sectional Scanning Electron Microscopy
XTEM	Cross-sectional Transmission Electron Microscopy

Abstract

Energetic ion beam bombardment of semiconductors often leads to the development of complex nanostructures at or near the material's surface that self-organize into patterns with well defined dimensions and spatial distributions. These self-organized structures are unique in that their morphologies are dependent upon fundamental properties of the irradiated material, as well as upon the irradiation conditions. Although the formation mechanics behind one- and two-dimensional ion irradiation-induced structures have been well established, the mechanisms behind formation of fully three-dimensional structures are less well understood. In this dissertation, ion irradiation-induced formation of three-dimensional nanoporous structures is studied in four common semiconductors: silicon, germanium, gallium antinomy, and indium antimony. The effects of varying ion energy, number, fluence, and flux, as well as other conditions such as temperature, are studied experimentally via ion irradiation of the materials and subsequent analysis of the microstructure, primarily through electron microscopy techniques. Irradiation conditions are shown to have a direct impact on porous network thickness, depth, and density but very little impact on porous network morphology and irradiation-induced feature size. Using the experimental data, a theoretical analysis of irradiation-induced three-dimensional nanoporous structure formation in semiconductors is presented. Amorphization is found to play a key role in

the nucleation and growth of voids that form the porous structures, as materials that become amorphized via ion irradiation form extensive porous networks at much lower ion fluences and lower homologous temperatures than materials that remain crystalline during irradiation. Melting temperature, bond strength, and atomic displacement energy all show distinct correlations to porous network growth. Two case studies are also presented examining changes in material properties of the irradiation-induced nanostructures due to quantum confinement effects, specifically changes in phase stability of nanofibers and increases in photoluminescence of the nanostructured semiconductors. All nanoscale semiconductor porous networks exhibited a distinct increase in photoluminescent intensity over their unirradiated counterparts within some range of excitation wavelengths.

Chapter 1

Introduction to Irradiation-Induced Structures and Porous Networks

Ion irradiation or implantation is a particle radiation technique whereby atoms are stripped from a material, ionized, electrostatically accelerated to high energy, and then implanted into a target material. Traditionally, ion implantation has been used for two main applications. The first and most widespread application of ion implantation is in semiconductor device fabrication. Probably the most common use of ion implantation is in the introduction of dopant atoms into semiconductor layers. Use of ion implantation allows the introduction of virtually any type of element into any material to very precise concentrations and depths. In addition, numerous semiconductor device manufacturing techniques utilize ion implantation in the creation of novel material phases, such as in mesotaxy, or in the creation of devices with unique material geometries, such as in the fabrication of silicon-on-insulator wafers through the use of the SIMOX (Separation by IMplantation of OXygen) process.

The majority of ion irradiation applications in semiconductor manufacturing, however, actually take advantage of the effects of ion implantation over the effects of ion irradiation, meaning that the resulting process effects are primarily a result of the addition of impurity atoms to the material rather than due to irradiation damage to the material lattice. The other historically important use of ion irradiation has been as an analogue in

the study of other irradiation effects, including neutron damage, electron damage, and nuclear fission. Compared to the direct study of these irradiation processes, ion irradiation has numerous advantages, including the ability to create high density, collimated beams of virtually any ion type, the ability to control the placement of ion damage, and a lack of nuclear activation of the target material, meaning that irradiated samples can be studied without specialized equipment and without radiation safety concerns.

With recent advances in focused ion beam (FIB) technology, as well as an increase in the availability of focused ion beam/scanning electron microscopy (SEM) dualbeam systems, access to ion irradiation equipment has spread dramatically. The rise of dualbeam systems in particular has allowed for much more research into the effects of ion irradiation at the nanoscale, as these systems provide nanometer scale resolution in the use of both the ion and electron beams. With the aid of new technology, much recent research has focused on the effects of ion irradiation at material surfaces as well as in the bulk. In this chapter, a review of ion irradiation-induced nanoscale structures will be given, and a literature review of experimental research in ion irradiation-induced porous networks in semiconductor materials will be given. Also, point defect interactions in crystalline materials will be discussed, and the issue of defining point defects in amorphous materials will be addressed.

1.1 Irradiation-induced Structures

Numerous studies have shown that ion irradiation of materials can produce drastically different results depending on the irradiated material's properties and the

irradiation conditions, such as incident ion energy, atomic number, fluence, flux, angle, and irradiation temperature. Under different conditions, ion irradiation can result not only in lattice damage as described by classical radiation damage theory, but also in the self-formation of one, two, and multi-dimensional structures.

1.1.1 Irradiation-induced Nanodots

The term quantum dots traditionally refers to semiconductors whose excitons are confined in all three spatial dimensions, whereas the term nanodots refers to any material that is similarly spatially confined at the nanoscale. In 1973, Sigmund published a comprehensive, geometrically-based sputtering theory to explain how ion irradiation of a material could cause initially small irregularities on a surface to be enhanced into larger surface perturbations.[1] Using the theory, Sigmund postulated that surface sputtering of a material could lead to the formation of stable cone-like structures. However, Sigmund's theory did not take into account several important mechanisms involved in the sputter formation process, most importantly the effects of diffusion-based migrational smoothening effects and the effects of impurities in sputtered materials.

In 1988, Bradley and Harper expanded upon Sigmund's original theory and combined it with the effects of surface self-diffusion to formulate a theory that included both sputtering-induced roughening effects and diffusion-based smoothening effects.[2] The Bradley-Harper (BH) model describes different results based on the ion irradiation angle, but the case for an incident angle of $\theta = 0°$ (perpendicular incidence) is easily qualitatively understood and is shown in Figure 1.1. Ions striking a surface at either the bottom of a trough (O) or the top of a hillock (O') will deposit the same amount of energy

at either location. However, ions striking the surface near the bottom of a depression (A, B) will deposit more energy at the bottom of the depression (O) than ions striking the surface near the top of a hillock (A', B') will deposit at the top of the hillock (O'). This is shown schematically in Figure 1.1, wherein energy deposition contour lines from A and B are closer to O than contour lines from A' and B' are to O'. This instability in the sputtering rate results in preferential sputtering of low points in the sample topography and leads to the formation of surface nanodots.

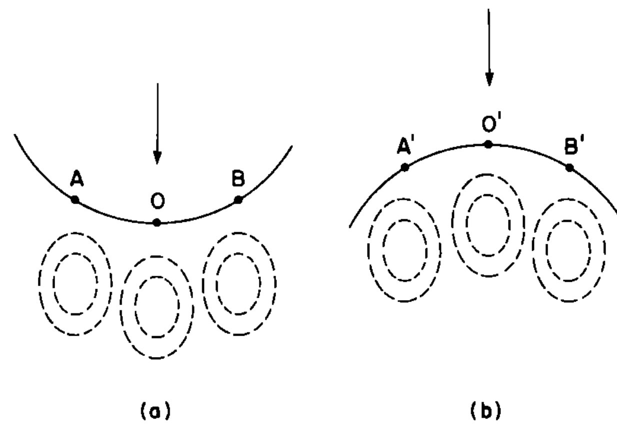

Figure 1.1. Schematic of an incident ion striking a) a trough versus b) a hillock. Dotted lines indicate energy deposition regions for the points listed on the sample surfaces.[2]

Although conclusive experimental evidence of the formation of nanodots by ion sputtering remained elusive for some time,[3] Facsko *et al.* clearly demonstrated the formation of nanodots on the surface of GaSb following perpendicular incidence, low energy Ar^+ ion sputtering.[4] The dot size was shown to depend on the ion fluence, with dot diameters of 18 to 50 nm measured at fluences of 4×10^{17} ions/cm^2 and 4×10^{18} ions/cm^2, respectively, and similar dot patterns were also fabricated in other materials. Numerous studies have since added to the understanding of nanodot formation, adding scaling laws,[5] energy dependencies of dot size,[6] and computer modeling studies,[7] among many others. In addition, irradiation-induced nanodots have been formed through off-

normal irradiation with sample rotation[5] and through off-normal irradiation in stationary samples with certain specific materials characteristics, such as preferential sputtering rates between two elements. For example, gallium droplets of 25 to 70 nm in diameter can be formed by off-normal ion irradiation of GaAs, which results in preferential sputtering of arsenic atoms and subsequent droplet formation and ordering of gallium nanodots.[8]

1.1.2 Irradiation-induced Ripples

Although experimental evidence of ion irradiation-induced ripples[9] far preceded that of ion irradiation-induced nanodots,[6] the foundation of the models for the formation of both ion irradiation-induced ripples and nanodots is rooted in the works of Sigmund[1] and Bradley and Harper.[2] Although the BH model does touch on nanodot formation under the condition $\theta = 0°$, the primary focus of the model is explaining the formation of ripple topographies under off-normal ion irradiation. By combining geometrical sputtering arguments with surface self-diffusion equations, the BH model predicts the dependence on θ for both the ripple orientation and wavelength, with wavelength also being a function of the activation energy for surface self-diffusion. Subsequent studies have since further expanded upon the basic BH model, examining in detail the effects of ion fluence, flux, energy, incidence angle, sample temperature, and surface crystallinity on the growth kinetics of ion irradiation-induced ripple patterns.[10-12] The BH model has been subject to a considerable amount of fundamental research, and recent non-linear extensions of the model have been able to successfully predict saturation and ordering mechanics.[13-14] Although the model is considered a fairly mature science, there are still

some material systems that exhibit unique responses to off-normal ion sputtering that are not explained by the basic BH model and are still currently under research.[8,15]

1.1.3 Irradiation-induced Bubbles and Pores

Irradiation-induced porosity was first observed in the 1950s as a result of the accumulation of fission gases in nuclear fuels.[16] Originally, the swelling of metal uranium fuel due to the accumulation of the fission gases Xe and Kr was considered in the same manner as fuel swelling due to solid fission products, with the movement of fission gases within the fuel pellet described by classical solid diffusion theory.[17] However, examination of the release of fission gases showed significant discrepancies between actual gas release rates and those predicted by diffusion theory, leading to the idea that fission gas atoms could be trapped within the fuel pellets at defect sites.[18] Later experimental studies bombarded UO_2 wafers with electrostatically accelerated Kr^+ ions, and following annealing of the samples, transmission electron microscopy (TEM) clearly showed the widespread presence of small bubbles, where bubbles are defined as pockets within a solid material that contain a measureable internal gas pressure.[19] Similar studies were able to show bubble formation in reactor-irradiated fuels as well. Although the formation of bubbles via production of fission gas is straightforward, the overall behavior of fission gas bubbles is dependent upon a number of factors that are still under study, including but not limited to: the rate of production of fission gas, nucleation of gas bubbles, bubble growth by gas atom migration, resolution of gas atoms into the matrix, bubble migration and coalescence, and fission gas release.[16]

While metal fuels often exhibit bubble formation, ceramic fuels show pore formation during burnup in a nuclear reactor. Whereas fission gas bubbles are generally small in size, with an average diameter of less than a micron, pores in ceramic fuels are large, often with an average diameter of 20 microns or more, and these pores contain a combination of gases, including large amounts of He, small amounts of CO and CO_2, and fission gases Xe and Kr, albeit at a substantially lower gas pressure than that in bubbles.[16] However, the mechanism by which these pores form is fundamentally different than that by which fission bubbles are formed. During fuel fabrication, ceramic fuels are sintered to create fuel pellets, but some level of porosity remains in the pellets even after annealing. Although it would be nearly impossible to achieve 100% of the theoretical density of a ceramic through sintering, some of the porosity left in fuel pellets is intentional, as the pellets are designed to be able to accommodate fission product swelling. When the pellets are placed in a reactor environment, extreme temperature gradients develop across the radius of the pellet, resulting in the center of the fuel pellet reaching temperatures hundreds of degrees hotter than the outer edge. As a result of the high temperature gradient, UO_2 molecules are transported via a vapor-phase transport mechanism to cooler, outer regions of the pellet, while gas molecules diffuse to the hot center of the pellet.[20] Although these large cavities are referred to in the literature as pores, it is important to recall that they do contain gas, and they are formed through primarily thermal means, not directly through irradiation processes.

In addition to bubbles and pores produced through atomic fission in nuclear fuels, bubbles have been formed in a vast variety of other materials through gaseous ion implantation.[21-25] Silicon has received particular attention due to its importance in

electronics manufacturing, and studies have shown that in addition to bubble formation, voids can be formed by following ion implantation with an annealing stage that induces diffusion of the implanted gas species such that the gas is removed from the silicon substrate, leaving only void space behind.[26] Although voids can be produced through auxiliary methods following the production of or implantation of gas atoms into a material, the primary result is the formation of bubbles due to the agglomeration of gas atoms. However, true voids that lack any internal gas pressure can be formed in materials through ion irradiation via an entirely different formation mechanism, one that relies on atomic damage to the target material lattice.

1.1.4 Irradiation-induced Void Lattices

In 1967, Cawthorne and Fulton observed the formation of voids in stainless steels irradiated with fast neutrons at high fluences and at elevated temperature.[27] Although bubbles had been seen in irradiated stainless steels before, their origin could be explained through the formation and accumulation of He during (n, α) reactions, while the observed voids could not be explained by the accumulation of He or other gasses. Instead, the presence of these voids was qualitatively explained by extrapolation of point defect reactions. Since neutron irradiation was known to create large numbers of vacancies in materials, voids seemingly could be formed by accumulation of these vacancies.

Shortly thereafter, Evans observed the formation of ordered void lattices in 2 MeV N^+ irradiated Mo at high temperature and high fluences.[28] TEM examination of the irradiated foils showed that voids formed in ordered body-centered cubic (BCC) lattices. Although the reason for the ordering was immediately unclear, free energy considerations

were proposed as a possible driving force for the ordering mechanism. Subsequent studies have shown similar void formation and ordering in other BCC metals such as Nb,[29] as well as face-centered cubic (FCC) metals such as Ni,[30] and hexagonal close-packed (HCP) metals such as Mg.[31] BCC metals experience void growth at damage levels of as little as a few displacements per atom (dpa), with more fully ordered structures requiring about 30 dpa. FCC metals require much larger damage levels, such as about 400 dpa in the case of Ni. The void lattices also form across a wide range of temperatures, although ordered lattices are most easily formed at temperatures just below the peak swelling temperature. Typically the void lattice parameter is about two orders of magnitude larger than the atomic lattice parameter, with a notable dependence on both the irradiation dose and temperature.[32] Analytical and computational models have been developed to explain the growth and ordering of the void lattice superstructures, including, but not limited to, elastic energy minimization models, which describe void organization as a function of elastic interactions between voids,[33,34] and self-interstitial atom preferential migration models, which explain void organization due to preferential migration of interstitial atoms to voids that are not aligned along crystallographic directions of the material.[35,36] Recently, phase-field models have been used to try to model void formation and self-organization.[37,38] Although models match fairly well with experimental observations, work is still underway to explain inconsistencies in the data.

1.2 Irradiation-Induced Porous Networks in Semiconductors

Like metals, semiconductors irradiated with energetic particles can experience widespread void formation and growth, but unlike metals, irradiation-induced void

structures in semiconductors vary drastically from material to material and generally have no recognizable order. These irradiation-induced porous structures are unique for a number of reasons. To begin with, these highly porous structures have only been observed in irradiated semiconductors which were either initially amorphous or became amorphized due the ion irradiation process, a stark difference from metallic void lattices which have only been observed in crystalline materials. These porous networks also can be formed embedded within the target material, indicating that their formation is a bulk process and not merely a diffusion- and sputtering-controlled surface process like the formation of nanodots and nanoripples. Finally, due to the small feature sizes of the porous networks and their ability to be formed in semiconductors, these irradiation-induced structures are prime candidates for optoelectronic applications that require materials to be quantumly-confined, such as in silicon lasers.

While the formation mechanisms for these structures are still not fully understood, there have been a large number of experimental studies investigating the structure, morphology, crystallinity, and composition of these irradiation-induced porous networks. Traditionally, research in this area has focused on the two most historically important pure semiconductors, silicon and germanium, as well as two III-V semiconductors that have shown an extreme affinity for porous structure formation, GaSb and InSb. In the following sections, literature on irradiation-induced porous structures in these four semiconductors is reviewed, as well as topics related to amorphization of these materials as a function of dose and temperature.

1.2.1 Irradiation-Induced Porous Networks in Germanium

Irradiation-induced void structures in Ge were first reported and studied by Wilson[39] while trying to research the effects of perpendicular-incidence ion sputtering as described by Sigmund.[1] Following self-ion bombardment near room temperature and ion energies of 30 to 500 keV, instead of forming surface cone structures as predicted by Sigmund's sputtering theory, Wilson found that the Ge near-surface region degenerated into a porous, cellular structure. SEM analysis clearly showed that the surface had expanded outwards and formed a network of intertwining cells, with void space in-between. While the cell diameter appeared to be a function of the ion dose, with cell diameter saturating at higher fluences, Wilson reported no obvious relationship between the cell size and ion energy. Thickness of the damaged layer also showed a clear relationship to incident ion fluence with no obvious saturation. Although no model was proposed to explain the structure formation, it was assumed that the structures formed due to the accumulation of excess vacancies in the material resulting from nuclear collisions in the target material, and the combined effects of radiation damage swelling, sputtering, and redeposition led to the unique porous structure.

Subsequent selected area electron diffraction (SAED) studies performed in a TEM confirmed that the porous Ge networks formed only in regions amorphized by the ion beam.[40] Implantations performed above the amorphous-crystalline transition temperature of Ge (~350°C), did not produce porous regions, again indicating that the amorphization of the Ge target was critical to the formation of the porous structure.[39,40] Additionally, porous layers were formed underneath Al surface layers, showing both that the structures

are not purely an effect of sputtering and that free surfaces are not necessary for the restructuring to occur.[41]

In-situ TEM ion irradiation studies provided further insight into the formation and organization of the structures, giving further evidence that the porous networks formed only following amorphization of the Ge crystal.[42,43] Figure 1.2 shows SAED patterns of 1.5 MeV Kr^+-irradiated Ge, and Figure 1.3 shows TEM micrographs of 1.5 MeV Kr^+-induced porous Ge microstructures. As can be seen by comparing the fluences of amorphization and porous network formation, it is clear that amorphization of the Ge target precedes void formation. *In situ* irradiation of Ge with 200 keV Kr^+ ions also provided evidence that the porous structure were not formed by bubbles, as TEM imaging revealed that small Kr bubble formation was only evident following formation of the larger overall porous Ge structure, shown in Figure 1.4.[43] A later study using swift heavy ions (SHI), defined as ions with energy greater than 1 MeV/amu, showed that the porous Ge structures could be embedded at depths of several microns within the sample without causing any noticeable atomic damage to the surface.[44] Although intermittent publications on irradiation-induced Ge have continued to surface, no comprehensive models for the formation of the cellular structures have been published.

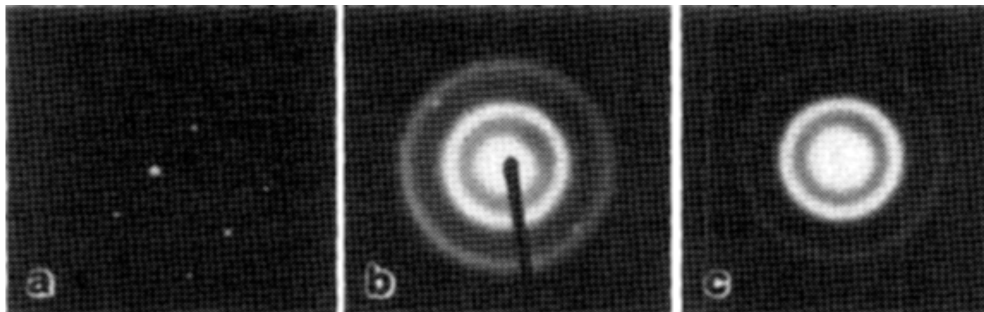

Figure 1.2. SAED patterns of Ge a) before irradiation and after irradiation with 1.5 MeV Kr^+ ions to a) 1×10^{14} ions/cm^2 and c) 1.2×10^{14} ions/cm^2.[42]

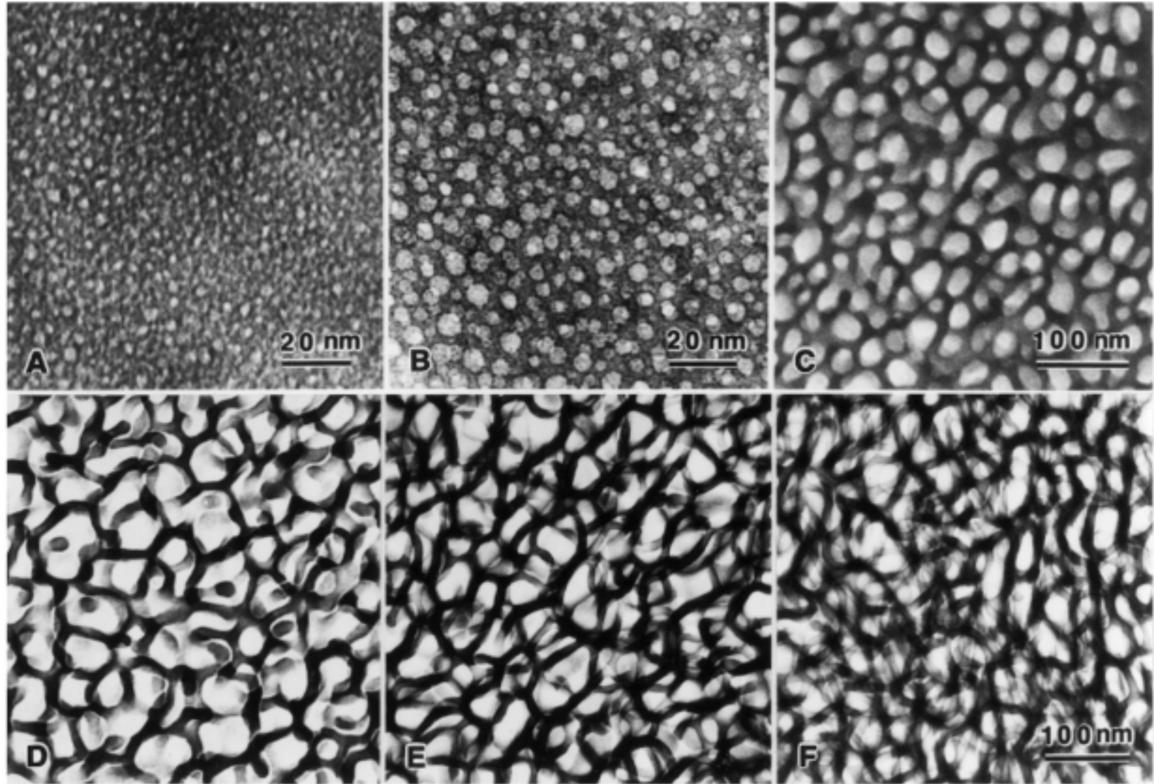

Figure 1.3. TEM micrographs of porous network formation in amorphous Ge following irradiation at room temperature to doses of a) 7×10^{14}, b) 3×10^{15}, c) 6×10^{15}, d) 1×10^{16}, e) 2×10^{16}, and f) 2.7×10^{16} ions/cm^2.[43]

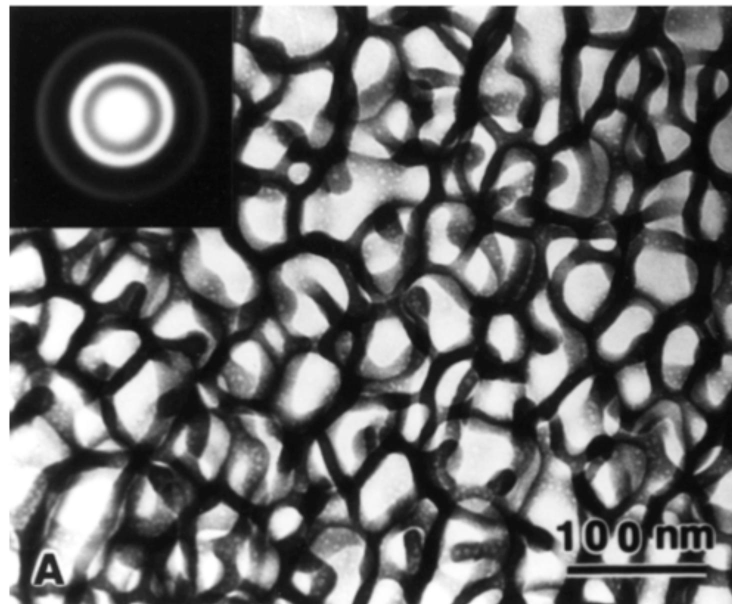

Figure 1.4. TEM micrograph of Ge implanted with 200 keV Kr^+ ions to 7×10^{15} ions/cm^2 at room temperature. Inset shows the corresponding SAED pattern. Small Kr bubbles can be seen in the overall porous Ge network, indicating that bubble formation is a separate and distinct process from porous network formation.[43]

1.2.2 Irradiation-Induced Porous Networks in Gallium Antimonide

The first evidence of ion-irradiation induced porous structures in GaSb were reported in 1957 when GaSb samples irradiated with 9 MeV deuterons were seen to experience an elevation of their surface above that of the unirradiated regions, so noticeable in fact that it was visible with the naked eye.[45] However, despite visual SEM evidence of the structures,[46] no true follow-up work was performed until more than 30 years later when Callec *et al.* performed a specific study of the swelling phenomenon in GaSb, irradiating GaSb wafers with a variety of ions at energies of 50 to 300 keV and fluences of up to 1×10^{16} ions/cm^2.[47] Cross-sectional SEM showed a substantial outward expansion of the irradiated region, which had evolved into a porous, sponge-like layer. The thickness of the porous layer was a function of the ion dose, and no saturation of the layer thickness was seen even at a fluence of 1×10^{16} ions/cm^2. A subsequent TEM investigation of the swelling phenomenon reported that at low fluences corresponding to the void formation threshold, the irradiated region remained single crystalline, while at higher fluences with more well developed pore structures, the SAED pattern indicated that the porous layer was in fact polycrystalline, a distinct difference from observations in Ge.[48] Further TEM investigations conflict with these observations, providing higher resolution SAED analysis showing that at moderate doses the fibers are polycrystalline, but at higher doses corresponding to more well developed structures, the cell walls are amorphous.[49] Other studies have confirmed that the nanofibers appear to be partly amorphous and partly nanocrystalline.[50]

Although a number of publications had provided insight into the formation of ion-irradiation induced porous GaSb nanostructures, Nitta *et al.* introduced a more

comprehensive qualitative model than previously available.[49] The formation model, shown schematically in Figure 1.5, explains a multi-stage process leading to the development of porous surface structures. The model postulates that initially, point defects are created by ion implantation and that interstitial atoms, which are fairly mobile, diffuse to defects and to the surface, leaving large concentrations of vacancies in the near-surface region. These vacancies coalesce into voids, with additional vacancies diffusing into the voids, thus causing them to grow. Additional interstitial point defects migrate to the cell walls (or nanofibers), causing elongation of the cell walls and causing the overall porous region to continue to swell. The model also postulates that voids will inevitably burst at the surface, either through void growth into the surface or through removal of the surface due to irradiation effects, such as sputtering. As in the case of Ge, although improvements to the qualitative formation model have been made,[51] no comprehensive numerical models exist.

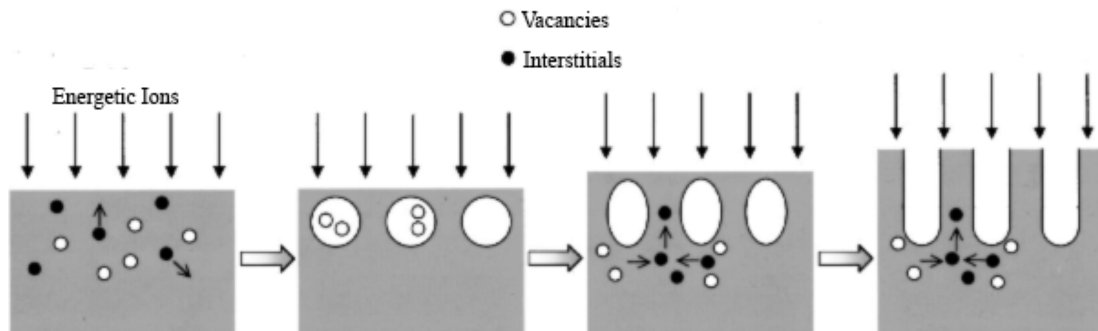

Figure 1.5. 2-D schematic of ion irradiation in GaSb. Incoming ions form point defects, of which interstitials are able to migrate and vacancies agglomerate into voids. Continued creation of point defects causes growth of voids and elongation of cell walls.[49]

1.2.3 Irradiation-Induced Porous Networks in Indium Antimonide

Similar to GaSb, ion irradiation-induced porous InSb structures were also first reported in 1957 in Kleitman's work, which merely reported an elevation of the surface

following irradiation.[45] The first true in-depth study of the InSb structures was performed by Destefanis and Gailliard, who performed TEM and SEM studies of InSb wafers irradiated with a variety of ions at energies of 30 to 300 keV and fluences of up to 1×10^{16} ions/cm^2.[52] Imaging confirmed a spongelike, porous structure after irradiation, containing pores of tens of nanometers in diameter. The porous layer was shown to expand with both increasing ion dose and energy, with no real saturation evident at the maximum dose and energy tested. In addition, a novel formation mechanism was hypothesized in which thermal expansion of small zones due to thermal spike heating could be responsible for the deformation of the target material. A follow-up work slightly expanded on the primary features of void formation but mainly focused on data that showed that the overall expansion of the porous layer was a function of the total energy density deposited by incoming ions.[53] Despite the novel formation mechanism proposed by Destefanis and Gailliard, further experimentation using Rutherford backscattering spectrometry (RBS) and channeling measurements indicated that the expansion of the near-surface was a result of the agglomeration of point defects caused by ion damage, and changes in the implantation temperature were shown to change the point defects kinetics such that at low (liquid nitrogen) or high temperature implantations, no swelling could be detected.[54]

Also of note are the effects of ion irradiation on the surface morphology of InSb. While ion-irradiated Ge and GaSb exhibit unique surface structures, the surface morphology is directly related to the structure of the porous layer, whereas there is some evidence to show that InSb surfaces behave differently under irradiation. A reactive ion etching experiment where InSb was irradiated with 500 eV ions to a high dose of 1.5 ×

10^{18} ions/cm^2 resulted in a vast increase of the surface roughness of the substrate, despite not forming a noticeable porous layer,[55] and another instance in which porous InSb was fabricated using 1 MeV ions, a buckled surface layer was reported.[56] No further research has been performed into this phenomenon, however.

1.2.4 Irradiation-Induced Porous Networks in Silicon

Despite the fact that silicon is by far the most heavily used and researched material in the semiconductor industry, evidence of ion irradiation-induced porous networks in silicon has been elusive. Although there have been numerous studies showing that pores can be fabricated in silicon by implantation of He, which creates bubbles, followed by an annealing stage to out-diffuse the gas,[24-26] there have been very few studies showing the creation of voids without implantation of a gaseous ion species. Romanov and Smirnov reported small voids in Si following 100 keV P^+ irradiation at room temperature, but the voids were sparsely distributed and did not resemble the extended porous networks that have been reported in other semiconductor materials.[57] In addition, the voids only appeared following annealing at temperatures of 400 to 800°C, which is above the evaporation point of phosphorus, drawing into question whether or not the reported voids were in fact phosphorus bubbles. Although the voids were reported to cluster at annealing temperatures of 700°C, they were also reported to disassociate completely above 800°C.

Ion irradiation-induced porous structures that even remotely resemble those seen in Ge and GaSb have only recently been reported by Zhang *et al.*[58] Following 40 keV Co^+ implantation of crystalline (111) and (100) silicon to fluences of up to 2.8×10^{18}

ions/cm^2 and at beam currents in excess of 50 μA/cm^2, porous surface structures were observed. While Ge, GaSb, and InSb form porous networks at fairly low ion doses, Si exhibited no changes in surface topography at 1×10^{17} ions/cm^2, but at a fluence of 5×10^{17} ions/cm^2, roughly a 50% surface pore coverage was visible. Rather than forming densely intertwining porous networks, however, the Si structures exhibited numerous individual, columnar pores. Annealing tests performed at high temperature showed that the developments of the porous, columnar structures was due to ion implantation effects and not due to grain growth of cobalt silicides induced by the implantation of ions. In another recent publication, SHI were implanted into fully amorphous Si, resulting in a large step height increase of the surface,[59] similar to those originally reported in ion-implanted antimonides.[45] Although this step height increase was attributed to the formation of a porous layer due to irradiation effects, no microscopy or other analytical studies were performed to confirm the verdict.

1.2.5 Amorphization of Irradiated Semiconductors

One common factor in the formation of irradiation-induced porous networks in the four semiconductors discussed in the previous sections is the lack of evidence of porous structure formation in single-crystalline materials. In all reported cases of porous network formation in Ge, GaSb, InSb, and Si, the target has either become amorphized by ion irradiation (such as in Ge), become partially amorphized by ion irradiation (such as in GaSb and InSb), or was fully amorphous to start with (such as in Si). This is a clear departure from observed behavior in metals, which are extremely difficult to amorphize via ion irradiation and only form porous structures, specifically void lattices, in materials

that are fully crystalline. While this observation that partial or complete amorphization of the target material may be necessary for porous network formation is useful in itself, it also serves as a useful indicator in determining temperature regimes in which porous network formation may be possible.

It is well established in the literature that crystalline materials subject to irradiation possess an intrinsic critical amorphization dose above which the material will become amorphous.[60] This critical amorphization dose is dependent upon a number of factors, including irradiation particle atomic number, energy, and sample temperature. While the amorphization dose is a fairly weak function of ion energy,[61] increasing ion atom number can result in increases to the critical amorphization dose of several orders of magnitude.[62] Temperature is arguably the most important factor in the critical amorphization dose, as each material generally has a temperature above which irradiation-induced amorphization is not possible. Amorphization as a function of temperature in irradiated Ge was first studied by Wang and Birtcher, who found that Ge samples irradiated with 1.5 MeV Kr^+ did not amorphize at a sample temperature of 300°C, as shown in Figure 1.6.[43] Similar studies have shown that amorphization will not occur above ~280°C in Si irradiated with 300 keV Sb^+ ions, and the critical amorphization temperature is even lower for implantation with lighter ions such as B^+ or P^+.[62,63] Electron beam irradiation experiments in GaSb showed an inability of the material to amorphize above ~30°C, but due to the difference in interaction cross-section between electrons and ions, this experiment does not provide useful data concerning the temperature dependence of the critical amorphization dose in GaSb for ion irradiation.[64] Although no specific studies of critical amorphization dose as a function of temperature

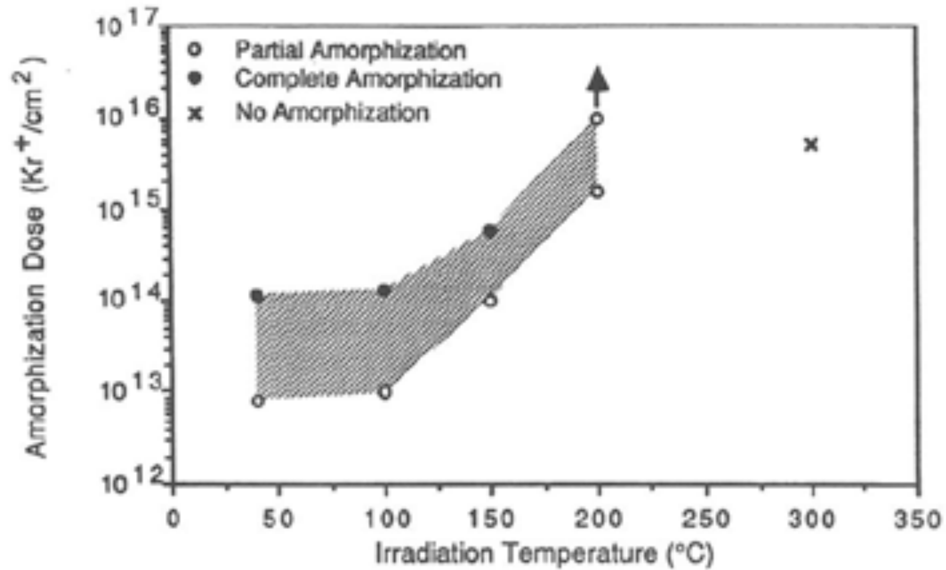

Figure 1.6. Temperature dependence of amorphization dose for 1.5 MeV Kr^+-irradiated Ge.[43]

have been performed for either GaSb or InSb under ion irradiation, porous network formation was noted to be severely limited in GaSb irradiated with 3.4 MeV Ga^+ ions at 220°C, perhaps indicating a correlation to the critical amorphization dose.[50]

It should also be noted that while energetic ion irradiation of single-crystalline semiconductors generally results in amorphization, ion irradiation-induced poly-crystallization can also occur.[65] Irradiation-induced poly-crystallization generally results in the formation of nanoscale microstructures similar to those seen in annealed amorphous materials, and the fact that poly-crystallization has been observed to occur near the critical amorphization temperature but below the normal recrystallization temperature of a material indicates that materials are influence both by the competing effects of irradiation-induced amorphization and by thermally-induced crystalline recovery.

1.3 Point Defect Reactions in Crystalline and Amorphous Materials

When energetic particles interact with solids, the incoming particles lose their kinetic energy through a series of two-body atomic collisions with target atoms and through electronic excitation of the electrons in the solid, and it is through these ion-solid interactions that defects are created in an irradiated material. Of primary interest for damage creation in metals and semiconductors are the elastic collisions, which lead to the formation of Frenkel pairs, which consist of an atomic vacancy and a self-interstitial atom.[66] In a crystalline material, a vacancy is defined as an atom missing from a lattice site, while a self-interstitial is defined as an atom occupying a lattice site that normally does not contain an atom. In amorphous materials, however, the traditional definitions of vacancies and interstitials are incongruous due to the lack of a crystal lattice. As such, point defects must be described differently in amorphous materials. In this section, the fundamental aspects of void swelling in crystalline solids are reviewed, including point defect formation, diffusion-driven point defect reactions, and void swelling and coalescence, while the issue of describing point defect interactions in amorphous materials is also discussed.

1.3.1 Displacement Reactions in Crystalline Materials

The atomic displacement process begins with the collision of an incoming particle, in this case ions, with a primary knock-on atom (PKA), which is defined as the first atom struck by an incoming particle. If the energy imparted to the PKA is sufficiently high, then the PKA can leave its lattice position and collide with other lattice atoms, in turn creating more atomic displacements. The resulting sequence of

displacements is commonly referred to as a collision or displacement cascade, and the number of atoms displaced in a collision cascade can be represented by the damage function, $N_d(E)$, where E is the energy of the PKA.[67]

The simplest calculation of the damage function is based on the hard-sphere model of Kinchin and Pease, which makes the following assumptions:[16,68]

1) The collision cascade consists of a series of two-body collisions between like atoms.
2) All collisions are assumed to be elastic, and electronic energy loss is ignored below a cutoff energy E_c
3) The energy transfer probability is given by the hard-sphere model:

$$P(E,T)dT \cong \frac{dT}{\gamma E} = \frac{dT}{E} \tag{1.1}$$

   where E is the energy of the PKA, T is the energy transferred to the recoil, and γ is the ratio of M_1 to M_2, which equals 1 for like atoms.
4) The displacement probability of an atom is assumed to be a step function, where an atom requires a minimum energy E_d to be displaced from a lattice site and must receive energy greater than $2E_d$ to create further displacements.
5) The energy E_d that is consumed in displacing an atom is neglected in the energy balance of the binary collision transferring energy to the recoil atom.
6) Effects due to crystal structure are neglected.

The total Kinchin and Pease PKA damage function can be stated as:

$$N_d(E) = \begin{cases} 0 & (\text{if } E < E_d) \\ 1 & (\text{if } E_d < E < 2E_d) \\ \dfrac{E}{2E_d} & (\text{if } 2E_d < E < E_c) \\ \dfrac{E_c}{2E_d} & (\text{if } E < E_c) \end{cases} \quad (1.2)$$

Improvements to the Kinchin and Pease model have been made that incorporate more realistic atomic interaction potentials and include the effects of electronic excitation, resulting in a more accurate displacement model:[69,70]

$$N_d(E) = \begin{cases} 0 & (\text{if } E < E_d) \\ 1 & (\text{if } E_d \le E < \dfrac{2E_d}{\xi}) \\ \dfrac{\xi v(E)}{2E_d} & (\text{if } \dfrac{2E_d}{\xi} \le E < \infty) \end{cases} \quad (1.3)$$

ξ is a constant that is dependent upon the interaction potential, which computer simulations suggest has a value near 0.8, and *v(E)* is the amount of energy of the PKA not lost to electronic excitation, commonly referred to as the damage energy. An approach to calculation of the damage energy is given in Reference 70. Overall, application of the modified Kinchin and Pease model gives a good estimate of the displacements, and consequently the number of vacancies and interstitials, created in an irradiated solid.

1.3.2 Point Defect Reactions in Crystalline Materials

Although ion irradiation of a solid results in the generation of large quantities of point defects, a number of mechanisms act to reduce point defect concentrations, including recombination of vacancies and interstitials and migration of point defects to sinks of various forms. Both recombination and migration of point defects are diffusion driven processes, depending upon temperature and defect concentration. Assuming that

only point defects are generated during ion irradiation, the concentrations of defects as a function of time can be expressed as:[71]

$$\frac{dC_v}{dt} = K_d + K_{th} - D_v C_v k_v^2 - \alpha C_i C_v$$
$$\frac{dC_i}{dt} = K_d - D_i C_i k_i^2 - \alpha C_i C_v \tag{1.4}$$

where K_d is the atomic displacement rate, K_{th} is the rate of thermal vacancy generation, D_v and D_i are the diffusion coefficients, C_v and C_i are the atomic concentrations, and k_v^2 and k_i^2 are the sink strengths for vacancies and interstitials, respectively. α is the vacancy-interstitial recombination coefficient and is equal to $4\pi(D_v + D_i)/d^2$, where d is the atomic jump distance, which is a function of the size of the crystal lattice. Furthermore, the atomic diffusion coefficients can be given by:[67]

$$D_i = \frac{d^2}{6} e^{-(\frac{E_m^i}{k_B T})} \tag{1.5}$$

$$D_v = \frac{d^2}{6} e^{-(\frac{E_m^v}{k_B T})}$$

E_m^i and E_m^v are the interstitial or vacancy migration energy, k_B is the Boltzman constant, and T is the temperature. Assuming that dislocations and voids are the only sinks for point defects, the sink strengths can also be defined as:

$$k_i^2 = 4\pi \bar{r}_v \rho_v + S_i \rho_d \tag{1.6}$$

$$k_v^2 = 4\pi \bar{r}_v \rho_v + S_v \rho_d$$

where $\bar{r}_v$ is the mean void radius, ρ_v is the void number density, S_x is the dislocation sink strength for interstitials and vacancies, and ρ_d is the dislocation line density.

Eq. 2.4 can be used to calculate steady state defect concentrations, which in turn can be simplified for different temperature regimes. At high temperature, the thermal

vacancy concentration is large and defect mobilities are high, resulting in a system relatively unaffected by irradiation. At intermediate temperatures where K_{th} is lower than K_d, irradiation induced vacancies and interstitials begin to dominate diffusion processes. In this range, migration to sinks will be the primary mechanism for defect loss, and steady-state defect concentrations can be approximated by:

$$C_i^{SS} = \frac{K_d}{D_i k_i^2} \qquad (1.7)$$

$$C_v^{SS} = \frac{K_d}{D_v k_v^2}$$

where SS refers to steady-state. At low temperatures, defect mobilities and thermal vacancy concentrations are low, so that K_{th} and losses to sinks can be neglected, resulting in defect concentrations of:

$$C_i^{SS} = \sqrt{\frac{K_d D_v}{\alpha D_i}} \qquad (1.8)$$

$$C_v^{SS} = \sqrt{\frac{K_d D_i}{\alpha D_v}}$$

Although the steady state equations provide insight into the behavior of vacancies and interstitials in an irradiated solid, integration of Eq. 2.4 is necessary for conditions of variable temperature or sink strength, as in the case of void growth.

1.3.3 Void Growth and Coalescence in Crystalline Materials

Certain conditions are necessary for void swelling to occur in an irradiated solid. First, both interstitials and vacancies must be mobile, otherwise recombination reactions will dominate. Point defects must be capable of annihilation at sinks, and there must be a preferential removal of interstitials at some of the sinks to allow for a vacancy excess to

form. In crystalline materials, dislocations act as preferential sinks for self-interstitial atoms. Finally, the supersaturation of vacancies in the solid must be large enough to allow for the nucleation and growth of voids.[16]

Given the proper formation conditions, the growth rate of a void is determined by the net influx of vacancies to a void per unit time:[72]

$$\frac{dr_v}{dt} = \frac{\Omega}{r_v}\{Z_v^v(r_v)D_v[C_v - C_v^e(r_v)] - Z_i^v(r_v)D_iC_i\} \tag{1.9}$$

where r_v is the void radius, Ω is the atomic volume, and Z_v^v and Z_i^v are the capture efficiencies for vacancies and interstitials at voids. Although the values for Z_v^v and Z_i^v are close to unity, more detailed values can be calculated as outlined in References 73 and 74. $C_v^e(r_v)$ is the thermal vacancy concentration for a void of radius r_v and is given by:

$$C_v^e(r_v) = C_v^e e^{(\frac{2\gamma}{r_v} - P_g)\frac{\Omega}{k_BT}} \tag{1.10}$$

where C_v^e is the bulk thermal vacancy concentration, γ is the surface tension, and P_g is the gas pressure in the void. As with point defect diffusion reactions, generalizations can be made about void growth under different regimes. In a recombination dominant system, void growth rate depends on the square root of the point defect generation rate, whereas in a sink dominated system, there is a linear proportionality, showing that point defect mobility is crucial to void growth.[72]

In addition to growth by vacancy accumulation, voids are susceptible to growth by coalescence. Although coalescence due to diffusional motion of voids is possible, experimental evidence indicates that the majority of void coalescence is due to mutual impingement due to void growth. In the absence of internal gas pressure, coalescence of voids becomes a simple matter of conservation of volume and is dictated by void

distributions in the irradiated target material. For a more complete analysis of void growth and coalescence in irradiated solids, including a full numerical analysis of void growth and void size distributions during coalescence, see Reference 72.

1.3.4 Point Defects in Amorphous Materials

Since amorphous materials lack crystalline structure, point defects cannot be described by their traditional definitions in amorphous solids, but multiple methods of defining point defects have been proposed throughout the literature. Spaepen considered the idea of structural imperfections in amorphous metals, where imperfections were defined as "deviations in the structure of the actual glass from that of the fully relaxed glass at 0 K."[75] For example, a 2D model of an amorphous solid was developed where vacancies-like defects were created by picking out hard spheres from a system of hard spheres in motion, which was used to model relaxation of nearby atoms. Structural defects in amorphous solids have also been defined in terms of internal stresses between atoms.[76]

In the most general sense, point defects in crystalline materials are merely atoms removed from lattice sites or introduced into new lattice sites. Similarly, point defects can be described very much the same way in amorphous materials, with vacancies described as atoms instantaneously removed from a localized special region and self-interstitials defined as atoms instantaneously introduced to a localized special region. This approach was used by Chaki and Li in a molecular-dynamics simulation of radiation damage in an amorphous solid and has also been used in similar simulations.[77,78] Alternatively, instead of considering individual defects, vacancy and interstitial concentrations in amorphous

materials have also been described by changes in density of localized regions.[79,80] Despite many proposed methods for dealing with vacancies and interstitials in amorphous materials, it is important to note that there is no real consensus on how to define point defects in amorphous materials. Subsequently, theories describing point defect generation and diffusion rates in amorphous materials are very much a subject of current research and debate.

Bibliography

1. P. Sigmund, A Mechanism of Surface Micro-roughening by Ion Bombardment. *J. Mater. Sci.* **8**, 1545 (1973).

2. R. M. Bradley and J. M. E. Harper, Theory of Ripple Topography Induced by Ion Bombardment. *J. Vac. Sci. Technol. A* **6**, 2390 (1988).

3. G. Carter and V. Vishnyakov, Roughening and Ripple Instabilities on Ion-bombarded Si. *Phys. Rev. B* **54**, 17647 (1996).

4. S. Facsko, T. Dekorsy, C. Koerdt, C. Trappe, H. Kurz, A. Vogt, and H. L. Hartnagel. Formation of Ordered Nanoscale Semiconductor Dots by Ion Sputtering. *Science* **285**, 1551 (1999).

5. F. Frost, A. Schindler, and F. Bigl, Roughness Evolution of Ion Sputtered Rotating InP Surfaces: Pattern Formation and Scaling Laws. *Phys. Rev. Lett*. **85**, 4116 (2000).

6. S. Facsko, H. Kurz, and T. Dekorsy, Energy Dependence of Quantum Dot Formation by Ion Sputtering. *Phys. Rev. B* **63**, 165329 (2001).

7. B. Kahng, H. Jeong, and A.-L. Barabási, Quantum Dot and Hole Formation in Sputter Erosion. *Appl. Phys. Lett.* **78**, 805 (2001).

8. Q. M. Wei, J. Lian, W. Lu, and L. M. Wang, Highly Ordered Ga Nanodroplets on a GaAs Surface Formed by a Focused Ion Beam. *Phys. Rev. Lett*. **100**, 076103 (2008).

9. A. D. G. Stewart and M. W. Thompson, Microtopography of Surfaces Eroded by Ion-Bombardment. *J. Mater. Sci.* **4**, 56 (1969).

10. E. Chason, T. M. Mayer, B. K. Kellerman, D. T. McIlroy, and A. J. Howard, Roughening Instability and Evolution of the Ge (001) Surface during Ion Sputtering. *Phys. Rev. Lett.* **72**, 3040 (1994).

11. M. A. Makeev, R. Cuerno, and A. L. Barabasi, Morphology of Ion-sputtered Surfaces. *Nucl. Instrum. Methods Phys. Res. B* **197**, 185 (2002).

12. A.-D. Brown and J. Erlebacher, Temperature and Fluence Effects on the Evolution of Regular Surface Morphologies on Ion-sputtered Si(111). *Phys. Rev. B* **72**, 075350 (2005).

13. S. Facsko, T. Bobek, A. Stahl, H. Kurz, and T. Dekorsy, Dissipative Continuum Model for Self-organized Pattern Formation During Ion-beam Erosion. *Phys. Rev. B* **69**, 153412 (2004).

14. M. Castro, R. Cuerno, L. Vázquez, and R. Gago, Self-Organized Ordering of Nanostructures Produced by Ion-Beam Sputtering. *Phys. Rev. Lett.* **94**, 016102 (2005).

15. S. Le Roy, E. Barthel, N. Brun, A. Lelarge, and E. Søndergard, Self-sustained Etch Masking: A General Concept to Initiate the Formation of Nanopatterns During Ion Erosion, *J. Appl. Phys.* **106**, 094308 (2009).

16. D. R. Olander, *Fundamental Aspects of Nuclear Reactor Fuel Elements*. (Technical Information Center, Office of Public Affairs, Energy Research and Development Administration; USA, 1976).

17. J. A. Brinkman, *Nuclear Metallurgy*. (American Institute of Mining, Metallurgy & Petroleum Engineering; New York, 1959).

18. J. R. MacEwan and P. A. Morel, Migration of Xenon Through a UO_2 Matrix Containing Trapping Sites. *Nucl. Appl.* **2**, 158 (1966).

19. R. M. Cornell and G. H. Bannister, *Proc. Brit. Ceram. Soc.* **7**, 355 (1967).

20. P. F. Sens, The Kinetics of Pore Movement in UO_2 Fuel Rods. *J. Nucl. Mater.* **43**, 293 (1972).

21. D. J. Reed, Review of Recent Theoretical Developments in Understanding of Migration of Helium in Metals and its Interaction with Lattice-Defects. *Radiat. Eff.* **31**, 129 (1977).

22. S. M. Meyers, D.M. Follstaedt, H. J. Stein, and W. R. Wampler, Hydrogen Interaction with Cavities in Helium-Implanted Silicon. *Phys. Rev. B* **47**, 13380 (1993).

23. S. M. Myers, H. J. Stein, and D. M. Follstaedt, Hydrogen Interaction with Cavities in Helium-Implanted Germanium. *Phys. Rev. B* **51,** 9742 (1995).

24. G. Lulli, P. G. Merli, A. Migliori, G. Brusatin, and A. V. Drigo, Dynamics of Void Formation During Implantation of Si Under Self-annealing Conditions and Their Influence on Dopant Distribution. *Nucl. Instrum. Methods Phys. Res. B* **80/81**, 559 (1993).

25. V. Raineri, M. Saggio, and E. Rimini, Voids in Silicon by He Implantation: From Basic to Applications. *J. Mater. Res.* **15**, 1449 (2000).

26. C. C. Griffioen, J. H. Evans, P. C. de Jong, and A. van Veen, Helium Desorption/Permeation from Bubbles in Silicon: A Novel Method of Void Production. *Nucl. Instrum. Methods Phys. Res. B* **27,** 417 (1987).

27. C. Cawthorne and E. J. Fulton, Voids in Irradiated Stainless Steel. *Nature* **216**, 575 (1967).

28. J. H. Evans, Observations of a Regular Void Array in High Purity Molybdenum Irradiated with 2 MeV Nitrogen Ions. *Nature* **229**, 403 (1971).

29. B. A. Loomis, S. B. Gerber, and A. Taylor, Void Ordering in Ion-Irradiated Nb and Nb 1% Zr. *J. Nucl. Mater.* **68**, 19 (1977).

30. G. L. Kulcinski, J. L. Brimhall, and H. E. Kissinger, Production of Voids in Nickel with High Energy Selenium Ions. *J. Nucl. Mater.* **40**, 166 (1971).

31. A. Risbet and V. Levy, Order of Cavities in Magnesium and Aluminum Irradiated with Fast Neutrons. *J. Nucl. Mater.* **50**, 116 (1974).

32. N. M. Ghoniem, D. Walgraef, and S. J. Zinkle, Theory and Experiment of Nanostructure Self-organization in Irradiated Materials. *J. Comp. Aided Mat. Design* **8**, 1 (2002).

33. J. R. Willis, The Interaction of Gas Bubbles in an Anisotropic Elastic Solid. *J. Mech. Phys. Solids* **23**, 129 (1975).

34. A. M. Stoneham, Theory of Regular Arrays of Defects: The Void Lattice. *J. Phys. F: Metal Phys.* **1**, 778 (1971).

35. C. H. Woo and W. Frank, A Theory of Void Lattice Formation. *J. Nucl. Mater.* **137**, 7 (1985).

36. V. I. Dubinko, A. V. Tur, A. A. Turkin, and V. V. Yanovskij, A Mechanism of Formation and Properties of the Void Lattice in Metals Under Irradiation. *J. Nucl. Mater.* **57**, 161 (1989).

37. H. -C. Yu and W. Lu, Dynamics of the Self-assembly of Nanovoids and Nanobubbles in Solids. *Acta Mater.* **53**, 1799 (2005).

38. S. Hu and C. H. Henager Jr., Phase-field Modeling of Void Lattice Formation Under Irradiation. *J. Nucl. Mater.* **394**, 155 (2009).

39. I. H. Wilson, The Effects of Self-ion Bombardment (30-500 keV) on the Surface Topography of Single-crystal Germanium. *J. Appl. Phys.* **53**, 1698 (1982).

40. O. W. Holland, B. R. Appleton, and J. Narayan, Ion Implantation Damage and Annealing in Germanium. *J. Appl. Phys.* **54**, 2295 (1983).

41. B. R. Appleton, O. W. Holland, D. B. Poker, J. Narayan, and D. Fathy, Morphological Instabilities and Ion Beam Mixing in Ge. *Nucl. Instrum. Methods Phys. Res. B* **7/8,** 639 (1985).

42. L. M. Wang and R. C. Birtcher, Radiation-induced Formation of Cavities in Amorphous Germanium. *Appl. Phys. Lett.* **55**, 2494 (1989).

43. L. M. Wang and R. C. Birtcher, Amorphization, Morphological Instability and Crystallization of Krypton Ion Irradiated Germanium. *Philos. Mag. A* **64**, 1209 (1991).

44. H. Huber, W. Assmann, S. A. Karamian, A. Mücklich, W. Prusseit, E. Gazis, R. Grötzschel, M. Kokkoris, E. Kossionidis, H. D. Mieskes, and R. Vlastou, Void Formation in Ge Induced by High Energy Heavy Ion Irradiation. *Nucl. Instrum. Methods Phys. Res. B* **122**, 542 (1997).

45. D. Kleitman and H. J. Yearian, Radiation-induced Expansion of Semiconductors. *Phys. Rev.* **108**, 901 (1957).

46. Y. Homma, Anomalous Sputtering of Gallium-antimonide Under Cesium-ion Bombardment. *J. Vac. Sci. Technol. A* **5**, 321 (1987).

47. R. Callec, P. N. Favennec, M. Salvi, H. L'Haridon, and M. Gauneau, Anomalous Behavior of Ion-implanted GaSb. *Appl. Phys. Lett.* **59**, 1872 (1991).

48. R. Callec and A. Poudoulec, Characteristics of Implantation-induced Damage in GaSb. *J. Appl. Phys.* **73**, 4831 (1993).

49. N. Nitta, M. Taniwaki, Y. Hayashi, and T. Yoshiie, Formation of Cellular Defect Structure on GaSb Ion-implanted at Low Temperature. *J. Appl. Phys*. **92**, 1799 (2002).

50. S. M. Kluth, J. D. Fitz Gerald, and M. C. Ridgway, Ion-induced Porosity in GaSb. *Appl. Phys. Lett*. **86**, 131920 (2005).

51. N. Nitta and M. Taniwaki, Novel Nano-fabrication Technique Utilizing Ion Beam. *Nucl. Instrum. Methods Phys. Res. B* **206**, 482 (2003).

52. G. L. Destefanis and J. P. Gailliard, Very Efficient Void Formation in Ion Implanted InSb. *Appl. Phys. Lett.* **36**, 40 (1980).

53. G. L. Destefanis, J. P. Belle, J. M. Ogier-Collin, and J. P. Gailliard, Molecular Effect in the Expansion of Ion Implanted InSb. *Nucl. Instrum. Methods* **182/183**, 637 (1981).

54. M. Shaanan, R. Kalish, and V. Richter, Changes in InSb as a Result of Ion Implantation. *Nucl. Instrum. Methods Phys. Res. B* **7/8**, 443 (1985).

55. F. Frost, G. Lippold, A. Schindler, and F. Bigl, Morphological, Structural, and Electronic Damage on InAs and InSb Surfaces Induced by (Reactive) Ion Beam Etching. *Defect Diffus. Forum* **183**, 127 (2000).

56. S. M. Kluth, D. Llewellyn, and M. C. Ridgway, Irradiation Fluence Dependent Microstructural Evolution of Porous InSb. *Nucl. Instrum. Methods Phys. Res. B* **242**, 640 (2006).

57. S. I. Romanov and L. S. Smirnov, Voids in Ion Implanted Silicon. *Radiat. Eff.* **37**, 121 (1978).

58. Y. Zhang, T. Winzell, T. Zhang, I. A. Maximov, E.-L. Sarwe, M. Graczyk, L. Montelius, and H. J. Whitlow, High-fluence Co Implantation in Si, SiO_2/Si and Si_3N_4/Si Part III: Heavy-fluence Co Bombardment Induced Surface Topography Development. *Nucl. Instrum. Methods Phys. Res. B* **159**, 158 (1999).

59. A. Hedler, S. Klaumünzer, and W. Wesch, Swift Heavy Ion Irradiation of Amorphous Silicon. *Nucl. Instrum. Methods Phys. Res. B* **242**, 85 (2006).

60. W. J. Weber, R. C. Ewing, and L. M. Wang, The Radiation-induced Crystalline-to-Amorphous Transition in Zircon. *J. Mater. Res.* **9**, 688 (1994).

61. J. R. Dennis and E. B. Hale, Energy Dependence of Amorphizing Implant Dose in Silicon. *Appl. Phys. Lett.* **29**, 523 (1976).

62. F. F. Morehead, B. L. Crowder, and R. S. Title, Formation of Amorphous Silicon by Ion Bombardment as a Function of Ion, Temperature, and Dose. *J. Appl. Phys.* **43**, 1112 (1972).

63. J. R. Dennis and E. B. Hale, Crystalline to Amorphous Transformation in Ion-implanted Silicon: A Composite Model. *J. Appl. Phys.* **49**, 1119 (1978).

64. H. Yasuda and K. Furuya, Irradiation Temperature Dependence of Chemical and Topological Disordering Induced by High-energy Electron Irradiation in GaSb. *Phil. Mag. A* **80**, 2355 (2000).

65. L. M. Wang, S. X. Wang, R. C. Ewing, A. Meldrum, R. C. Birtcher, P. Newcomer Provencio, W. J. Weber, and H. Matzke, Irradiation-induced Nanostructures. *Mater. Sci. Eng. A* **286**, 72 (2000).

66. R. S. Averback and T. Diaz de la Rubia, Displacement Damage in Irradiated Metals and Semiconductors. *Solid State Phys.* **51**, 281 (1998).

67. M. Nastasi, J. W. Mayer, and J. K. Hirvonen, *Ion-solid Interactions: Fundamentals and Applications*. (Cambridge University Press; New York, 1996).

68. G. H. Kinchin and R. S. Pease, The Displacement of Atoms in Solids by Radiation. *Rep. Prog. Phys.* **18**, 1 (1955).

69. P. Sigmund, A Note on Integral Equations of the Kinchin-Pease Type. *Radiat. Eff.* **1**, 15 (1969).

70. M. J. Norgett, M. T. Robinson, and I. M. Torrens, A Proposed Method of Calculating Displacement Dose Rates. *Nucl. Eng. Des.* **33**, 50 (1975).

71. K. C. Russell, Phase Stability Under Irradiation. *Prog. Mater. Sci.* **28**, 229 (1984).

72. L. K. Mansur, Void Swelling in Metals and Alloys Under Irradiation: An Assessment of the Theory. *Nuc. Technol.* **40**, 5 (1978).

73. W. G. Wolfer and M. Ashkin, Stress-induced Diffusion of Point Defects to Spherical Sinks. *J. Appl. Phys.* **46**, 547 (1975).

74. W. G. Wolfer and L. K. Mansur, The Capture Efficiency of Coated Voids. *J. Nucl. Mater.* **91**, 265 (1980).

75. F. Spaepen, Structural Imperfections in Amorphous Metals. *J. Non-Cryst. Solids* **31**, 207 (1978).

76. T. Egami, K. Maeda, and V. Vitek, Structural Defects in Amorphous Soilds: A Computer Simulation Study. *Phil. Mag. A* **41**, 883 (1980).

77. T. K. Chaki and J. C. M. Li, Radiation Damage in an Amorphous Lennard-Jones Solid: A Computer Simulation. *Philos. Mag. B* **51**, 557 (1985).

78. J. Laakkonen and N. M. Nieminen, Computer Simulation and Identification of Vacancies and Interstitials in Amorphous Solids. *J. Phys. C: Solid State Phys.* **21**, 3663 (1988).

79. K. D. Li, A. G. Perez-Bergquist, and L. M. Wang, Computer Simulation of Radiation-induced Nanostructure Formation in Amorphous Materials. *Nucl. Instrum. Methods Phys. Res. B* **267**, 3063 (2009).

80. K. D. Li, A. G. Perez-Bergquist, Q. M. Wei, L. M. Wang, and W. Lu, Energy-dependent Irradiation-induced Nanostructure Formation in Amorphous Germanium. *J. Comput. Theor. Nanosci.* **7**, 522 (2010).

Chapter 2

Statement of Research Objectives

Despite a vast amount of research into ion irradiation-induced porous structures over the past six decades, a multitude of questions remain unanswered. Can we quantify the effects of ion irradiation parameters, such as atomic number, ion energy, and fluence? What role do materials properties, such as lattice structure, bond energy, and diffusion coefficients, play in the process, and how do environmental conditions, such as implantation temperature, affect the results? Can the effects of these parameters be quantified in terms of the resulting pore size, as well as the overall porous layer thickness and placement? Also, are irradiation conditions the most important factor in determining porous structure morphology, or do inherent materials properties of each material play a greater role in determining the final structure of the irradiated material?

The answers to many of these questions may require experimental, computational, and theoretical techniques, and as such, a combined approach is needed to better understand the processes behind irradiation-induced porous network formation. Here I present the research objectives of my thesis work:

- To experimentally study ion irradiation-induced nanostructure formation in four materials: GaSb, Ge, InSb, and Si. As discussed in the first chapter, there have been numerous experimental studies of ion irradiation effects in these materials.

However, there remain inconsistencies in the data and gaps to be filled in the research. For example, while the amorphous structure of ion-irradiated Ge has been conclusively shown, there are conflicting reports regarding the crystalline nature of irradiated GaSb. Also, while *in situ* irradiation experiments have been performed on Ge, no such work has been published on GaSb, despite the proposal of a formation mechanism for the unique nanostructures. Finally, though there are numerous studies of irradiation effects in Si, there has yet to be published any conclusive evidence of ion irradiation-induced porous network formation in the material. These issues and others will be addressed in Chapters 4-7.

- To provide qualitative and quantitative analysis of the resulting nanostructures, including the effects of ion energy, ion atomic number, ion fluence, ion flux, and sample temperature on the formation and evolution of the porous networks. These issues will be addressed for each material in the experimental results sections in Chapter 4-7. In Chapter 8, a summary of the effects of the irradiation parameters as well as the effects of the material properties of each material on porous network formation will be presented, and theoretical arguments to help explain some of the differences in observed behavior between the different materials will be discussed.
- To study the resulting size-dependent materials properties of the nanoscale porous structures. A vast amount of research in quantum confinement effects has shows that particle size can affect electronic and optical properties of nanoscale semiconductors. In Chapter 9, some select materials properties of porous semiconductors are obtained and analyzed, including thermal and optical

properties. In addition, engineering applications for irradiation-induced porous materials are discussed.

Chapter 3

Experimental Procedures

In this chapter, experimental procedures for all performed experiments are presented. The procedures are organized into sections covering irradiation of the sample materials, sample preparation for analysis, and sample analysis using various techniques, principally various electron microscopy techniques.

3.1 Sample Irradiation

Irradiation of samples was performed at three facilities: the Environmental Molecular Sciences Laboratory (EMSL) located at Pacific Northwest National Laboratory in Richland, WA, the Michigan Ion Beam Laboratory (MIBL) at the University of Michigan in Ann Arbor, MI, and the Electron Microbeam Analysis Laboratory (EMAL) at the University of Michigan in Ann Arbor, MI.

Irradiations performed at EMSL were performed using a National Electrostatics Corporation (NEC) 9SDH-2 3.0-MV tandem electrostatic accelerator. The accelerator is equipped with two Pelletron charging chains capable of carrying 300 mA of charging current to the high voltage terminal. The accelerator is capable of accelerating voltages up to 3 MV, but ion energies higher than 3 MeV can be obtained by acceleration of ions with charge states greater than 1. Faraday cup beam currents of roughly 10 μA are

obtainable for source atoms with atomic mass greater than 10 amu. When the ion accelerator is in operation, typical pressures in the high-energy beam lines are in the low-to-mid 10^{-8} Torr range. The ion accelerator is equipped with a SNICS II (Source of Negative Ions by Cesium Sputtering) ion source that is used to generate ions from virtually any solid source.

Irradiations performed at MIBL were performed using a National Electrostatics Corporation 400 kV ion implanter. The accelerator is capable of producing ions of energies in the range of 10 to 400 keV using a Danfysik Model 921 CHORDIS ion source, which is designed for the production of high current and high brightness ion beams using virtually any atom as a source. Ion currents vary depending on the source, but beam currents of over 100 μA are possible. Typical pressures during operation are roughly 10^{-8} Torr. The ion implantation stage is manufactured by High Voltage Engineering (HVEE) and allows for irradiations of up to four 6-inch wafer targets. In addition, built in liquid nitrogen cooling and resistive heating elements allow for sample temperature control in the range of roughly -200 to 800°C. Sample surface temperatures are measured using an IRCON Modline Plus infrared thermometer attached to one of the ports on the ion implantation stage.

Irradiations performed at EMAL were performed using an FEI Nova Nanolab Dualbeam FIB SEM workstation. The Dualbeam system consists of both ion and electron beams that can be used in conjunction for simultaneous imaging and irradiation. The FIB portion consists of a gallium liquid metal ion source (LMIS) that is capable of accelerating Ga^{+} ions at energies of 5 to 30 keV at beam currents of roughly 1 pA to 20 nA, depending on the beam voltage. Operating pressures for the chamber are in the range

of 10^{-7} to 10^{-8} Torr. Being a focused ion beam, very precise small areas can be irradiated by the beam, which has a maximum resolution of 7 nm at 30 kV and at 1 pA.

Although the 3 facilities discussed above were the only ones used to produce samples for this dissertation, a collaborator, Dr. Yanwen Zhang of Pacific Northwest National Laboratory, provided additional previously fabricated samples for analysis. These samples were prepared by metal vapor vacuum arc (MEVVA) ion irradiation at the Institute of Low Energy Nuclear Physics at Beijing Normal University using 40 keV Co^+ ions. An average beam flux of 51 $\mu A/cm^2$ was used. While not included here, a detailed explanation of experimental procedures for these samples was published and is available in Reference 1, and an initial microscopy study of these samples was subsequently published in Reference 2.

Throughout this chapter and the remainder of the dissertation, the terms high and low energy are used in relation to ion energies. For the purposes of this dissertation, high energy will refer to ions accelerated to energies of 280 keV up to a maximum of 9 MeV; these ions were produced using the broadbeam ion accelerator facilities available at EMSL and MIBL. Low energy will refer to ions accelerated to energies of 30 keV; these ions were produced solely using the Nova Nanolab Dualbeam system at EMAL. The MEVVA irradiated samples can also be considered low energy for the purposes of this study.

3.1.1 Irradiation Experiments Performed at EMSL

Single side mirror-polished (100) single crystal Ge, GaSb, and InSb wafers of 0.5 mm in thickness were sectioned into approximately 1 cm by 1 cm square samples. These

samples were then mounted in the NEC accelerator with the mirror-polished side facing the ion beam. All Ge, GaSb, and InSb samples were stationary during irradiation and implanted at perpendicular ion incidence. Samples were irradiated at room temperature with 1, 2, and 3 MeV Au^+ ions at an beam current density of 0.346 μA/cm^2 to fluences ranging from 2.9×10^{14} ions/cm^2 up to a maximum of 9×10^{15} ions/cm^2 for Ge, from 2.9 $\times 10^{14}$ ions/cm^2 up to a maximum of 9×10^{15} ions/cm^2 for GaSb, and from 5×10^{13} ions/cm^2 up to a maximum of 8.4×10^{14} ions/cm^2 for InSb. Fluence was calculated by charge integration. Specific implantation conditions for each sample tested are listed in Table 3.1. Though the samples were irradiated at room temperature, ion beam heating effects undoubtedly caused sample surface temperature to increase. While surface temperature measurements were not taken for the irradiation performed at PNNL, estimations of maximum sample surface temperature are made in Section 3.2.

Similarly, single side mirror-polished (100) single crystal Si wafers of 0.5 mm in thickness were sectioned into approximately 1 cm by 1 cm square samples. These samples were mounted in the NEC accelerator with the mirror-polished side facing the ion beam, with the ion beam at an angle of 7° from normal. All samples were stationary during the irradiation process. Samples were implanted with Au^+ and Au^{3+} ions at accelerator voltages of 1 MV and 3MV, respectively, resulting in ion energies of 1 MeV Au^+ and 9 MeV Au^{3+}. Implantation fluences ranged from 1×10^{14} ions/cm^2 up to a maximum of 7.8×10^{16} ions/cm^2, and ion beam current densities ranged from 0.1 μA/cm^2 for the 1 MeV sample irradiated to 1×10^{14} ions/cm^2 up to a high of 5.1 μA/cm^2 for the 9 MeV sample irradiated to 7.8×10^{16} ions/cm^2. Specific implantation conditions for each Si sample are also listed in Table 3.1. Again, while sample surface temperatures were not

Table 3.1. Irradiation conditions of samples irradiated at EMSL.

Material	Beam Angle [° From ⊥]	Ambient Temp. [°C]	Ion Type	Ion Energy [MeV]	Ion Fluence [ions/cm^2]	Ion Dose [dpa]	Beam Current Density [μA/cm^2]	Ion Flux [ions/cm^{2}s]
Ge	0	25	Au^+	1	1.00E+15	36.28	0.346	2.16E+12
Ge	0	25	Au^+	1	2.20E+15	79.82	0.346	2.16E+12
Ge	0	25	Au^+	1	6.00E+15	217.69	0.346	2.16E+12
Ge	0	25	Au^+	1	9.00E+15	326.53	0.346	2.16E+12
Ge	0	25	Au^+	2	2.90E+14	10.52	0.346	2.16E+12
Ge	0	25	Au^+	2	7.70E+14	27.94	0.346	2.16E+12
Ge	0	25	Au^+	2	1.70E+15	61.68	0.346	2.16E+12
Ge	0	25	Au^+	3	3.90E+14	14.15	0.346	2.16E+12
Ge	0	25	Au^+	3	1.05E+15	38.10	0.346	2.16E+12
Ge	0	25	Au^+	3	2.32E+15	84.17	0.346	2.16E+12
GaSb	0	25	Au^+	1	4.40E+13	2.13	0.346	2.16E+12
GaSb	0	25	Au^+	1	1.00E+14	4.83	0.346	2.16E+12
GaSb	0	25	Au^+	1	2.00E+14	9.66	0.346	2.16E+12
GaSb	0	25	Au^+	1	4.00E+14	19.32	0.346	2.16E+12
GaSb	0	25	Au^+	1	6.00E+14	28.98	0.346	2.16E+12
GaSb	0	25	Au^+	1	1.00E+15	48.30	0.346	2.16E+12
GaSb	0	25	Au^+	1	2.20E+15	106.25	0.346	2.16E+12
GaSb	0	25	Au^+	1	6.00E+15	289.77	0.346	2.16E+12
GaSb	0	25	Au^+	2	3.90E+13	1.88	0.346	2.16E+12
GaSb	0	25	Au^+	2	8.00E+13	3.86	0.346	2.16E+12
GaSb	0	25	Au^+	2	1.40E+14	6.76	0.346	2.16E+12
GaSb	0	25	Au^+	2	2.40E+14	11.59	0.346	2.16E+12
GaSb	0	25	Au^+	3	5.10E+13	2.46	0.346	2.16E+12
GaSb	0	25	Au^+	3	1.00E+14	4.83	0.346	2.16E+12
GaSb	0	25	Au^+	3	2.00E+14	9.66	0.346	2.16E+12
InSb	0	25	Au^+	1	5.00E+13	3.06	0.346	2.16E+12
InSb	0	25	Au^+	1	1.25E+14	7.65	0.346	2.16E+12
InSb	0	25	Au^+	1	3.00E+14	18.37	0.346	2.16E+12
InSb	0	25	Au^+	1	6.00E+14	36.73	0.346	2.16E+12
InSb	0	25	Au^+	1	8.40E+14	51.43	0.346	2.16E+12
InSb	0	25	Au^+	2	5.00E+13	3.06	0.346	2.16E+12
InSb	0	25	Au^+	2	1.20E+14	7.35	0.346	2.16E+12
InSb	0	25	Au^+	2	2.00E+14	12.24	0.346	2.16E+12
InSb	0	25	Au^+	3	5.00E+13	3.06	0.346	2.16E+12
InSb	0	25	Au^+	3	1.00E+14	6.12	0.346	2.16E+12
InSb	0	25	Au^+	3	2.00E+14	12.24	0.346	2.16E+12
Si	7	25	Au^+	1	1.00E+14	1.10	0.099	6.19E+11
Si	7	25	Au^+	1	1.00E+15	11.02	0.346	2.16E+12
Si	7	25	Au^+	1	1.00E+16	110.22	0.346	2.16E+12
Si	7	25	Au^{3+}	9	1.00E+14	1.30	2.56	1.60E+13
Si	7	25	Au^{3+}	9	1.00E+15	13.03	2.56	1.60E+13
Si	7	25	Au^{3+}	9	1.00E+16	130.26	2.56	1.60E+13
Si	7	25	Au^{3+}	9	7.80E+16	1016.03	5.12	3.20E+13

measured, estimations of maximum sample surface temperature are presented in Section 3.2.

3.1.2 Irradiation Experiments Performed at MIBL

High dose experiments were performed using the 400 kV NEC ion implanter using single side mirror-polished (100) single crystal Si wafers of 0.5 mm in thickness as the sample target. The wafers were sectioned into somewhat larger pieces than in the PNNL experiments, approximately 3 cm by 2 cm rectangles. These samples were mounted in a stationary position in the implantation stage with the mirror-polished surfaces perpendicular to the ion beam direction. To achieve a high ion flux at the sample surface, the ion beam was left stationary on the target without scanning the beam. 280 keV Si^+ ions were used for the experiments. Si was used as an ion source because use of solid ions would avoid gas accumulation effects in the Si target, and self-implantation with Si ions would avoid contamination of the Si target by high fluence implantation of foreign ions. Si^+ ions were accelerated at 280 kV rather than 400 kV because the ion beam current density was maximized at 280 kV, allowing for the maximum possible ion flux using a Si source. During the experiments, ion beam current fluctuated between ~20 and 25 μA, as measured at the Faraday cup. Beam size at the target measured roughly 3 mm in diameter, resulting in beam current densities of about ~250 - 300 μA/cm^2. Using the above conditions, Si targets were irradiated to fluences of ~ 2×10^{18} to 8×10^{18} ions/cm^2. Fluences were estimated based on beam current, time, and irradiated area.

Sample surface temperatures were measured at the point of irradiation using the IRCON infrared thermometer. A control sample was implanted without any resistive

heating or external cooling, which resulted in a surface temperature of ~ 450 - 500°C. Some samples were externally heated such that combined resistive and beam heating effects resulted in surface temperatures of ~ 600 - 650°C during implantation, while other samples were externally cooled with liquid nitrogen, resulting in surface temperature readings of ~170°C. An additional control sample was irradiated using a lower current density of ~ 70 $\mu A/cm^2$ but with additional resistive heating to bring the surface temperature to 600°C. Although surface temperature measurements were made, the actual measured temperatures are compared to theoretically derived surface temperature estimates in Section 3.2.

Finally, Si samples with 36 nm thick SiO_2 and Si_3N_4 surface layers were also implanted at high current densities and at high temperature. These surface layers were intended to act as sputter shields for the Si substrate, such that ion damage to the Si could be maximized while minimizing the sputtering of the Si itself. While (100) Si wafers were used as substrates, the surface coatings themselves were amorphous. Fabrication conditions for the SiO_2 and Si_3N_4 surface layers are listed in Reference 1, and specific implantation conditions for all Si samples irradiated at the MIBL facilities are listed in Table 3.2.

3.1.3 Irradiation Experiments Performed at EMAL

Single side mirror-polished (100) Si, Ge, GaSb, and InSb wafers samples of 0.5 mm in thickness were sectioned into approximately 1 cm by 1 cm square samples and mounted, polished side up, in the FEI Dualbeam FIB SEM using a copper adhesive tape. Samples were tilted to an angle of 52° within the Dualbeam's stage, which corresponds to

Table 3.2. Irradiation conditions of samples irradiated at MIBL. SiO_2/Si and Si_3N_4/Si indicate samples with 36 nm thick surface layers of SiO_2 and Si_3N_4, respectively.

Mater-ial	Beam Angle [° From ⊥]	Ambient Temp. [°C]	Surface Temp. [°C]	Ion Type	Ion Energy [MeV]	Ion Fluence [ions/ cm^2]	Ion Dose [dpa]	Beam Current Density [μA/cm^2]	Ion Flux [ions/ cm^{2}s]
Si	0	LNT	~170	Si^+	0.28	8.00E+18	12826	260	1.63E+15
Si	0	25	~450	Si^+	0.28	8.00E+18	12826	280	1.75E+15
Si	0	400	~500	Si^+	0.28	8.00E+18	12826	70	4.38E+14
Si	0	400	~650	Si^+	0.28	2.00E+18	3206	300	1.88E+15
Si	0	400	~650	Si^+	0.28	4.00E+18	6413	300	1.88E+15
Si	0	400	~650	Si^+	0.28	8.00E+18	12826	300	1.88E+15
SiO_2/Si	0	400	~650	Si^+	0.28	2.00E+18	3206	300	1.88E+15
SiO_2/Si	0	400	~650	Si^+	0.28	4.00E+18	6413	300	1.88E+15
SiO_2/Si	0	400	~650	Si^+	0.28	8.00E+18	12826	300	1.88E+15
Si_3N_4/Si	0	400	~650	Si^+	0.28	4.00E+18	6413	300	1.88E+15
Si_3N_4/Si	0	400	~650	Si^+	0.28	8.00E+18	12826	300	1.88E+15

perpendicular incidence between the sample surface and the FIB. Samples were irradiated with 30 keV Ga^+ ions at room temperature. Ge, GaSb, and InSb samples were irradiated to fluences ranging from roughly 1×10^{15} up to 2×10^{17} ions/cm^2. Si samples were irradiated to much higher maximum fluences, up to a maximum of 5×10^{19} ions/cm^2. Fluences were calculated using the beam current, irradiation time, and irradiated area. Typical ion beam current densities ranged from 25 μA/cm^2 to 250 μA/cm^2, with a high flux test performed at 15000 μA/cm^2 for the Si samples. High ion beam current densities were obtained by irradiating small areas, generally 10 μm × 10 μm or 20 μm × 20 μm squares. One of the unique aspects of FIB irradiation is that small irradiated regions of virtually any ion dose can be fabricated easily and quickly. Because of this, numerous irradiation conditions were tested. Table 3.3 lists a representative sample of the irradiation conditions tested for materials under FIB irradiation.

Table 3.3. Irradiation conditions of samples irradiated at EMAL.

Material	Beam Angle [° From ⊥]	Ambient Temp. [°C]	Ion Type	Ion Energy [keV]	Ion Fluence [ions/cm^2]	Ion Dose [dpa]	Beam Current Density [μA/cm^2]	Ion Flux [ions/cm^{2}s]
Ge	0	25	Ga^+	30	5.00E+14	6.80	25	1.56E+14
Ge	0	25	Ga^+	30	1.00E+15	13.61	25	1.56E+14
Ge	0	25	Ga^+	30	5.00E+15	68.03	125	7.81E+14
Ge	0	25	Ga^+	30	1.00E+16	136.05	125	7.81E+14
Ge	0	25	Ga^+	30	5.00E+16	680.27	250	1.56E+15
Ge	0	25	Ga^+	30	1.00E+17	1360.54	250	1.56E+15
GaSb	0	25	Ga^+	30	5.00E+14	8.52	25	1.56E+14
GaSb	0	25	Ga^+	30	1.00E+15	17.05	25	1.56E+14
GaSb	0	25	Ga^+	30	5.00E+15	85.23	125	7.81E+14
GaSb	0	25	Ga^+	30	1.00E+16	170.45	125	7.81E+14
GaSb	0	25	Ga^+	30	5.00E+16	852.27	250	1.56E+15
GaSb	0	25	Ga^+	30	1.00E+17	1704.55	250	1.56E+15
InSb	0	25	Ga^+	30	5.00E+14	9.52	25	1.56E+14
InSb	0	25	Ga^+	30	1.00E+15	19.05	25	1.56E+14
InSb	0	25	Ga^+	30	5.00E+15	95.24	125	7.81E+14
InSb	0	25	Ga^+	30	1.00E+16	190.48	125	7.81E+14
InSb	0	25	Ga^+	30	5.00E+16	952.38	250	1.56E+15
InSb	0	25	Ga^+	30	1.00E+17	1904.76	250	1.56E+15
InSb	0	25	Ga^+	30	2.00E+17	3809.52	250	1.56E+15
Si	0	25	Ga^+	30	5.00E+14	4.01	25	1.56E+14
Si	0	25	Ga^+	30	1.00E+15	8.02	25	1.56E+14
Si	0	25	Ga^+	30	5.00E+15	40.08	125	7.81E+14
Si	0	25	Ga^+	30	1.00E+16	80.16	125	7.81E+14
Si	0	25	Ga^+	30	5.00E+16	400.80	250	1.56E+15
Si	0	25	Ga^+	30	1.00E+17	801.60	250	1.56E+15
Si	0	25	Ga^+	30	5.00E+19	400802	15000	9.38E+16

3.1.4 Si MEEVA Experimental Procedures

Low energy, broad-beam ion implantations were performed using a MEVVA ion source to implant 40 keV Co^+ into (100) and (111) Si at ion fluences of 1×10^{16} ions/cm^2 to 2.8×10^{18} ions/cm^2. Samples were implanted at 30° from normal at an average ion beam current density of 51 μA/cm^2. All samples were provided by a collaborator, Dr. Yanwen Zhang, and produced at the Institute of Low Energy Nuclear Physics at Beijing Normal University. A detailed explanation of experimental procedures for fabrication of

these samples was published and is available in Reference 1. Due to the broad-beam implantation at high beam current density, sample temperature was elevated, and estimates of sample temperature are also listed in Reference 1.

3.2 Estimations of Sample Temperature During Irradiation

As mentioned throughout Section 3.1, most of the irradiations performed did not possess the capabilities to measure the sample surface temperature during irradiation, including all the tests performed at EMSL and EMAL. Here, two different methods are used to approximate the temperature rise at the sample surface due to ion beam heating effects. The first methodology used is a general theory of beam-induced substrate heating presented by T. R. Groves.[3] In the theory, a general solution of the heat equation is presented to determine the temperature rise, $\psi(r,t)$, at an observation point, r, and at time, t. To estimate temperature rise for the samples irradiated in this dissertation, the condition of an infinitely thin disk source of radius R depositing energy at the surface of a semi-infinite medium was chosen. Under these conditions, the equation for temperature rise at the origin, $r = 0$, centered over the source at the surface of the target medium, becomes:

$$\psi(0,t) = \frac{2}{\kappa} V \frac{\partial I}{\partial A} [\frac{1}{a}\sqrt{\frac{t}{\pi}}(1 - e^{-\frac{a^2R^2}{4t}}) + \frac{R}{2}(1 - erf(\frac{aR}{2t}))] \qquad (3.1)$$

where κ is the thermal conductivity, V is the accelerating voltage, $\frac{\partial I}{\partial A}$ is the beam current density, a is the thermal diffusivity in units of $s^{1/2}/m$, and $erf(x)$ is the standard error function. Using Eq. 3.1 in conjunction with thermal materials properties data for Si, Ge, GaSb, and InSb, shown in Table 3.4,[4,5] estimates of surface temperature increases due to ion beam heating can be calculated. Two issues must be considered in calculating data

points, however. The first is the change in thermal conductivity with temperature, which can be dealt with fairly easily by iteratively computing the temperature rise equation, each time using values for κ more appropriate to the predicted temperature. Values for thermal conductivity and diffusivity as a function of temperature for the four tested semiconductors can be found in References 4 and 5, and this data is shown in Table 3.5.

Table 3.4. Relevant thermal materials properties for Si, Ge, GaSb, and InSb.

	Silicon	Germanium	GaSb	InSb
Density [g/cm^3]:	2.329	5.323	5.614	5.775
Specific Heat Capacity [J/kg*K]:	702	321.9	320	144
Volumetric Heat Capacity [J/m^3*K]:	1.63E+06	1.71E+06	1.80E+06	8.32E+05
Thermal Conductivity [W/mK]:	124	64	27	16
Thermal Diffusivity [m^2/s]:	7.58E-05	3.74E-05	1.50E-05	1.92E-05
Thermal Diffusivity [s$^{1/2}$/m]:	114.8265873	163.6246515	257.9463051	227.9802623

Table 3.5. Thermal conductivity and diffusivity of Si, Ge, GaSb, and InSb as a function of temperature, given in units of W/mK and s$^{1/2}$/m, respectively.

	Silicon	Germanium	GaSb	InSb
Conductivity @ 300K (27C):	124.00	64.00	27.00	16.00
Diffusivity @ 300K (27C):	114.83	163.62	257.95	227.98
Conductivity @ 400K (127C):	98.00	43.00	22.00	11.00
Diffusivity @ 400K (127C):	129.16	199.62	285.76	274.95
Conductivity @ 500K (227C):	76.00	34.00	17.00	9.00
Diffusivity @ 500K (227C):	146.67	224.49	325.08	303.97
Conductivity @ 600K (337C):	62.00	27.00	14.00	8.00
Diffusivity @ 600K (337C):	162.39	251.92	358.22	322.41
Conductivity @ 700K (447C):	52.00	23.50	10.00	7.00
Diffusivity @ 700K (447C):	177.32	270.03	423.85	344.67
Conductivity @ 800K (557C):	42.00	20.00	8.00	7.00
Diffusivity @ 800K (557C):	197.30	292.70	473.88	344.67

The second issue with calculating temperature is dealing with the effects of porosity that is created throughout the ion irradiation process. As porosity increased, target material density decreases, as does thermal conductivity, as outlined in Reference 6. While the dependence of thermal conductivity on porosity depends in part on the pore

morphology and material, general estimates can be made that will help obtain more realistic surface temperatures. Table 3.6 lists materials properties needed for calculation of Eq. 3.1 where it is assumed that the target material contains a volume fraction of 90% porosity. For this case, the density of the porous material, ρ_p, becomes equal to one tenth of the bulk material, and given data from Reference 6, it is assumed that the thermal conductivity of the porous material, κ_p, becomes ~ one tenth that of the bulk as well. Table 3.7 lists the thermal conductivities and diffusivities of the irradiated material as a function of temperature for the case of 90% porosity. Thermal diffusivity does not change given the assumption that both density and thermal conductivity drop by equal amounts.

Table 3.6. Relevant thermal materials properties for Si, Ge, GaSb, and InSb where the material is assumed to be 90% porous, resulting in an order of magnitude decrease in density and thermal conductivity.

	Silicon	**Germanium**	**GaSb**	**InSb**
Density [g/cm^3]:	0.2329	0.5323	0.5614	0.5775
Specific Heat Capacity [J/kg*K]:	702	321.9	320	144
Volumetric Heat Capacity [J/m^3*K]:	1.63E+05	1.71E+05	1.80E+05	8.32E+04
Thermal Conductivity [W/mK]:	12.4	6.4	2.7	1.6
Thermal Diffusivity [m^2/s]:	7.58E-05	3.74E-05	1.50E-05	1.92E-05
Thermal Diffusivity [s$^{1/2}$/m]:	114.8265873	163.6246515	257.9463051	227.9802623

Table 3.7. Thermal conductivity and diffusivity of Si, Ge, GaSb, and InSb as a function of temperature, given in units of W/mK and s$^{1/2}$/m, respectively. Material properties are calculated for a material that is 90% porous.

	Silicon	**Germanium**	**GaSb**	**InSb**
Conductivity @ 300K (27C):	12.40	6.40	2.70	1.60
Diffusivity @ 300K (27C):	114.83	163.62	257.95	227.98
Conductivity @ 400K (127C):	9.80	4.30	2.20	1.10
Diffusivity @ 400K (127C):	129.16	199.62	285.76	274.95
Conductivity @ 500K (227C):	7.60	3.40	1.70	0.90
Diffusivity @ 500K (227C):	146.67	224.49	325.08	303.97
Conductivity @ 600K (337C):	6.20	2.70	1.40	0.80
Diffusivity @ 600K (337C):	162.39	251.92	358.22	322.41
Conductivity @ 700K (447C):	5.20	2.35	1.00	0.70
Diffusivity @ 700K (447C):	177.32	270.03	423.85	344.67
Conductivity @ 800K (557C):	4.20	2.00	0.80	0.70
Diffusivity @ 800K (557C):	197.30	292.70	473.88	344.67

Given the above data, an estimate of sample surface temperature can be obtained using Eq. 3.1. Table 3.8 lists estimated surface temperatures for irradiated Si, Ge, GaSb, and InSb samples for conditions pertaining to the various experiments performed at EMSL, MIBL, and EMAL at varying ion energies. For each different accelerator voltage, only the irradiation experiment with the maximum current density and maximum irradiation time were included. As such, the calculated temperature rise values should correspond to the maximum possible temperature rise seen by the implanted sample.

Table 3.8. Temperature rise calculations for irradiated Si, Ge, GaSb, and InSb.

Target Mater-ial	Ion Energy	Voltage [V]	Current Density [A/m^2]	Beam Radius [m]	Max. Ir-radiation Time [s]	Tempera-ture Rise [K]	Temperature Rise W/ 90% Porosity [K]	4.5x Temp-erature Rise W/ 90% Porosity [K]
Si	30 keV Ga^+	3.00E+04	2.5	0.00001	65	0.0060	0.0605	0.2722
Si	280 keV Si^+	2.80E+05	2.8	0.0015	6400	9.4895	94.8949	427.0269
Si	1 MeV Au^+	1.00E+06	0.00346	0.005	4570	0.1398	1.3984	6.2928
Si	9 MeV Au^{3+}	3.00E+07	0.0512	0.0015	2440	18.5982	185.9818	836.9182
Ge	30 keV Ga^+	3.00E+04	2.5	0.00001	65	0.0060	0.0605	0.2722
Ge	1 MeV Au^+	1.00E+06	0.00346	0.005	4110	0.1399	1.3986	6.2936
Ge	2 MeV Au^+	2.00E+06	0.00346	0.005	770	0.2805	2.8054	12.6245
Ge	3 MeV Au^+	3.00E+06	0.00346	0.005	1050	0.4205	4.2051	18.9230
GaSb	30 keV Ga^+	3.00E+04	2.5	0.00001	65	0.0060	0.0605	0.2722
GaSb	1 MeV Au^+	1.00E+06	0.00346	0.005	2740	0.1399	1.3993	6.2969
GaSb	2 MeV Au^+	2.00E+06	0.00346	0.005	110	0.2825	2.8252	12.7133
GaSb	3 MeV Au^+	3.00E+06	0.00346	0.005	90	0.4242	4.2418	19.0883
InSb	30 keV Ga^+	3.00E+04	2.5	0.00001	65	0.0060	0.0605	0.2722
InSb	1 MeV Au^+	1.00E+06	0.00346	0.005	380	0.1406	1.4056	6.3250
InSb	2 MeV Au^+	2.00E+06	0.00346	0.005	90	0.2828	2.8279	12.7255
InSb	3 MeV Au^+	3.00E+06	0.00346	0.005	90	0.4242	4.2418	19.0883

Table 3.8 also shows the estimated temperature rise for samples with 90 volume % porosity. Given the assumptions, this results in an order of magnitude increase in sample surface temperature. Unfortunately, given the lack of actual surface temperature data from either the EMSL or EMAL experiments, there is only one feasible comparison between actual measured data and the calculated data, which is the case of 280 keV Si^{+} irradiation of Si at MIBL without any external heating or cooling. As seen from Table 3.2, this sample experienced a surface temperature increase of roughly 425°K. Even in the maximum temperature rise scenario, this same sample only had a calculated temperature rise of ~95°K. The discrepancy between the measured and calculated values likely arises from assumptions made in the theoretical calculation, most important of which is the assumption of a semi-infinite medium. While this assumption is probably accurate for the FIB irradiation scenarios, where only small surface areas were irradiated, clearly this is not an accurate assumption for the broad beam implantations, where significant fractions of the target wafer surfaces were irradiated. For the broad beam irradiation, the realities of a finite medium indicate that actual surface temperatures should be higher than calculated. As such, an additional multiplying factor of 4.5 has been included as a comparison in Table 3.8. This multiplying factor results in an accurate temperature rise for the case of 280 keV Si^{+} irradiation of Si. The accuracy of the multiplying factor for the all implantation scenarios is nebulous, but even for this "worst-case" temperature rise scenario, only two conditions result in temperature rises in excess of 20°K, the 280 keV Si^{+} on Si test performed at MIBL and the 9 MeV Au^{3+} on Si test performed at EMSL. This indicates that for the vast majority of our experiments, the assumption of constant surface temperature during ion irradiation is fairly valid.

To further confirm the results of the temperature rise calculations, additional temperature rise calculations were performed using the approach of Ishitani and Kaga for temperature rise from FIB irradiation.[7] This is a simplified approach that calculates the temperature rise, ψ, at the point of irradiation using the equation:

$$\psi = \frac{R\sqrt{\pi}}{2\kappa} V \frac{\partial I}{\partial A} \tag{3.2}$$

where variables are defined identically as in Eq. 3.1. Results are shown in Table 3.9.

Table 3.9. Temperature rise calculations for irradiated Si, Ge, GaSb, and InSb using Eq. 3.2.

Target Mater -ial	Ion Energy	Voltage [V]	Current Density [A/m^2]	Beam Radius [m]	Irradia -tion Time [s]	Tempera- ture Rise [K]	Temperature Rise W/ 90% Porosity [K]	4.5x Temp- erature Rise W/ 90% Porosity [K]
Si	30 keV Ga^+	3.00E+04	0.5	0.00001	65	0.0054	0.0536	0.2412
Si	280 keV Si^+	2.80E+05	2.8	0.0015	6400	8.4049	84.0486	378.2188
Si	1 MeV Au^+	1.00E+06	0.00346	0.005	4570	0.1236	1.2364	5.5639
Si	9 MeV Au^{3+}	3.00E+07	0.0512	0.0015	2440	16.4667	164.6667	741.0001
Ge	30 keV Ga^+	3.00E+04	0.5	0.00001	65	0.0104	0.1039	0.4673
Ge	1 MeV Au^+	1.00E+06	0.00346	0.005	4110	0.2396	2.3956	10.7801
Ge	2 MeV Au^+	2.00E+06	0.00346	0.005	770	0.4791	4.7912	21.5602
Ge	3 MeV Au^+	3.00E+06	0.00346	0.005	1050	0.7187	7.1867	32.3404
GaSb	30 keV Ga^+	3.00E+04	0.5	0.00001	65	0.0246	0.2462	1.1078
GaSb	1 MeV Au^+	1.00E+06	0.00346	0.005	2740	0.5678	5.6784	25.5529
GaSb	2 MeV Au^+	2.00E+06	0.00346	0.005	110	1.1357	11.3568	51.1058
GaSb	3 MeV Au^+	3.00E+06	0.00346	0.005	90	1.7035	17.0353	76.6586
InSb	30 keV Ga^+	3.00E+04	0.5	0.00001	65	0.0415	0.4154	1.8694
InSb	1 MeV Au^+	1.00E+06	0.00346	0.005	380	0.9582	9.5823	43.1205
InSb	2 MeV Au^+	2.00E+06	0.00346	0.005	90	1.9165	19.1647	86.2410
InSb	3 MeV Au^+	3.00E+06	0.00346	0.005	90	2.8747	28.7470	129.3614

Similar to Table 3.8, Table 3.9 includes data for cases of 90 volume % porosity in the target and the case of 90 volume % porosity with an additional 4.5 temperature rise multiplier. Although calculations performed using Eq. 3.2 result in slightly higher estimated temperatures for the irradiated samples, the assumptions inherent in the temperature calculation, which are accurate for the case of FIB irradiation, are inherently inaccurate for the case of broad beam irradiation. Given the assumptions between both models, it is assumed that Groves' theory is more accurate for broad beam implantations, while Ishitani and Kagi's theory is possibly more accurate for FIB irradiations. Nonetheless, when comparing both temperature rise data sets, both theories predict fairly low temperature rises in all cases except for those of 280 keV Si^{+} on and 9 MeV Au^{3+} on Si. Therefore, for the purposes of this dissertation, temperature rise was assumed to be negligible in all other irradiation experiments.

3.3 Sample Preparation for Analysis

Irradiated samples required very little preparation for analysis using SEM. Due to their inherent electrical semiconductivity, the irradiated specimens could be mounted directly in the SEM for plan-view analysis. For cross-sectional SEM (XSEM), samples were cleaved within the irradiated region to provide a clean interface of the irradiated structure. A diamond-tipped pen was used to create a deep scratch on the backside of the irradiated samples. Then, the samples were placed on the edge of a glass slide, with the scratch aligned with the edge of the slide, and a force was imparted to the edge of the irradiated sample, causing the sample to cleave along the scratch. Cleaved samples were

stored in plastic Petri dished. Although some samples were tested in an atomic force microscope (AFM), no sample preparation was necessary for these specimens.

Both cross-sectional samples and crushed powder samples were prepared from the irradiated materials for TEM analysis. Cross-sectional TEM (XTEM) samples were prepared using T-Tool sample holders from Precision TEM, Inc. First, small pieces of the irradiated samples were obtained through multiple cleaving steps as described for XSEM preparation. These small pieces of samples were then bonded to (100) Si wafers which had been similarly cleaved into small pieces. The irradiated surface of the samples were bonded to the mirror-polished face of the (100) Si wafers using M-Bond 600, a commercially available epoxy resin. These bonded samples were then placed within small binder clips to apply pressure at the bonded interface. These samples, in the binder clip enclosure, were cured for 1 hour at a temperature of roughly 200°C. After curing, the samples were removed from the binder clip and allowed to cool to room temperature.

Samples were then attached to the side of a sample mounting block in a T-Tool 510A sample holder using the Crystalbond 509 adhesive, which is soluble in acetone, such that the bonded interface is the exposed polish surface. The interface of the samples were then polished by hand using Buehler diamond lapping films with sequentially decreasing abrasive sizes of 30 μm, 15 μm, 3 μm, and 1 μm, respectively. This resulted in a flat, mirror-polished cross-section of the interface between the irradiated sample and the silicon wafer. Afterwards, the sample mounting block was placed on a hot plate at about 200°C and the one side polished sample was removed from the mounting block. The polished interface of the sample was then attached, polished side down, to the glass sample mounting block of a T-Tool 510B sample holder using Crystalbond 509 adhesive.

After allowing to cool, the sample was again polished using Buehler diamond lapping films with sequentially decreasing abrasive sizes of 30 μm, 15 μm, 3 μm, and 1 μm, to a final thickness of about 5 to 10 μm. Thickness of the final polished cross-sectional samples was determined by optical microscopy of the silicon wafer pieces bonded to the irradiated samples. Silicon becomes translucent at thicknesses of about 10 μm, and it's color changes based on thickness, making it an ideal indicator of sample thickness.

Following polishing, a TEM sample grid was attached to the surface of the polished sample using M-Bond 600 and allowed to cure for 1 hour at 200°C. Various SPI TEM grids were used depending on the polished sample size, morphology, and composition. Generally, 1 mm aperture grids or 2 mm by 1 mm slot grids were used. Copper and nickel grids were generally used, primarily for price considerations. After curing and cooling to room temperature, the sample mounting block for the T-Tool 510B was submerged in acetone until the Crystalbond 509 adhesive dissolved, freeing the TEM grid and sample from the holder. Samples were then cleaned with methanol to remove acetone and adhesive residue. After cleaning, the TEM samples were placed in a Gatan Model 691 Precision Ion Polishing System (PIPS) to ion mill the cross-sectional samples to an electron transparent thickness. PIPS milling conditions were: dual ion beam milling (one beam milling from above the sample, one from below), a chamber pressure of ~ 5×10^{-6} Torr, sample rotation of 3 rpm, beam energy of ~ 4.5 keV, and ion beam angles ranging from 9° to 4° from the sample surface depending on sample thickness and sputter rate. Initially, milling was begun at 9° for most samples and brought down to 4° as a hole began to develop in the milled sample, but in some samples that were noticeably thin to begin with, milling was begun at only 7° and brought down to 4°. Milling time varied

with the sample thickness and sputter rate of the target material. After milling, the samples were stored in a Glider SB100 TEM sample storage grid.

Crushed-powder TEM samples were prepared by first polishing down the backside of the irradiated samples such that only the near-surface region of the irradiated samples remained. Irradiated samples were cleaved into small pieces and then bonded, irradiated face down, to the glass sample mounting block of a T-Tool 510B sample holder using Crystalbond 509 adhesive. The backside of the irradiated samples were then polished by hand using Buehler diamond lapping films with sequentially decreasing abrasive sizes of 30 μm, 15 μm, and 3 μm, respectively, to a final thickness of roughly 10 μm. The sample mounting block was then submerged in an acetone bath, allowing the thinned samples to be removed from the mounting block. The samples were then cleaned in ethanol and placed in an ethanol solution in a small porcelain mortar and pestle. Samples were crushed by hand in the mortar and pestle for approximately 10 minutes per sample, resulting in the formation of a nanoparticle suspension of the irradiated surface structures. Afterwards, the nanoparticle suspensions in ethanol were transferred to small vials via pipette and placed in a Branson 1510 Ultrasonic Cleaner for 30 minutes to disperse the nanoparticles in solution. Immediately afterwards, for each sample, two droplets of the dispersed solution was deposited via clean pipette to an SPI 200 mesh copper TEM grid with a carbon-coated Formvar coating, commonly refered to as a "holey-carbon" grid. These holey carbon grids contain an electron transparent coating of carbon-coated polymer that acts as a support for nanoparticles or other materials deposited upon the grid. After air drying, the samples were stored in a Glider SB100 TEM sample storage grid.

In addition, annealing of irradiated samples was performed to recrystallize samples amorphized by ion irradiation, and annealed samples were primarily used for luminescent intensity experimentation. The specific samples that were heat-treated are listed in Section 10.2, which deals with increases in luminescent intensity of ion irradiated semiconductors, but the procedures for annealing of the samples are outlined here. Each sample to be annealed was encapsulated in quartz tubes by glassblower Harald Eberhart. Each tube was vacuum pumped to less than 1×10^{-6} Torr and back-filled with inert argon gas before closing. After encapsulation, the enclosed samples were thermally annealed in a 5 kW Lindberg/Blue M tube furnace with a maximum operating temperature of 1700°C. Each sample was annealed for 600 seconds, each at a temperature suited to recrystallization in that material: 250°C for GaSb, 300°C for InSb, 600°C for Ge, and 650°C for Si. After air-cooling to room temperature, the tubes were broken opened, and the annealed samples were used to create further SEM and TEM specimens. In the case of GaSb, annealing produced chages in the morphology of the samples, as discussed in Section 10.1. To confirm the effects of annealing in GaSb only, some unannealed irradiated GaSb samples were annealed in a JEOL 2010F analytical TEM *in situ* to confirm the results from the tube furnace. Samples were heated in a Gatan 652 Double-Tilt Resistive Heating Holder to a temperature of 250°C for over 600 seconds.

3.4 Sample Analysis

Plan view SEM and XSEM images were taken of the as-irradiated samples using an FEI Nova Nanolab Dualbeam FIB operated in SEM mode. XSEM was performed on the cleaved samples with an electron beam incident angle of 90º to the side of the original

sample surface. SEM imaging was performed with the secondary electron detector at a working distance of 5 mm, and typical imaging conditions were an electron beam current of 98 pA at 5 kV or a beam current of 0.13 nA at 10 kV. Both electron beam conditions produced quality SEM images and were used interchangeably. Composition of the ion-irradiated layers was tested through energy-dispersive x-ray spectroscopy (EDS) analysis using an EDAX UTW detector.

Most TEM work was performed using a JEOL 2010F analytical electron microscope operating at 200 kV and a column pressure of less than 1.5×10^{-7} Torr. JEOL single tilt and double tilt holders were used unless otherwise noted. Bright field (BF) imaging was performed in TEM mode to image the irradiated surfaces, and high-resolution TEM (HRTEM) imaging was performed to study the crystallographic structure of the irradiated materials at the atomic scale. In addition, SAED was performed in diffraction mode to help determine sample crystallinity. Scanning transmission electron microscopy (STEM) was used to obtain higher resolution images of irradiated nanostructures. A 0.2 nm electron probe was used for experiments performed in STEM mode. High-angle annular dark field (HAADF) imaging was used to provide qualitative data regarding sample composition. EDS was performed using an EDAX r-TEM Detector in both TEM and STEM modes to confirm specimen composition and provide more quantitative data regarding sample composition. A Gatan Image Filter (GIF) was used for electron energy loss spectroscopy (EELS) analysis and imaging in STEM mode, which also provided data regarding sample composition. Additional HRTEM images were taken at an accelerating voltage of 300 kV and at a column pressure of less than 1.5×10^{-7} Torr using a JEOL 3011 High Resolution TEM.

Additional analysis of ion-irradiated InSb surface morphologies, discussed in Section 6.1.2, was performed via atomic force microscopy (AFM). AFM micrographs were obtained using a Digital Instruments NanoScope IIIa-Phase AFM using an AFMD scanner that scans a 12 μm × 12 μm square area. The AFM was operated in tapping mode with an etched single crystal silicon probe. AFM data was intended to be used primarily for obtaining surface roughness readings for the irradiated samples.

Testing of the photoluminescent intensity of irradiated Ge, GaSb, InSb, and Si samples was performed by Dr. Juan Antonio Zapien and Dr. Xiuli Zhou at the City University of Hong Kong via near-field scanning optical microscopy (NSOM). NSOM is a microscopic technique where the optical detector is placed extremely close to the specimen surface, at a distance much smaller than the wavelength, λ, of the illuminating light. NSOM allows for surface analysis with high spatial, spectral, and temporal resolving power. With this technique, the resolution of the image is limited by the size of the detector aperture and not by the wavelength of the illuminating light. For samples investigated at the City University of Hong Kong, photoluminescent intensities were measured in arbitrary units as a function of spatial position using an illumination laser with an excitation wavelength of 633 nm for all samples.

3.5 TRIM Simulations

The TRIM (Transport and Range of Ions in Matter) computer code was used to calculate estimated values for implantation parameters, such as ion range, ion concentration, vacancy production rate, etc., for use in analyzing observed experimental results. Values for bulk material density, displacement energy, and surface binding

energy were defined as shown in Table 3.10. Displacement energy values were taken from the literature and are shown in Table 3.11. Threshold displacement energy is defined as the minimum energy required for displacement of an atom from its lattice site, while average displacement energy is defined as the average energy required for displacement of an atom from its lattice site over all possible lattice directions. Values for average displacement energy shown in Table 3.10 were taken from the literature where available and were estimated as double the average of the threshold displacement energy values taken from the literature where reported values were unavailable. This approximation is based on the ratio of reported values for the average displacement energy to threshold displacement energy for Si and Ge, as well as upon trends reported by Nastasi *et. al.*.[8] Surface binding energy is defined as the energy required for an atom on the surface of the target to leave the surface. Surface binding energy values were taken as given by TRIM.

Table 3.10. Materials parameters used for TRIM calculations.

Material	Bulk Density [g/cm^3]	Displacement Energy [eV]	Surface Binding Energy [eV]
Si	2.32	36	4.7
Ge	5.35	23	3.88
GaSb	5.6	12.4 (Ga), 20.8 (Sb)	2.82 (Ga), 2.72 (Sb)
InSb	5.77	12.2 (In), 16 (Sb)	2.49 (In), 2.72 (Sb)

Table 3.11. Displacement energies for Si, Ge, GaSb, and InSb. References for each value are listed.

Material	Threshold Displacement Energy [eV]	Average Displacement Energy [eV]
Si	13[8], 15.8[9]	36[10]
Ge	15[8], 14.8[9]	23[11]
GaSb	6.2[12], 6.2[13] (Ga), 10.3[12], 10.5[13] (Sb)	-
InSb	5.8[9], 6.4[14] (In), 6.8[8], 9.2[14] (Sb)	-

Bibliography

1. Y. Zhang, T. Winzell, T. Zhang, M. Andersson, I. A. Maximov, E.-L. Sarwe, M. Graczyk, L. Montelius, and H. J. Whitlow, High-fluence Co Implantation in Si, SiO_2/Si and Si_3N_4/Si Part I: Formation of Thin Silicide Surface Films. *Nucl. Instrum. Methods Phys. Res. B* **159**, 142 (1999).

2. Y. Zhang, T. Winzell, T. Zhang, I. A. Maximov, E.-L. Sarwe, M. Graczyk, L. Montelius, and H. J. Whitlow, High-fluence Co Implantation in Si, SiO_2/Si and Si_3N_4/Si Part III: Heavy-fluence Co Bombardment Induced Surface Topography Development. *Nucl. Instrum. Methods Phys. Res. B* **159**, 158 (1999).

3. T. R. Groves, Theory of Beam-induced Substrate Heating, *J. Vac. Sci. Technol. B* **14**, 3839 (1996).

4. CRC Handbook of Chemistry and Physics, 87th ed., edited by D.R. Lide (Taylor and Francis, New York, 2006).

5. Ya. B. Magomedov and A. R. Bilalov, Thermal Conductivity and the Wiedemann–Franz Relation in Melts of Indium and Gallium Antimonides. *Semiconductors* **35**, 499 (2001).

6. R. W. Rice, Evaluation and Extension of Physical Property-porosity Models Based on Minimum Solid Area. *J. Mater. Sci.* **31**, 102 (1996).

7. T. Ishitani and H. Kaga, Calculation of Local Temperature Rise in Focused-ion-beam Sample Preparation. *J. Electron Microsc.* **44**, 331 (1995).

8. M. Nastasi, J. W. Mayer, and J. K. Hirvonen, *Ion-solid Interactions: Fundamentals and Applications*. (Cambridge University Press; New York, 1996).

9. J. Wang and W. Yang, Effects of Irradiation with Gamma and Beta Rays on Semiconductor Hall Effect Devices. *Nucl. Instrum. Methods Phys. Res. B* **266**, 3583 (2008).

10. E. Holmström, A. Kuronen, and K. Nordlund, Threshold Defect Production in Silicon Determined by Density Functional Theory Molecular Dynamics Simulations. *Phys Rev*. *B* **78**, 045202 (2008).

11. E. Holmström, K. Nordlund, and A. Kuronen, Threshold Defect Production in Germanium Determined by Density Functional Theory Molecular Dynamics Simulations. *Phys. Scr.* **81**, 035601 (2010).

12. K. Thommen, Energy and Orientation Dependence of Electron-irradiation-induced Damage in Undoped GaSb. *Phys. Rev.* **174**, 938 (1968).

13. M. Mukhopadhyay and S. Basu, Radiation Damage of Gallium Antimonide – Effect on Electrical and Optical Properties. *Radiat. Eff.* **132**, 215 (1994).

14. F. H. Eisen, Orientation Dependence of Electron Radiation Damage in InSb. *Phys. Rev.* **135**, 1394 (1964).

Chapter 4

Ion Irradiation of GaSb

GaSb is a narrow band gap semiconductor that has been studied extensively for use in a variety of optoelectronic devices, including laser diodes, photodetectors, and high frequency electronic devices.[1] GaSb can be used to create ordered nanodot arrays,[2] and recently GaSb has been reported as a promising material for use in thermo-photovoltaic systems and tandem concentrator solar cells.[3,4] In this chapter, the effects of ion irradiation in GaSb are studied in high and low ion energy regimes.

4.1 High Energy Ion Irradiation

4.1.1 Embedded GaSb Nanofibers

After ion irradiation at room temperature with 1 MeV Au^+ ions to 1×10^{14} ions/cm^2 (4.8 dpa), three distinct regions, a solid surface layer, a nanofibrous layer, and a mesoporous layer, were visible in the GaSb sample by XSEM as shown in Figure 4.1. At the sample surface, the sample shows a thin intact surface layer of uniform thickness (the top portion of Figure 4.1b). At this ion fluence, the thickness of the surface layer was measured to be roughly 20 nm. At higher fluences of up to 6×10^{14} ions/cm^2 (29.0 dpa), the surface layer remained uniform in thickness, at 20±3 nm as measured by SEM. At ion fluences higher than 6×10^{14} ions/cm^2, the surface layer tends to be non-uniformly removed. At ion fluences greater than 1×10^{15} ions/cm^2 (48.3 dpa), the GaSb fibers

became completely exposed, with a cobweb-like structure beginning to speckle the surface of the irradiated area above 6×10^{15} ions/cm^2 (289.8 dpa) (see Section 4.1.2).

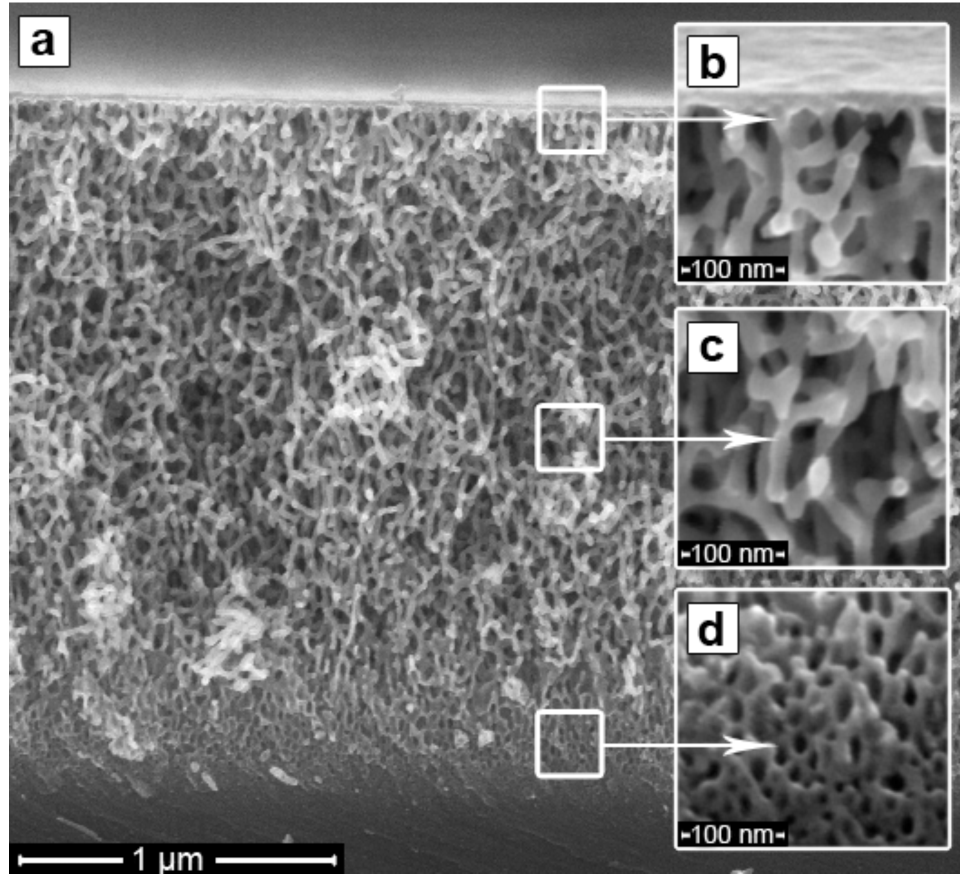

Figure 4.1. a) Cross-sectional SEM image of GaSb fiber layers irradiated with 1 MeV Au^+ to 1×10^{14} ions/cm^2. Insets show b) the surface layer (tilted to 10° off axis), c) the presence of fully formed fibers, and d) a mesoporous region in which pore size shrinks, transitioning from a fibrous matrix to a solid substrate.

Directly underneath the thin surface layer is a regime of fully formed, relatively uniformly spaced GaSb nanofibers of ~20 nm in diameter. At a fluence of 1×10^{14} ions/cm^2, the fiber layer measured ~2.15 µm in thickness (Figure 4.1a), and the layer continued to increase in thickness with increasing ion fluence, despite a predicted average ion range of just 173 nm for 1 MeV Au^+ in GaSb, as predicted by TRIM. The fiber layer retained its structural integrity up through a fluence of 6×10^{14} ions/cm^2, at which point

the layer measured 6.2 μm in thickness. However, at higher ion fluences the fiber layer became increasingly fragile, and the thickness was no longer uniform. At the maximum tested ion fluence of 6×10^{15} ions/cm^2, portions of the GaSb fiber layer reached a thickness of roughly 20 μm. The fiber diameter, which was measured to be in the range of 20±4 nm from electron microscopy images, remained fairly uniform both within each sample and across the range of ion fluences (Figure 4.2). Increasing the ion fluence from 1×10^{14} to 6×10^{15} ions/cm^2 did not appear to strongly affect the average fiber diameter (Figure 4.2a). Measured data points for fiber size as a function of implantation conditions are included in Appendix 1. In addition, images of GaSb samples irradiated with 150 keV Kr^+ ions were provided for comparison by a former post-doctoral appointee of the research group, Dr. Sha Zhu. The Kr^+ implanted samples also resulted in very uniform fibers of ~16 nm in diameter (Figure 4.2b). GaSb nanofiber diameter seems to be only weakly affected by irradiation parameters given the similar fiber sizes seen in samples irradiated with different types of ions (Kr^+, Au^+), different ion energies (150 keV - 1 MeV), and different ion fluences (1×10^{14} to 6×10^{15} ions/cm^2). Although our experimentation resulted in limited variation in fiber size with varying implantation parameters, as listed in Appendix 1, fiber size values reported in the literature range from 10 to 20 nm.[5-7] Some of the variation in values from the literature seems to be due to accuracy and alignment of instrumentation, however, as reported values for fiber size do not change significantly within individual publications, only when comparing values from separate publications. TEM measurements indicated the presence of nanocrystals within the GaSb fibers, as also reported in the literature,[8] but the majority of the fiber volume remains amorphous (Figure 4.2c).

At the bottom of the sample cross-section, a transitional nanoporous layer contains voids 10 nm in diameter (Figure 4.1d), as compared to ~50 nm in diameter in the fiber regime. This transitional layer is a formation regime, in which the bulk of the incident ion energy is deposited. As the incident Au^+ ions slow down, they rapidly begin to lose energy through atomic collision cascades, resulting in a thin porous layer and a quick transition from GaSb fibers to the dense substrate. A thin layer of partially amorphous GaSb, caused by limited atomic collision damage, separates the porous region from the crystalline substrate.[9,10]

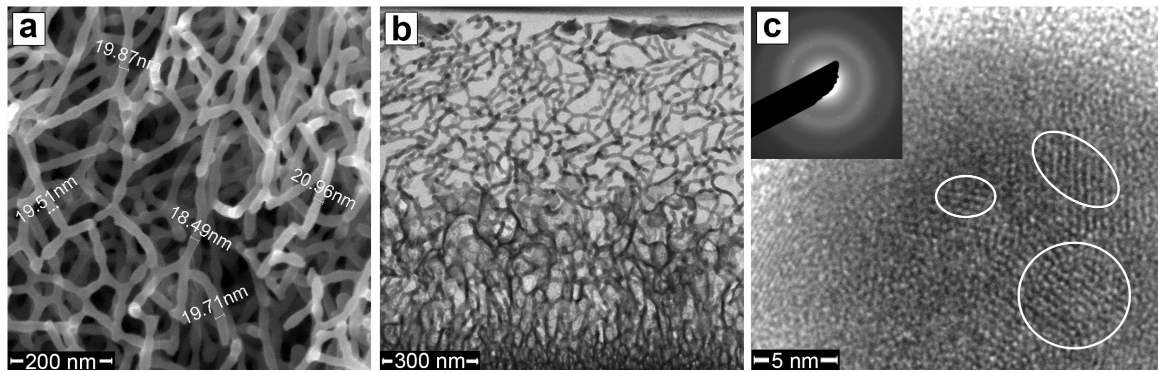

Figure 4.2. SEM and TEM images of GaSb fibers. a) GaSb fibers irradiated at 6×10^{14} ions/cm^2 with 1 MeV Au^+ ions. SEM imaging shows that fiber diameter is fairly uniform and does not change at increased ion fluence. b) Image of GaSb fibers irradiated at 6×10^{15} ions/cm^2 with 150 keV Kr^+ ions, provided by Dr. Sha Zhu. XTEM image shows that fiber size also remains fairly constant at varying implantation energies. c) High resolution TEM (HRTEM) image of a single fiber reveals that multiple nanocrystals are present within the fiber, and diffraction of the fiber volume (inset) shows distinct halos, confirming the presence of nanocrystals in the bulk fiber mass.

Investigation of GaSb samples irradiated with 2 and 3 MeV Au^+ ions (estimated average penetration depths of 332 nm and 495 nm, respectively) showed the same overall structure but with thicker porous layers at the same fluences. For a sample irradiated to a fluence of 2×10^{14} ions/cm^2 (9.7 dpa) with 1 MeV Au^+ ions, the porous layer was 5.6 μm in thickness, as compared with 6.6 μm and 8.4 μm for samples irradiated with 2 and 3

MeV ions, respectively. Porous layer thickness measurements for all irradiated materials are included in Appendix 2. For all three samples, however, a surface layer of roughly the same thickness (20±4 nm) was observed.

A qualitative defect structure formation mechanism, shown in Figure 1.5, has been developed by Nitta *et. al.* that describes the formation process of porous GaSb at relatively low ion implantation energies (~ 60 keV).[6,10] However, this formation mechanism breaks down for ion implantation at higher energies, in this case with 1 MeV Au^+, as evidenced by the presence of a thick, embedded fiber region as seen in Figure 4.1. A qualitative defect structure formation mechanism for higher energy ions is shown in Figure 4.3.

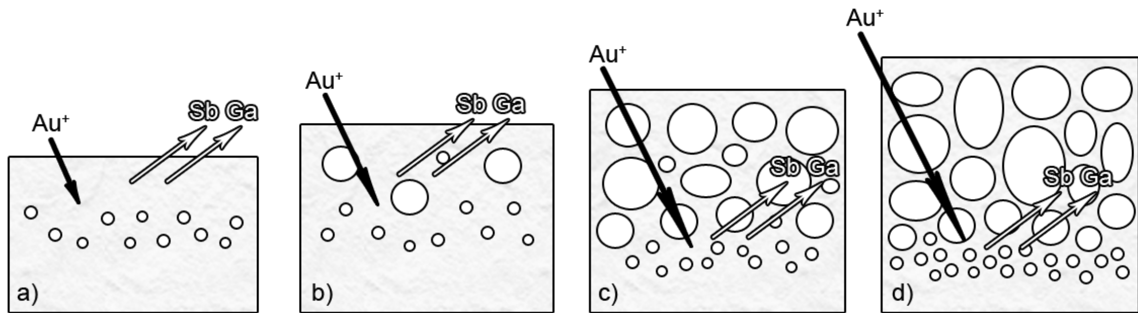

Figure 4.3. Nanofiber formation mechanism for higher energy ions, with a 2-D GaSb cross-section shown under Au^+ ion irradiation. a) Incoming ions cause the formation of vacancies, and b) as vacancies agglomerate, voids form. c) As voids accumulate, the material becomes less dense. d) Incoming ions are able to penetrate thick layers of low-density porous material, and sputtering and redeposition of Ga and Sb within the porous layer may influence the evolution of the morphology.

At first, incident ion irradiation results in the formation of point defects. As proposed in the literature, vacancies preferentially coalesce into voids due to highly inefficient recombination of vacancies and interstitials in GaSb.[5] The voids continue to grow with continued ion irradiation, and as voids accumulate, the density of the material drops dramatically. Since an ion's interaction cross-section with a material is correlated

to material density, a substantial decrease in material density allows incident ions to penetrate through fairly thick porous layers. Due to the nature of atomic interaction cross-sections, the majority of atomic collisions happen at the end of the ion range, where ion energy is relatively low and nuclear stopping is predominant. Thus, incident ions continue to cause void formation and growth at the bottom of the fiber layer (at the interface with the substrate) while causing limited damage to the surface and near-surface region. Since the probability of nuclear interaction between an incoming high-energy atom and a ~20 nm thick surface layer is fairly low, the surface layer experiences fewer sputtering interactions than the bulk material and the surface thickness remains fairly constant at increasing ion fluence. Essentially, as the porous layer forms, atomic collisions in the low-density porous layer are limited, which may explain the relative uniformity in fiber diameter at increasing ion fluences, although diffusion mechanics and surface energy considerations could also be important factors controlling fiber size.

Overall, irradiation with high-energy ions causes continuous void growth at the bottom of the fiber layer, where nuclear stopping is significant. Because the energy of the incoming ion is weakly curtailed by the sparse fibers, the incoming ion continually deposits the bulk of its energy through atomic collisions in the dense transition regime. This model of continuous fiber growth upon ion irradiation breaks down at very high fluences, when the fiber layer becomes thick enough that significant atomic energy losses begin to take place in the fiber layer rather than in the substrate. With 1 MeV Au^+ ions, this occurred at about 2.2×10^{15} ions/cm^2 in a fiber layer thickness of roughly 18.4 µm. At this point, a three-fold increase in the ion fluence to 6×10^{15} ions/cm^2 resulted in only a modest increase in the porous layer thickness to about 20.2 µm.

4.1.2 Surface Layer Response Under Irradiation

At the sample surface, after an ion fluence of 1×10^{14} ions/cm^2, the entire irradiated area of the sample was covered by a uniform surface layer, but as ion fluence increased, the surface layer was progressively removed in a non-uniform fashion such that selected regions of the surface were preferentially removed over others. Initially, only very small breaks resembling polymer crazing occur in the surface layer (Figure 4.4a). As the ion fluence increases, breaches in the surface layer expand, exposing increasingly greater amounts of embedded nanofibers (Figure 4.4b). When two openings in the surface layer expand into one another, the expansion fronts stretch into thin strands (Figure 4.4c). As ions continue to bombard the surface, the surface layer begins to detach from the fiber layer, with large patches of the surface beginning to crack and spall off (Figure 4.4d). Eventually, the entire surface is removed, but further ion irradiation creates cobweb-like structures uniformly distributed across the exposed fiber surface (Figures 4.4e and 4.4f). These cobweb-like structures appear to be formed by remnants of the surface layer in response to continued ion irradiation. Structures shown in Figure 4.4 were chosen to be representative of the surface evolution of irradiated GaSb at increasing fluence, but for a more extensive analysis of the propensity of such structures over the entire irradiated surface, see Appendix 3.

As showcased in Figure 4.4a, openings in the surface layer initially tend to be long and thin, and they often are arranged in parallel orientations. However, investigation of the break orientations shows no crystallographic dependence, indicating that some other formation mechanism is responsible. As the breaks expand, they tend to retain their initial orientation until, with increasing ion fluence, surface openings begin to intersect

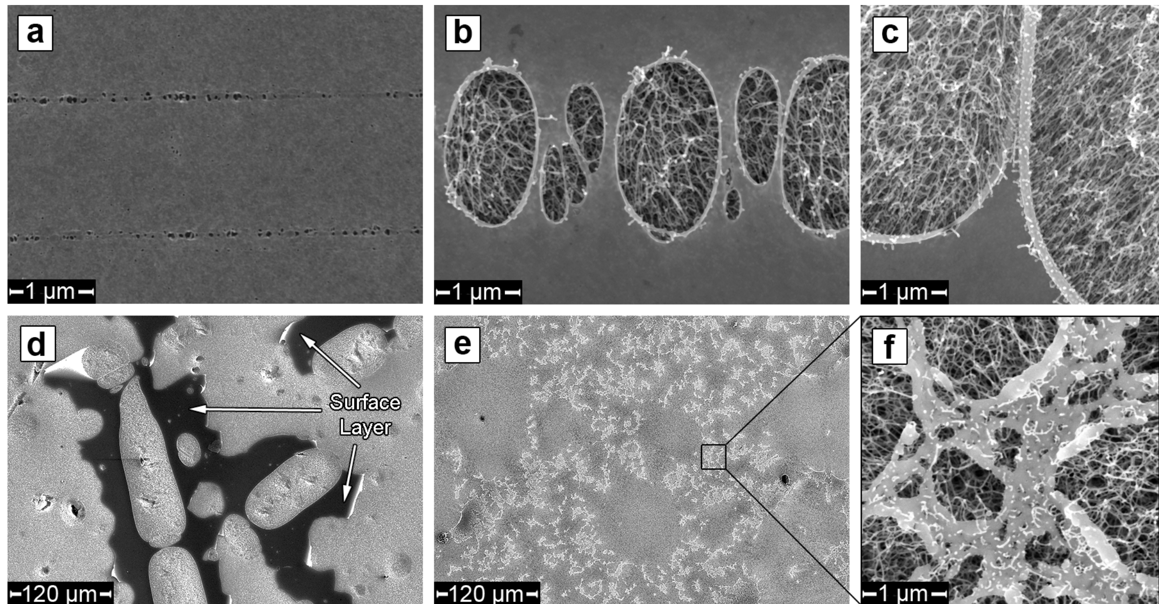

Figure 4.4. Plan view SEM images of GaSb irradiated with 1 MeV Au^+ at fluences of a) 1×10^{14} ions/cm^2, b,c) 4×10^{14} ions/cm^2, d) 6×10^{14} ions/cm^2, e,f) and 6×10^{15} ions/cm^2. As ion fluence increases, the surface layer is stretched, exposing embedded nanofibers. Eventually, the majority of the surface layer begins to crack and peel away, exposing the fibers to the surface. Continued ion irradiation past this point results in degradation of the fibers into web-like patches.

and overlap, causing all semblance of an ordered removal method to be lost. SEM observation of the irradiated GaSb surface also indicates that the surface layer deforms plastically under irradiation. Bulk GaSb is brittle, but the nanoplasticity of amorphous semiconductors is not fully understood. Recent experimental and theoretical work seems to support the idea that nanoscale materials can exhibit size-dependent elastic phenomena in the length scale range of less than ~10 nm due to increased surface energy effects caused by large surface area-to-volume ratios present at the nanoscale.[11,12] In addition, radiation-enhanced diffusion (RED) is known to lead to enhanced mixing and plastic flow in irradiated materials,[13] and RED leading to plastic flow has been reported in similar irradiated systems, such as GaAs.[14] Visual evidence of the behavior of the GaSb surface layer seems to support arguments for enhanced plastic behavior in nanomaterials

under irradiation. The craze-like openings in Figure 4.4a and the taffy-like strands seen in Figure 4.4c are consistent with characteristics of a material undergoing plastic deformation. Overall, Figure 4.5 presents a schematic showing the observed steps in the surface layer removal process for high-energy ion bombardment of GaSb.

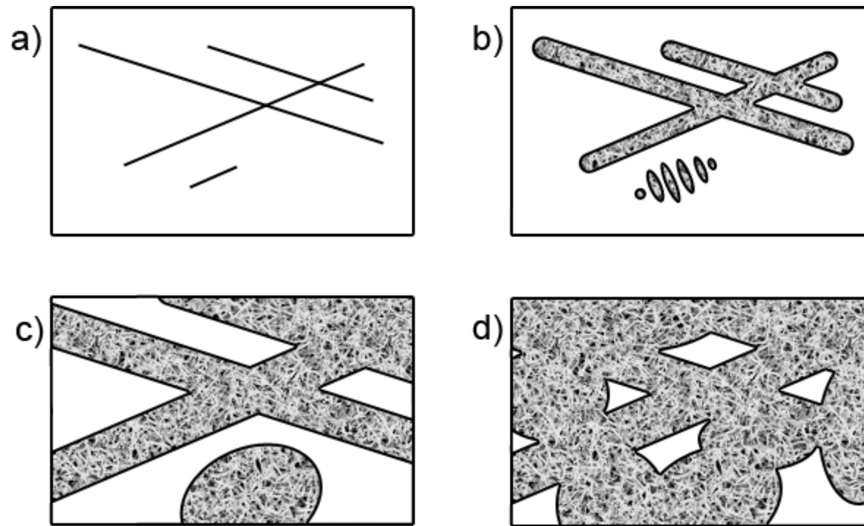

Figure 4.5. Surface layer removal process for 1 MeV Au^{+} irradiated GaSb shown in a top-down view. a) Initially, little swelling has occurred and the surface is intact, although very slight defects can be seen at high magnification. b) As swelling occurs, breaks in the surface appear, exposing the fibers. c) With increased swelling, breaks expand. d) At high fluence, the surface film is observed to crack and spall off.

The non-uniform removal of the surface film indicates that sputtering is not solely responsible for the removal of the layer. As mentioned previously, the probability of nuclear interaction between a high-energy ion within a ~20 nm thick solid layer can be fairly low; for example, a 10 MeV Si^{+} ion produces roughly 0.02 vacancies per ion per Å in Si at a depth of 20 nm, as predicted by TRIM simulations. However, TRIM simulations estimate that a 1 MeV Au^{+} ion produces almost 3.8 vacancies per ion per Å at a depth of 20 nm in solid GaSb, so clearly sputtering cannot be neglected for the case of 1 MeV Au^{+} irradiation of GaSb. Nonetheless, while the surface layer is removed with

continued ion irradiation, it is removed in an unexpected fashion, indicating that other mechanisms besides sputtering affect the surface evolution.

Vacancy accumulation may play a role in the evolution of the irradiated surface. As shown above, TRIM simulations predict notable vacancy production in the ~20 nm thick surface layer. While vacancy accumulation results in void formation in the bulk material, vacancy accumulation in the thin, almost two-dimensional surface layer would tend to result in the formation of gaps in the surface, such as those seen in Figure 4.4a. With increased fluence, rather than void growth as seen in the bulk, one would expect growth of the surface gaps, such as that seen in Figures 4.4b and 4.4c. In addition to vacancy accumulation, surface energy minimization may play a role in the surface evolution. As sputtering and vacancy accumulation begin to create gaps in the surface, surface energy would be minimized by formation of few large surface gaps rather than large numbers of very small surface gaps, which may help explain the evolution of large gaps at increasing fluence as seen in Figure 4.4a-d. Finally, visual evidence of surface layer peeling and cracking, as seen in Figure 4.4d, indicates that some stresses exist between the surface layer and the underlying fibers. While swelling of the fiber layer is constrained at the substrate, swelling is unconstrained at the edges of the irradiated sample, which may result in some small stresses being imparted to the surface layer as the underlying fiber layer expands.

Clearly, given the observed surface layer effects and the vacancy production rates predicted by TRIM, 1 MeV Au^+ irradiation of GaSb does not fall fully within the high-energy irradiation regime as outline in Figure 4.3. Instead, the evolution of the fiber and surface morphologies is best described by a combination of Nitta's low-energy model and

the high-energy model presented in Figure 4.3.[6] While the precise mechanisms for surface layer evolution are not completely understood, it is evident that ion energy plays a large role in the thickness and stability of the surface. By controlling the incident ion energy, as well as atomic number and ion fluence, embedded fiber layers may be formed where surface removal effects are mitigated to the best degree possible.

4.2 FIB Irradiation

4.2.1 Surface and Embedded Structures

As discussed in Section 4.1.1, Nitta's formation model for porosity in GaSb is only valid for low energy ion irradiation regimes.[6,10] To confirm the current model for low energy ions, ion irradiation with 30 keV Ga^+ ions was performed with *in situ* SEM. The results from the *in situ* experiments, shown in Figure 4.6, effectively confirm Nitta's model. At first, low energy ions create a thin porous layer directly beneath the surface (Figure 4.6b). As ion fluence increases, the surface layer is breached, exposing the thin porous region (Figure 4.6c-4.6e). Eventually at higher ion fluence, the porous structures grow outwards, as first shown by Callec *et. al.*,[15] developing into a well defined area of surface nanofibers (Figure 4.6f).

Figure 4.7 shows a GaSb surface irradiated at room temperature to ion fluences of 1×10^{15}, 1.5×10^{15}, and 3×10^{15} ions/cm^2 (17.1, 25.6, and 51.2 dpa). Also shown are XSEM images showing the depth of the porous layer formed as a result of the irradiation. Although the depth of the porous layer increases with increasing ion fluence, a small porous layer of a depth of about 150 nm is formed by ion irradiation to 1×10^{15} ions/cm^2 (Figure 4.7a). At this ion fluence, a subsurface porous layer is formed, with a thin,

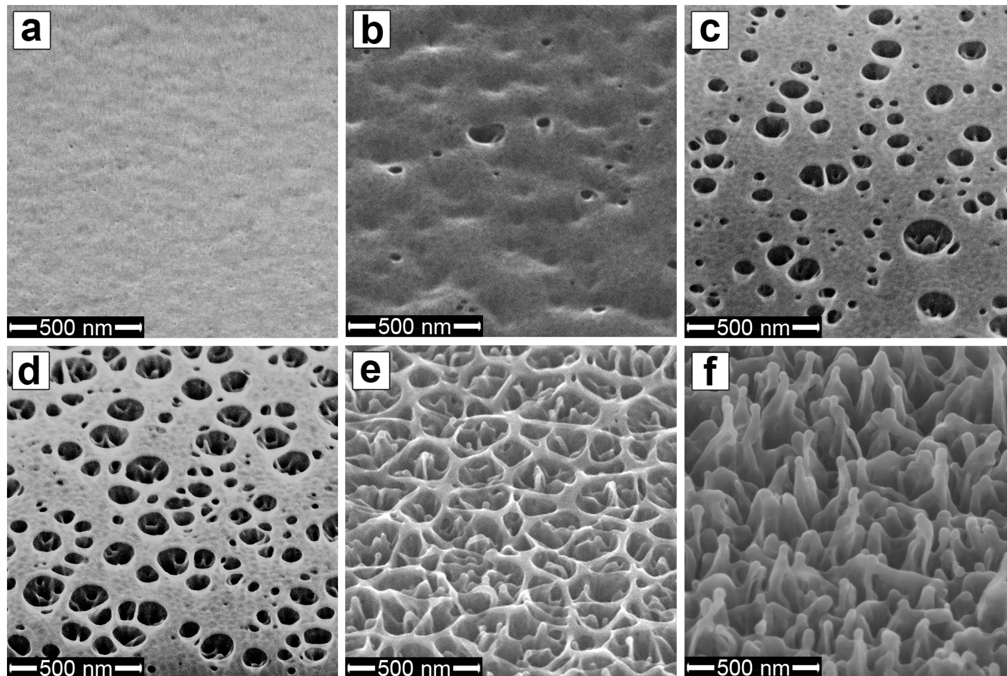

Figure 4.6. *In situ* SEM observation of GaSb surface under FIB irradiation with 30 keV Ga^+ ions. Irradiation fluence is: a) Unirradiated, b) 1×10^{15} ions/cm^2, c) 1.3×10^{15} ions/cm^2, d) 1.6×10^{15} ions/cm^2, e) 2.6×10^{15} ions/cm^2, f) 6.5×10^{15} ions/cm^2. Surface morphology supports the current model for low energy ion irradiation, showing the initial formation of porosity just underneath the surface followed by surface exposure and fiber formation. Samples are shown tilted to 52°.

uniform surface film covering the affected region. However, comparison with other areas irradiated to higher ion fluences (Figure 4.7b and 4.7c) shows that the thin subsurface porous layer shown in Figure 4.7a is not fully developed, and the layer's properties may vary greatly from that of a fully developed porous region, such as those seen in samples irradiated with 1 MeV Au^+ ions. For this reason, although GaSb embedded porous layers are possible through FIB techniques, their structure is noticeable different than those fabricated with higher energy ions and therefore cannot be deemed nanofibrous.

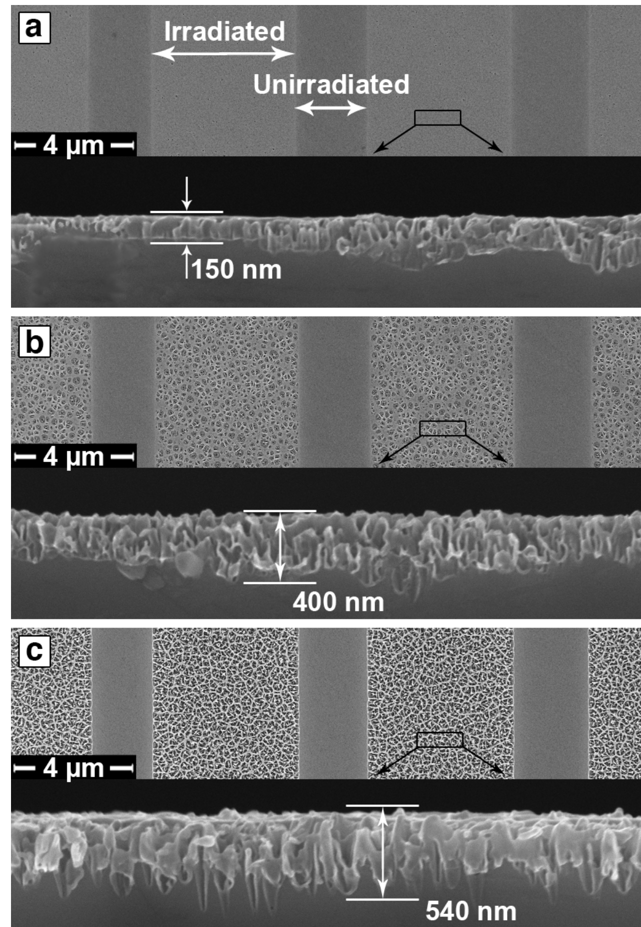

Figure 4.7. Plan view and XSEM images of GaSb irradiated to a) 1×10^{15}, b) 1.5×10^{15}, and c) 3×10^{15} ions/cm^2. Irradiated areas in a) contain porosity that is completely enclosed under a thin surface film, while irradiated areas in b) and c) exhibit porosity that is starting to be exposed to the surface.

4.2.2 Size and Pattern Control

With recent technological improvements in semiconductor microdevice manufacturing, FIB techniques have become increasingly important both in production and repair of microdevices due to their ability to modify very small spatial regions and their ability to have computer-controlled FIB milling and patterning. To test the size limitations of our FIB system for patterning ion irradiation-induced porous areas, rectangular areas of decreasing size were irradiated with ions to a dose sufficient to produce a well-developed porous region (about 5×10^{15} ions/cm^2 or 85.2 dpa). Ion beam

currents of 0.5-1 nA were used in the larger patterned areas, with a minimum current of 1 pA used in the smallest patterned areas. The results of the irradiations are shown in Figure 4.8a. Despite an ion beam spot size of just 7 nm, the smallest possible patterned area was a line of 175 nm in width, indicating that the limiting factor in size control of patterned GaSb porous structures is not the size of the FIB but the size of the self-organizing pores. In general, the homogeneity of the porous region was inconsistent, with a tendency for the pores to order themselves in larger cells with relatively thick walls, and patterned edges and corners were rounded and imprecise. Computer-controlled milling of larger designs, such as the University of Michigan logo shown in Figure 4.8b, resulted in equally imprecise pattern formation.

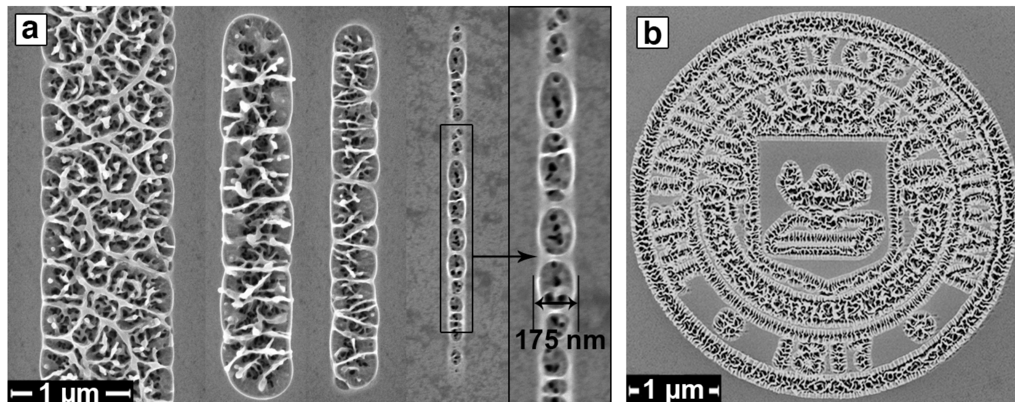

Figure 4.8. SEM images of FIB milled GaSb irradiated to ~ 5 × 10^{15} ions/cm^2. a) Ion beam currents decrease from 0.54 nA (at far left) to 1 pA (at far right). Irradiation results in fairly irregular patterned regions with minimum pattern sizes of ~175 nm. b) Patterned University of Michigan logo, with minimum feature size of ~200 nm, irradiated with a beam current of 0.5 nA.

Bibliography

1. P. S. Dutta, H. L. Bhat, and V. Kumar, The Physics and Technology of Gallium Antimonide: An Emerging Optoelectronic Material. *J. Appl. Phys*. **81**, 5821 (1997).

2. S. Facsko, T. Dekorsy, C. Koerdt, C. Trappe, H. Kurz, A. Vogt, and H. L. Hartnagel, Formation of Ordered Nanoscale Semiconductor Dots by Ion Sputtering. *Science* **285**, 1551 (1999).

3. A. W. Bett, F. Dimroth, G. Stollwerck, and O. V. Sulima, III-V Compounds for Solar Cell Applications. *Appl. Phys. A* **69**, 119 (1999).

4. D. Martín, C. Algora, V. Corregidor, and A. Datas, Development of GaSb Photoreceiver Arrays for Solar Thermophotovoltaic Systems. *J. Sol. Energy Eng.* **129**, 283 (2007).

5. R. Callec and A. Poudoulec, Characteristics of Implantation-induced Damage in GaSb. *J. Appl. Phys.* **73**, 4831 (1993).

6. N. Nitta, M. Taniwaki, Y. Hayashi, and T. Yoshiie, Formation of Cellular Defect Structure on GaSb Ion-implanted at Low Temperature. *J. Appl. Phys*. **92**, 1799 (2002).

7. S. M. Kluth, J. D. Fitz Gerald, and M. C. Ridgway, Ion-induced Porosity in GaSb. *Appl. Phys. Lett*. **86**, 131920 (2005).

8. R. Callec, A. Poudoulec, M. Salvi, H. L'Haridon, P. N. Favennec, and M. Gauneau, Ion Implantation Damage and Annealing in GaSb. *Nucl. Instrum. Methods Phys. Res. B* **80/81**, 532 (1993).

9. L. M. Wang and R. C. Birtcher, Amorphization, Morphological Instability and Crystallization of Krypton Ion Irradiated Germanium. *Philos. Mag. A* **64**, 1209 (1991).

10. N. Nitta and M. Taniwaki, Novel Nano-fabrication Technique Utilizing Ion Beam. *Nucl. Instrum. Methods Phys. Res. Sect. B* **206**, 482 (2003).

11. E. Le Bourhis and G. Patriarche, TEM-nanoindentation Studies of Semiconducting Structures. *Micron* **38**, 377 (2007).

12. R. Maranganti and P. Sharma, Length Scales at which Classical Elasticity Breaks Down for Various Materials. *Phys. Rev. Lett.* **98**, 195504 (2007).

13. G. J. Dienes and A. C. Damask, Radiation Enhanced Diffusion in Solids. *J. Appl. Phys*. **29**, 1713 (1958).

14. S. K. Mohanta, R. K. Soni, N. Gosvami, S. Tripathy, and D. Kanjilal, Morphological

and Micro-Raman Investigations on Ar^+-ion Irradiated Nanostructured GaAs Surface. *Appl. Surf. Sci.* **253**, 4531 (2007).

15. R. Callec, P. N. Favennec, M. Salvi, H. L'Haridon, and M. Gauneau, Anomalous Behavior of Ion-implanted GaSb. *Appl. Phys. Lett.* **59**, 1872 (1991).

Chapter 5

Ion Irradiation of Ge

Germanium is a semi-metallic semiconductor that has a long history in the electronics industry. Ge was used in the development of the first transistor in 1948,[1] and was used throughout the electronics industry until the 1970s when process improvements in the production of high-purity Si caused Ge to be used more sparingly. Since then, Ge has been primarily used in fiber optics, infrared optics, and polymerization catalysts, though recently Ge has increasingly been used for solar cell applications.[2] In this chapter, the effects of ion irradiation in Ge are studied in high and low ion energy regimes.

5.1 High Energy Ion Irradiation

5.1.1 Formation of Nanocellular Structures

Following high-energy Au^+ irradiation at room temperature to fluences of greater than about 1×10^{15} ions/cm^2 (36.3 dpa), the Ge surface self-organized into a nanocellular structure as initially described by Wilson, Holland *et. al.*, and Wang and Birtcher.[3-5] Figure 5.1 shows a plan view image of the structure shortly after formation, irradiated with 3 MeV Au^+ ions at a fluence of 1×10^{15} ions/cm^2. Although no actual ordering is present, the pores are fairly evenly distributed, with an average diameter of ~23 nm. An increase in ion fluence

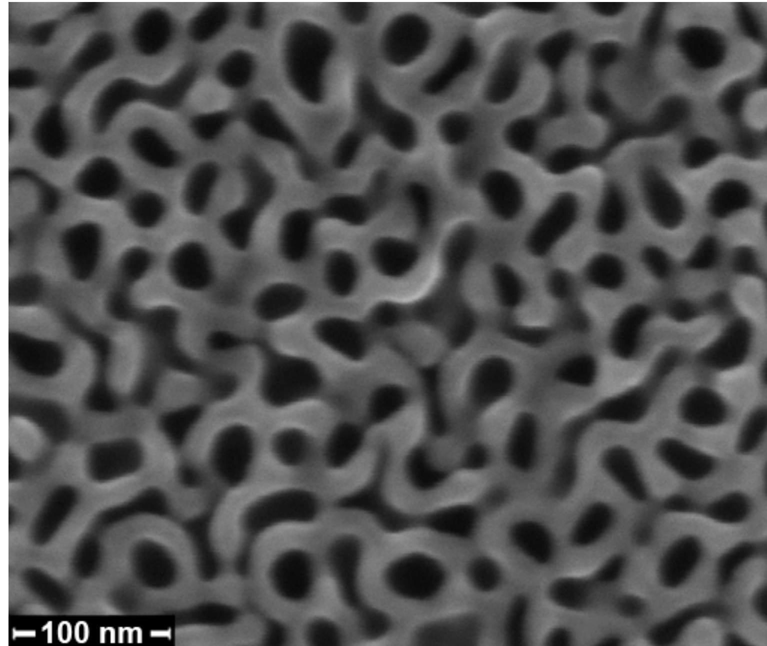

Figure 5.1. Plan view SEM image of Ge irradiated with 3 MeV Au^+ ions at a fluence of 1×10^{15} ions/cm^2, resulting in formation of a nanocellular structure. Dark areas represent void space, and lighter areas are cell walls.

caused a slight but noticeable increase in pore size, although a direct comparison is inaccurate due to the changing morphology of the structure during irradiation.

Figure 5.2 shows cross-sections of Ge samples irradiated with 1 MeV Au^+ ions at ion fluences of 1×10^{15}, 2.2×10^{15}, and 6×10^{15} ions/cm^2 (36.3, 79.8, and 217.7 dpa, respectively), and the images illustrate some of the problems in trying to define the size of the pores. Initially, the porous structure is confined to the immediate near-surface region, and the pores, though somewhat oblong, do not vary drastically along their various dimensions (Figure 5.2a). As the ion fluence increases, the pores grow parallel to the ion beam direction but not radially to the beam direction, resulting in cylindrical void structures (Figure 5.2b). At even higher ion fluence, the individual cells begin to degrade into an intertwined, porous structure (Figure 5.2c). Overall, however, increasing the ion

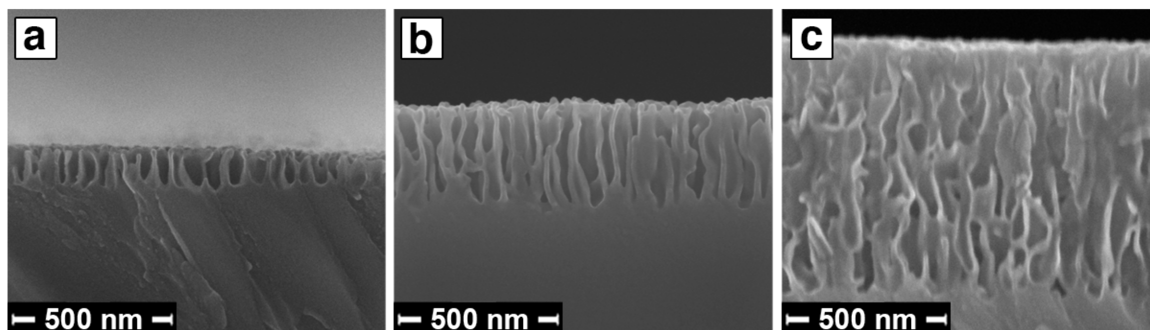

Figure 5.2. XSEM images of Ge irradiated with 1 MeV Au^+ ions at ion fluences of a) 1 × 10^{15}, b) 2.2 × 10^{15}, and c) 6 × 10^{15} ions/cm^2. Increasing ion dose results in thicker fiber layers and changes in the void structure.

fluence results in larger pores and more entwined cell walls. For more data on Ge pore and cell wall size as a function of irradiation fluence and ion energy, see Appendix 1.

As shown in Figure 5.2, in addition to causing changes in the structure morphology, an increase in ion fluence results in the formation of progressively thicker porous layers. The samples shown in Figure 5.2 that had been irradiated to fluences of 1 × 10^{15}, 2.2 × 10^{15}, and 6 × 10^{15} ions/cm^2 displayed porous layer thicknesses of ~125, 310, and 850 nm, respectively. Samples irradiated to a fluence of 9 × 10^{15} ions/cm^2 exhibited an even thicker porous layer and a more developed porous structure, although the fundamental columnar pore structure still remained.

When comparing samples that were irradiated to a uniform fluence of 2 × 10^{15} ions/cm^2 using 1, 2, and 3 MeV Au^+ ions (penetration depths of 160, 308, and 457 nm as predicted by TRIM, respectively), the porous layer thickness surprisingly decreased with increasing ion energy. While the 1 MeV Au^+ sample had a 310 nm thick porous layer, the sample irradiated with 3 MeV Au^+ only had a 140 nm thick porous layer. This can perhaps be explained by the fact that higher energy ions initially lose more of their kinetic energy through electronic interactions in the target surface, which do not result in

atomic displacements that lead to point defect and void formation. However, one would expect higher energy ions to create more point defects overall within the bulk solid, perhaps leading to the formation of embedded Ge porous layers, as seen in the literature[6] and in GaSb (Section 4.1.1).

TEM investigation of the Ge cellular structure confirmed that the cell walls are amorphous, which is consistent with literature observations.[7] Figure 5.3a shows a high contrast TEM image of the irradiated Ge surface along with SAED images of the fibrous region and underlaying crystalline substrate. The high contrast image gives an easy visual boundary between the amorphous and crystalline regions, which is indicative of the ion damage distribution. EDS confirmed that the fibers were composed of Ge without any significant impurities. This could also be seen via high-angle annular dark field (HAADF) imaging in STEM mode as seen in Figure 5.3b; the nanofibers exhibited only thickness contrast, indicating a uniformity in elemental composition.

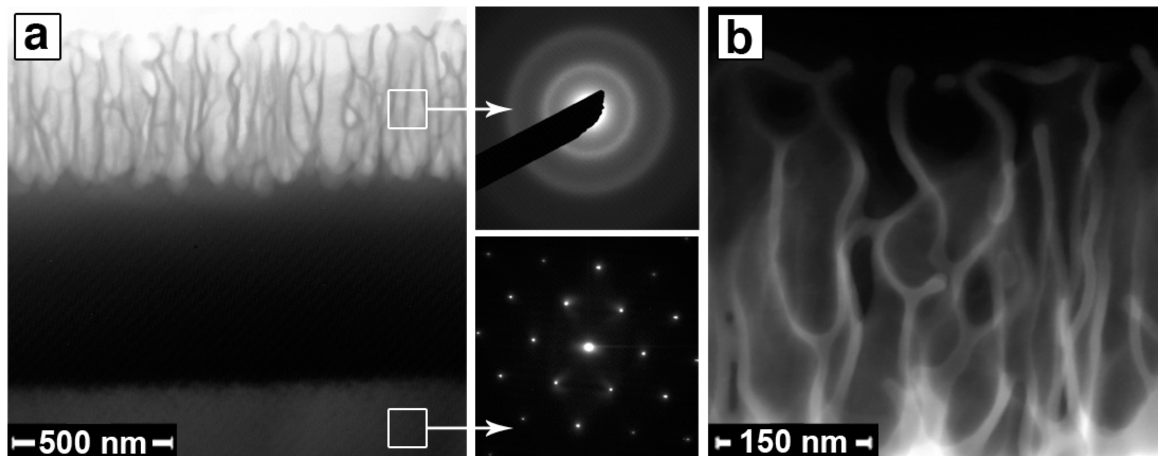

Figure 5.3. TEM images of irradiation-induced Ge fibers fabricated by 1 MeV Au^+ ion irradiation of Ge to a fluence of 2.2×10^{15} ions/cm^2. a) High contrast XTEM image showing, from top to bottom, the amorphous Ge fibers, a solid amorphous layer, and the crystalline substrate. SAED images corresponding to the regions are shown. b) HAADF STEM image of the Ge fibers shown in a) displaying only thickness contrast.

5.2 FIB Irradiation

5.2.1 Ge Surface Evolution under FIB

Nanocellular porous structures begin to form following room temperature 30 keV Ga^+ FIB irradiation of Ge to fluences of about 1×10^{15} ions/cm^2 (13.6 dpa), similar to samples irradiated with higher energy ions. Initially, the sample surface appears pock-marked but quickly develops into the familiar cellular structure (Figure 5.4a,b,c). At around 6.25×10^{15} ions/cm^2 (106.5 dpa), the irradiation-induced voids begin to coalesce, causing the cellular structure to degrade into a more porous structure similar to those seen in irradiated GaSb (Figure 5.4d,e). Continued irradiation above 1×10^{16} ions/cm^2 (170.5 dpa) results in further growth of the voids and additional degradation of the remaining cell walls and connecting nanofibers (Figure 5.4f,g,h). Unlike in high-energy ion irradiated Ge, which resulted in substantial longitudinal growth of voids, the low penetration depth of the incoming 30 keV Ga^+ ions results in an immediate structural transition from individual near-surface voids to a fully porous structure. In addition, sputtering and redeposition effects are almost certainly partially responsible for the morphology of the Ge surface at high fluence. Though the surface continues to change in response to increased ion fluence, the overall surface morphology at doses higher than 1×10^{16} ions/cm^2 remains very similar to that seen in Figure 5.4h.

Though limited embedded porosity was possible through FIB irradiation of GaSb (Section 4.2.1), the same is not possible in Ge. Figure 5.5a shows a FIB irradiated Ge sample containing both high and low dose regions, and Figure 5.5b shows an XTEM image of the corresponding irradiated region. In both the low and high dose regions, regardless of the structure of the cell walls, the pores remain exposed to the surface.

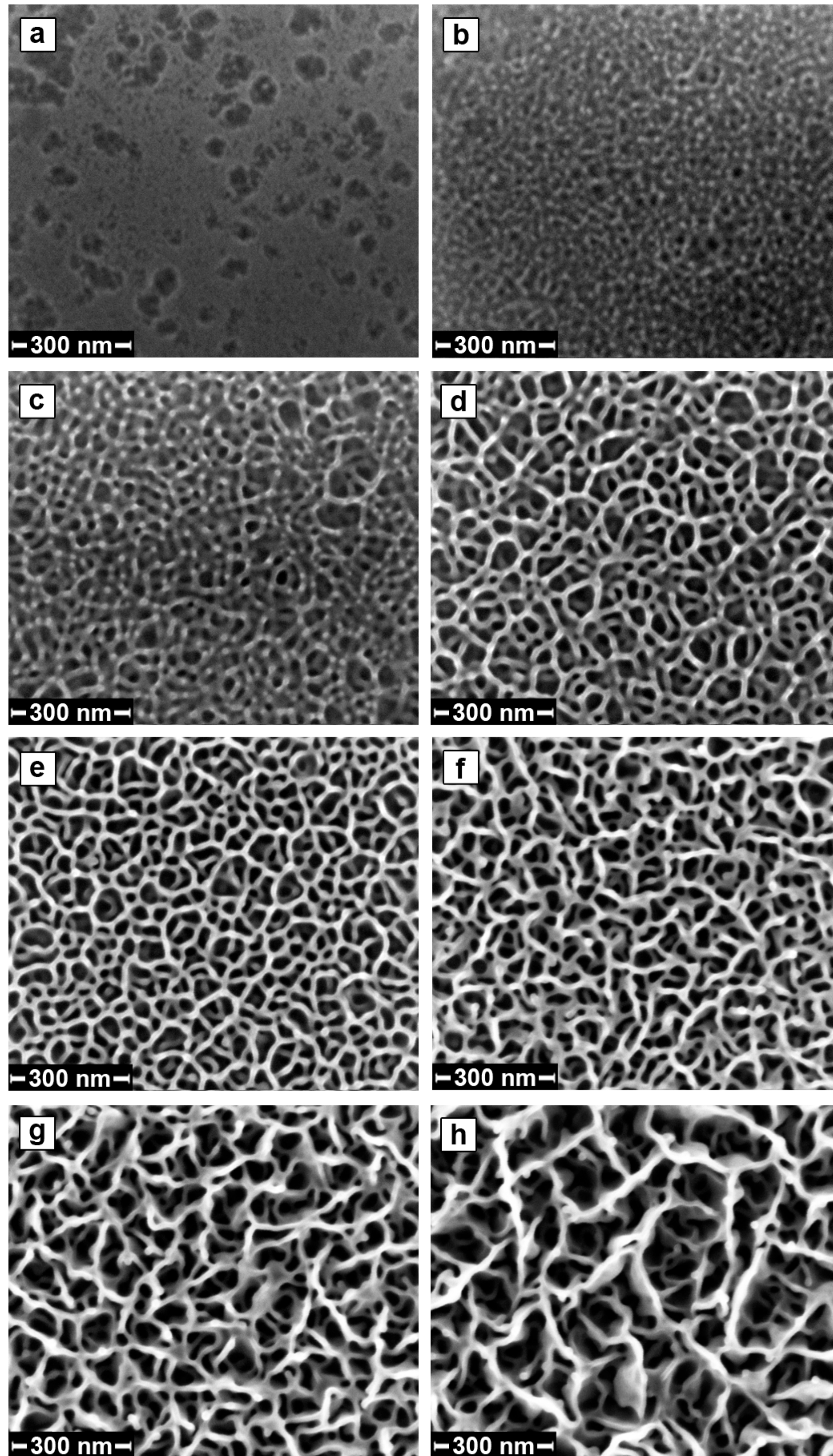

Figure 5.4. Plan view SEM images of Ge irradiated *in situ* with 30 keV Ga^+ to doses of a) 1.875, b) 3.175, c) 5.625, d) 6.25, e) 9.375, f) 18.75, g) 25, and h) 50×10^{15} ions/cm^2.

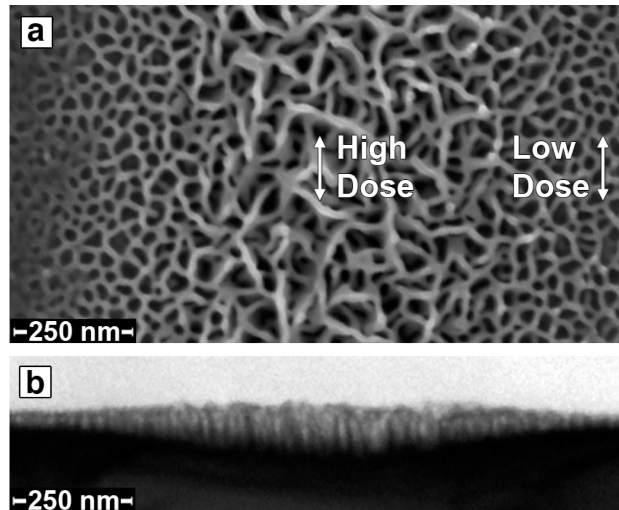

Figure 5.5. Ge fibers formed by FIB irradiation. a) Plan view SEM image showing the FIB irradiated Ge surface. b) XTEM image of the same region, showing pores exposed to the surface across the sample length. "High dose" regions irradiated at ~ 2.5×10^{16} ions/cm^2 (476.2 dpa) and "low dose" regions irradiated at ~ 6×10^{15} ions/cm^2 (102.3 dpa)

Although embedded porous structures may not be feasible in current FIB systems due to their low ion energies, they can be fabricated at higher ion energies.[6]

5.2.2 Size and Pattern Control

Current publications show that there is already considerable interest in the ability to use FIB technology to manufacture Ge microdevices.[8,9] Size and pattern control are clearly important factors in the manufacture of such microdevices. For example, current generation silicon transistor technology consists of the reliable production of 45 nm silicon transistors, with 35 nm transistor gate lengths and oxide coatings of as thin as 1 nm.[10] If irradiation-induced porous semiconductor technology were to be integrated with current lithography-based semiconductor manufacturing technology, irradiation of porous areas would need to not only be capable of producing sub-100 nm porous regions but also be extremely precise in patterning.

To test the size limitations of our FIB system for patterning ion irradiation-induced porous regions, rectangular areas of decreasing size were irradiated with ions to a dose sufficient to produce a well-developed porous region (about 2×10^{16} ions/cm^2 or 341 dpa). Ion beam currents of ~0.5-1 nA were used in the larger patterned areas, with a minimum current of 1 pA used in the smallest patterned areas. The results of the irradiations are shown in Figure 5.6a.

The porous cellular structures formed in germanium have a very uniform internal distribution of pores and result in very well defined patterned areas, with crisp edges and corners even at the smallest fabricated sizes. Using an ion beam spot size of 7 nm, the smallest possible patterned area was a line of 100 nm in width, which contained 2 to 3 voids and 1 to 2 cell walls along the width of the line. As mentioned for GaSb, the minimum size of the structure seems to be dictated not by the beam spot size but by the self-forming sizes of the pores themselves. Semantically, the smallest possible porous region need be defined as two pores separated by a cell wall, which in the case of Ge would be a region only slightly thinner than that shown in Figure 5.6a. Therefore, with a very well defined ion beam and fine control of the ion beam current, it may be possible to decrease the size of the pattered area even further, but the size limitation for porous structures in Ge seems to be ~75 nm. Computer-controlled milling of larger, more complex designs resulted in very neat, uniform patterns (Figure 5.6b). Even very small irradiated patterns with sharp edges between porous and fully dense regions were possible (Figure 5.6c), unlike the FIB irradiated GaSb patterns of Section 4.2.2.

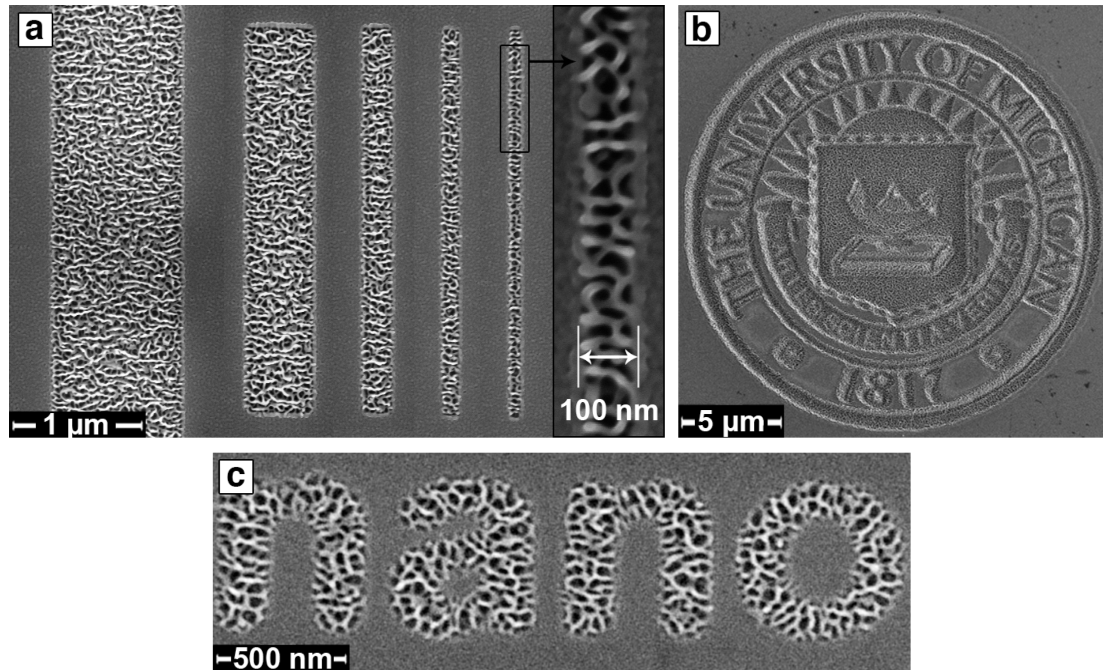

Figure 5.6. SEM images of FIB milled Ge irradiated to ~ 2×10^{16} ions/cm^2. a) Ion beam currents decrease from 0.5 nA (at far left) to 1 pA (at far right). Ge forms very well defined regions, with pattern sizes of less than 100 nm possible. b) Irradiated with a beam current of 1 nA. Large patterns are clean and easily recognizable. c) Irradiated with a beam current of ~0.1 nA. Small patterns show that there is a very sharp distinction between the irradiated and virgin regions.

Bibliography

1. J. Bardeen and W. H. Brattain, The Transistor, A Semiconductor Triode. *Phys. Rev.* **74**, 230 (1948).

2. D. E. Guberman, Germanium. U.S. Geological Survey, Mineral Commodity Summaries (January 2009).

3. I. H. Wilson, The Effects of Self-ion Bombardment (30-500 keV) on the Surface Topography of Single-crystal Germanium. *J. Appl. Phys.* **53**, 1698 (1982).

4. O. W. Holland, B. R. Appleton, and J. Narayan, Ion Implantation Damage and Annealing in Germanium. *J. Appl. Phys.* **54**, 2295 (1983).

5. L. M. Wang and R. C. Birtcher, Radiation-induced Formation of Cavities in Amorphous Germanium. *Appl. Phys. Lett.* **55**, 2494 (1989).

6. H. Huber, W. Assmann, S. A. Karamian, A. Mücklich, W. Prusseit, E. Gazis, R. Grötzschel, M. Kokkoris, E. Kossionidis, H. D. Mieskes, and R. Vlastou, Void Formation in Ge Induced by High Energy Heavy Ion Irradiation. *Nucl. Instrum. Methods Phys. Res. B* **122**, 542 (1997).

7. B. Stritzker, R. G. Elliman, and J. Zou, Self-ion-induced Swelling of Germanium. *Nucl. Instrum. Methods Phys. Res. B* **175-177**, 193 (2001).

8. S. Rubanov and P. R. Monroe, The Application of FIB Milling for Specimen Preparation from Crystalline Germanium. *Micron* **35**, 549 (2004).

9. S. Ichim and M. J. Aziz, Lateral Templating of Self-organized Ripple Morphologies During Focused Ion Beam Milling of Ge. *J. Vac. Sci. Technol. B* **23**, 1068 (2005).

10. D. Lammers, Intel Takes 45 nm HKMG Process to IEDM. *Semiconductor International*, Dec. 14, 2007. Accessed from web: Mar. 25, 2010.

Chapter 6

Ion Irradiation of InSb

Ever since the discovery of semiconducting intermetallic compounds in the 1950s,[1] InSb has been widely investigated for use in infrared photovoltaic detectors and photodiodes.[2] Although ion implantation is an attractive way to fabricate junctions in many semiconductor devices, ion irradiation of InSb has long been known to create extended void defect networks in the material, resulting in the formation of highly porous nanostructures.[3,4] In this chapter, the effects of ion irradiation in InSb are studied in high and low ion energy regimes.

6.1 High Energy Ion Irradiation

6.1.1 Embedded InSb Nanofibers

Figure 6.1 shows an XSEM image of an InSb sample irradiated at room temperature with 1 MeV Au^+ ions to a fluence of 1.25×10^{14} ions/cm^2 (7.7 dpa). The figure highlights three distinct regions of the porous layer: a highly buckled yet continuous surface layer, a fiber regime where the material is composed of fairly uniformly sized and distributed InSb fibers, and a formation regime, composed of numerous small voids embedded within a continuous InSb matrix. Figure 6.2 shows bright field (BF) TEM images of the InSb porous layer. TEM EDS performed on

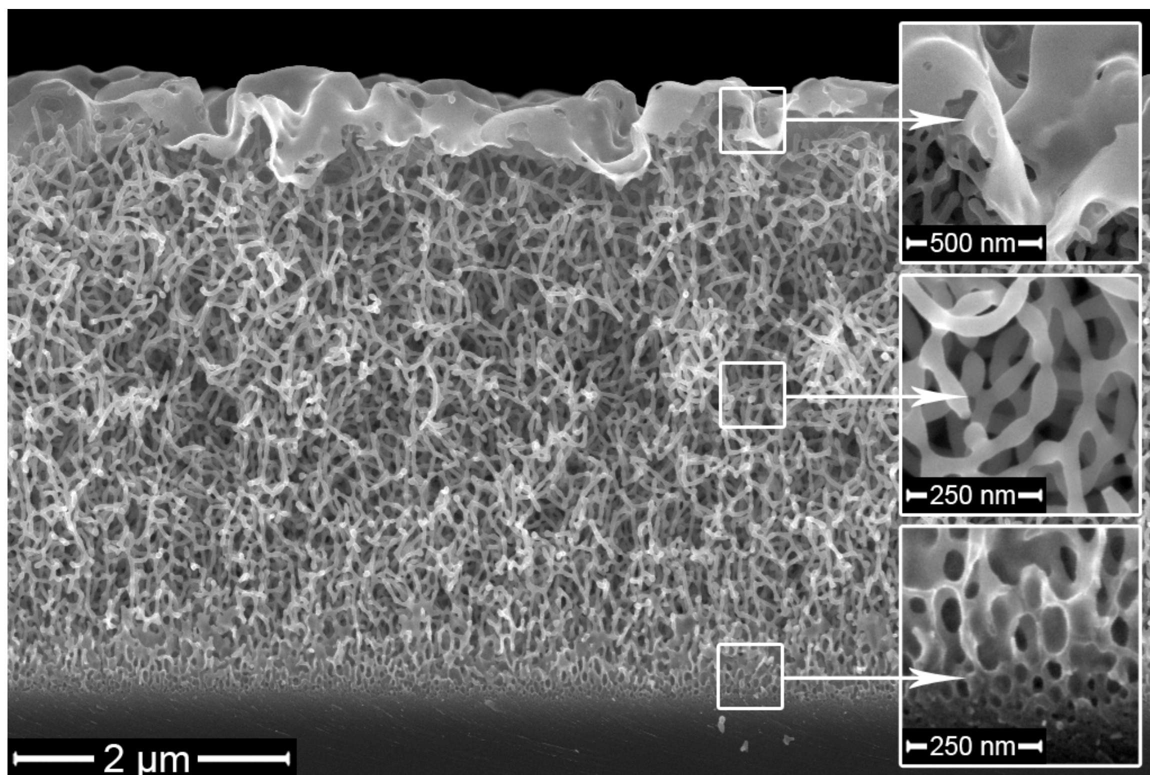

Figure 6.1. XSEM image of an InSb sample irradiated with 1 MeV Au^+ to a fluence of 1.25×10^{14} ions/cm^2. Three distinct regions of the porous layer are visible: a warped yet continuous surface layer, a fiber regime composed of fairly uniform InSb fibers, and a formation regime composed of small voids embedded within a continuous InSb matrix.

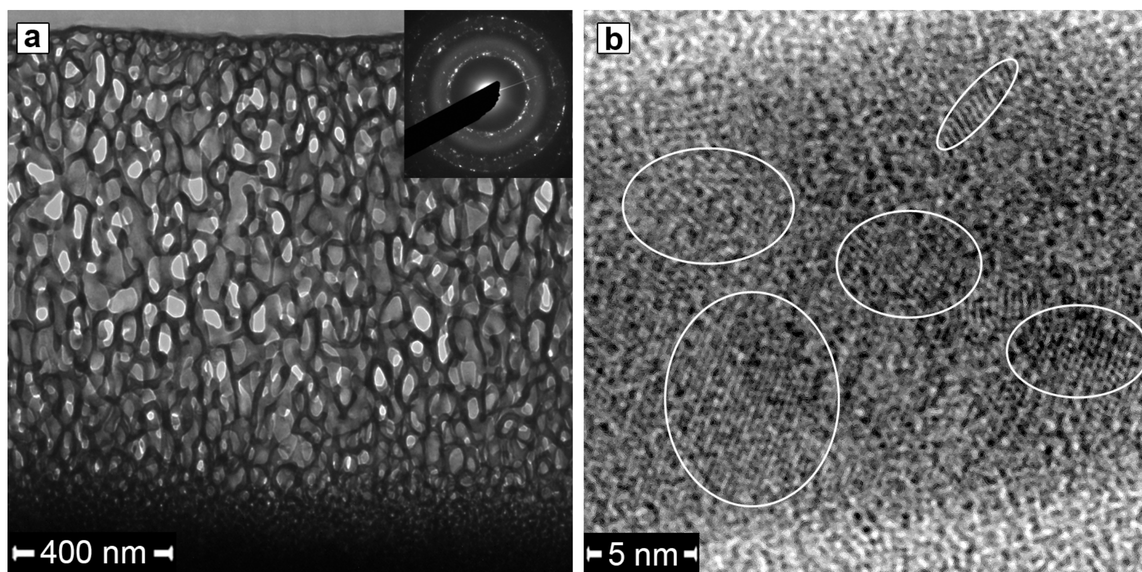

Figure 6.2. TEM images of InSb fibers. a) XTEM BF image of InSb irradiated with 2 MeV Au^+ to a fluence of 5×10^{13} ions/cm^2 (3.1 dpa). b) HRTEM image of an individual InSb fiber/cell wall. Nanocrystalline regions have been highlighted.

individual nanofibers showed that the fibers contained uniform concentrations of In and Sb, and SAED of the fiber volume showed that the fibers are primarily nanocrystalline with some amorphous components (Figure 6.2a). HRTEM imaging performed in a JEOL 3011 showed how the nanofibers contain large quantities of small, randomly oriented nanocrystals (Figure 6.2b). The polycrystalline nature of the diffraction pattern is consistent with results in the literature[5] and indicates that InSb is amorphized by the incoming ions but that small regions recrystallize due to ion beam heating and thermal spike effects in the material. Similarly, SAED and HRTEM of the surface layer showed that the surface layer was nanocrystalline with some amorphous regions, and EDS of the surface also confirmed the composition of the surface film as InSb without any significant impurities.

Experimentation across a wide range of ion energies and fluences seems to show that the formation mechanism of InSb fibers is the same as that for GaSb fibers, which has been well established in the literature and in Section 4.1.1.[6] Succinctly, ion irradiation creates a large vacancy excess in InSb, leading to the accumulation of vacancies into large voids. These voids accumulate to such a large extent that they force the remaining material in the porous layer into thin nanofibers. As the material accumulates voids and expands, the density of the material drops dramatically, allowing energetic incoming ions to pass through the low-density fiber layer without losing much kinetic energy. This allows for the continual formation of new porous material at the interface of the fiber layer and the dense substrate with additional ion irradiation. By irradiating the material with high-energy ions, the fiber layer forms under a continuous surface layer.

The irradiated InSb samples responded very similarly to Ge and GaSb samples in terms of their response to increased ion fluence and ion energy. Samples irradiated to fluences of 5×10^{13}, 1.25×10^{14}, 3×10^{14}, 6×10^{14}, and 8.4×10^{14} ions/cm^2 (3.1, 7.7, 18.4, 36.7, and 51.4 dpa) with 1 MeV Au^+ ions resulted in porous layers of 1.8, 4.4, 8.4, 15.8, and 20.3 μm in thickness, respectively. In addition to the thickness of the layer, noticeable differences were observed in the porous layer morphology at different doses. At 1.25×10^{14} ions/cm^2, distinct nanofibers were visible, but the structure was densely populated with fibers. The average fiber diameter was about 32.5 nm but with a high variance in the measurement (Figure 6.3a). At 8.4×10^{14} ions/cm^2, the fiber density was substantially lower, and fiber diameter was on average about 24.2 nm, with a much lower variance (Figure 6.3b). Fibers also appeared to be better aligned with the orientation of the ion beam. For more data on InSb pore and fiber size as a function of irradiation fluence and ion energy, see Appendix 1. Similar to irradiations in GaSb, InSb samples irradiated with higher energy ions exhibited thicker porous layers, as well. Samples implanted with 1, 2, and 3 MeV Au^+ ions (penetration depths of 180, 343, and 504 nm as predicted by TRIM, respectively) to ~ 1×10^{14} ions/cm^2 possessed porous layer thicknesses of 4.4, 8.6, and 11.8 μm, respectively.

6.1.2 Surface Layer Evolution Under Irradiation

In GaSb, ion irradiation with high-energy ions of several hundred keVs to a few MeVs, depending on the ion species, results in the formation of embedded nanofibers underneath a flat, uniform surface layer. Although embedded fibers can be formed in InSb, the surface layer morphology is textured and varies with both ion energy and ion

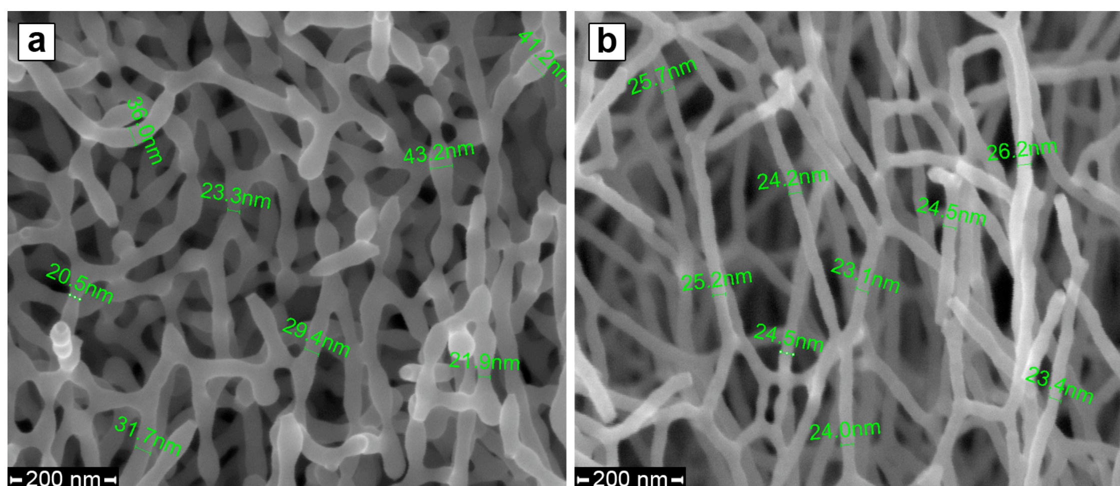

Figure 6.3. XSEM images of InSb nanofibers after 1 MeV Au^+ irradiation to a) 1.25×10^{14} ions/cm^2 and b) 8.4×10^{14} ions/cm^2 showing fiber size as a function of ion fluence.

fluence. Figure 6.4 shows the surface morphology of InSb samples irradiated with 1 and 3 MeV Au^+ ions through plan-view SEM imaging. Irradiation with 1 MeV ions at a fluence of 5×10^{13} ions/cm^2 leads to surface roughening but no observable pattern formation (Figure 6.4a), while increasing the fluence to 1.25×10^{14} ions/cm^2 leads to additional roughening that creates a surface morphology resembling crumpled tissue paper (Figure 6.4b). As ion fluence continues to increase, the surface layer is gradually removed, revealing the nanofibers underneath (Figure 6.4c). With an increase in ion energy, the surface features became markedly more distinct and noticeable, albeit at lower ion fluence. When irradiated with 3 MeV Au^+ ions at a fluence of just 5×10^{13} ions/cm^2, the surface took on a ropy, corrugated appearance (Figure 6.4d). An increase in ion fluence caused the surface layer to be gradually removed and caused the features of the ropy regions to become larger but less distinct (Figures 6.4e, 6.4f). Figure 6.5 visibly displays the bimodal surface structures that can result from the ion irradiation process, showing that at certain combinations of ion fluence and ion energy the larger microscale surface structures are fully composed of individual nanoscale fibers.

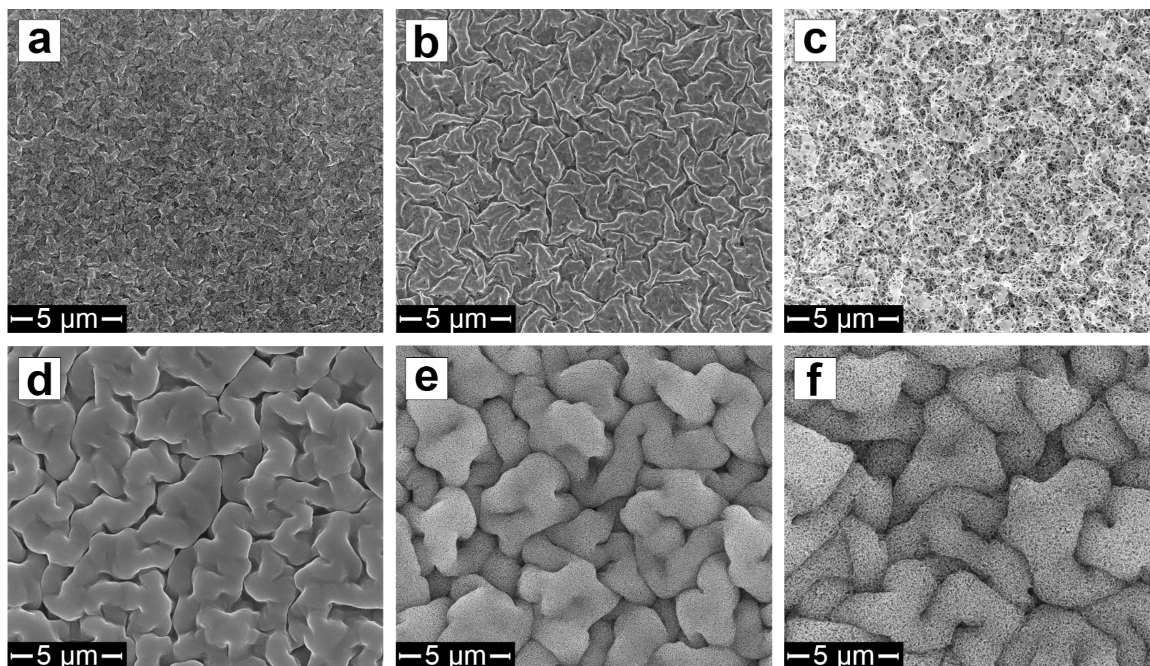

Figure 6.4. Plan-view SEM images of InSb samples irradiated with 1 and 3 MeV Au^+ ions. Samples were irradiated with 1 MeV Au^+ to a) 5×10^{13} ions/cm^2, b) 1.25×10^{14} ions/cm^2, and c) 3×10^{14} ions/cm^2 and with 3 MeV Au^+ to d) 5×10^{13} ions/cm^2, e) 1×10^{14} ions/cm^2, and f) 2×10^{14} ions/cm^2. Sputtering effects can be seen to remove the surface layer with increasing fluence.

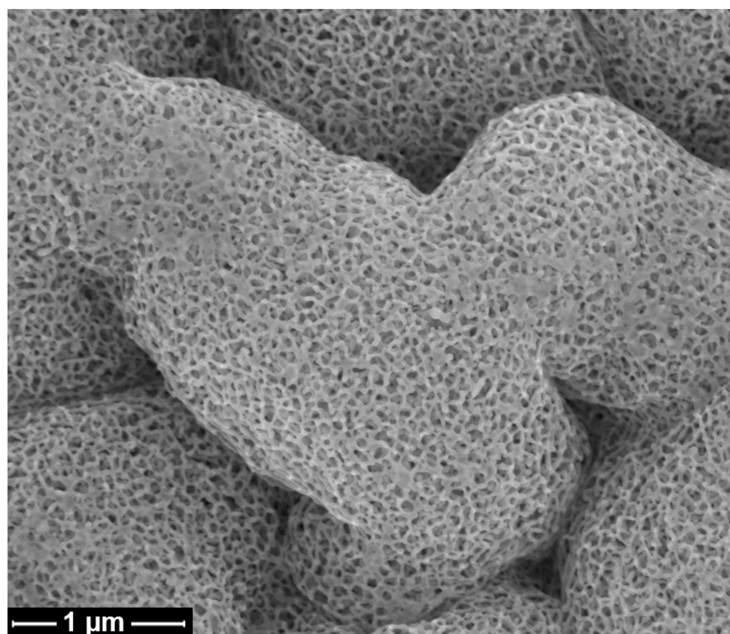

Figure 6.5. Plan-view SEM image of an InSb sample irradiated with 3 MeV Au^+ ions to 1×10^{14} ions/cm^2. The large surface structures are roughly 2 μm across and are composed of nanofibers that are approximately 25 nm in diameter.

When viewed in cross-section, the InSb samples clearly show a thin, continuous surface layer of around 18 nm in thickness covering a broad expanse of nanofibers. Figure 6.6 shows SEM cross-sections of the InSb samples irradiated with 1 MeV and 3 MeV ions at an ion fluence of 5×10^{13} ions/cm^2 with a focus on the interface between the surface layer and the porous layer underneath. The sample irradiated with 1 MeV ions exhibited a maximum peak to valley distance of about 185 nm (Figure 6.6a). When the ion energy was increased to 3 MeV, the maximum peak to valley distance increased to about 1.2 µm (Figure 6.6b). AFM micrographs qualitatively confirmed the SEM data, showing dramatically higher average peak to valley measurements in the sample irradiated with higher energy ions, as well as dramatically lower periodicity of surface structures in the higher energy sample, as seen in Figure 6.7, which shows InSb samples irradiated with 1 MeV Au^+ to a fluence of 1.25×10^{14} ions/cm^2 (Figure 6.7a) and with 3 MeV Au^+ to a fluence of 5×10^{13} ions/cm^2 (Figure 6.7b).

Overall, increasing the incident ion energy caused an increase in surface structure size and, consequently, a decrease in surface structure areal density. Qualitatively, the effects of incident ion energy on the InSb surface make some sense, as higher energy ions are able to displace more lattice atoms and should be able to create larger defect structures than low energy ions. Quantifying the effects of ion fluence is more difficult due to the narrow range of fluences under which samples with discrete surface layers were observed. Although an increase in ion fluence from 5×10^{13} to 1.25×10^{14} ions/cm^2 was observed to cause an increase in surface roughness in the 1 MeV Au^+ irradiated samples, the most obvious effect of increased fluence across the sample sets was the removal of the surface layer due to atomic sputtering, as seen in Figure 6.4. Due to the

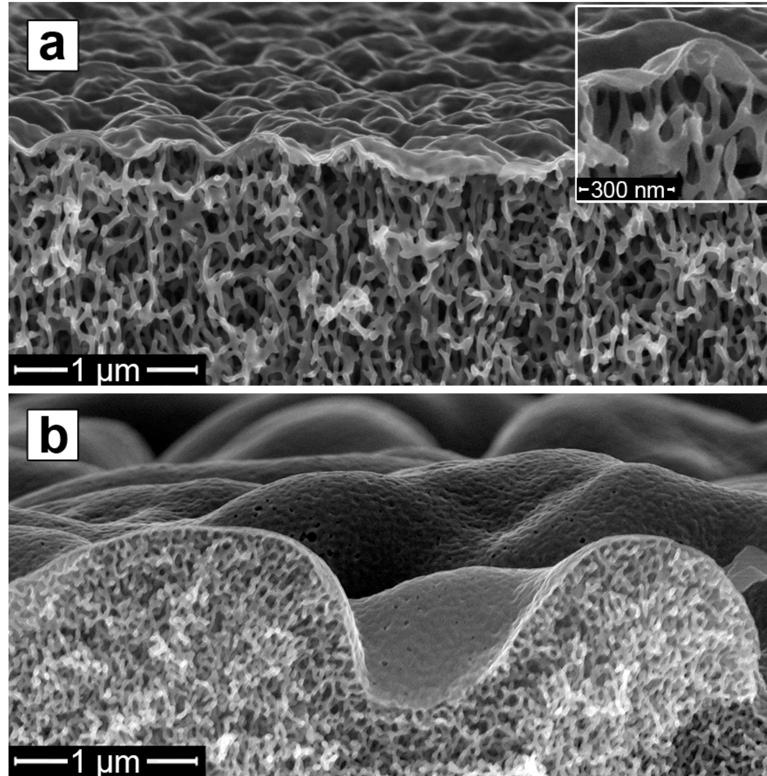

Figure 6.6. XSEM images of the interface between the surface layer and porous layer in InSb samples irradiated with a) 1 MeV and b) 3 MeV Au^+ ions at 5 × 10^{13} ions/cm^2. Insert shows a close-up of the attachment of the fibers to the surface. Images were taken at an angle of 10° from the cross-section surface to better illustrate surface topography.

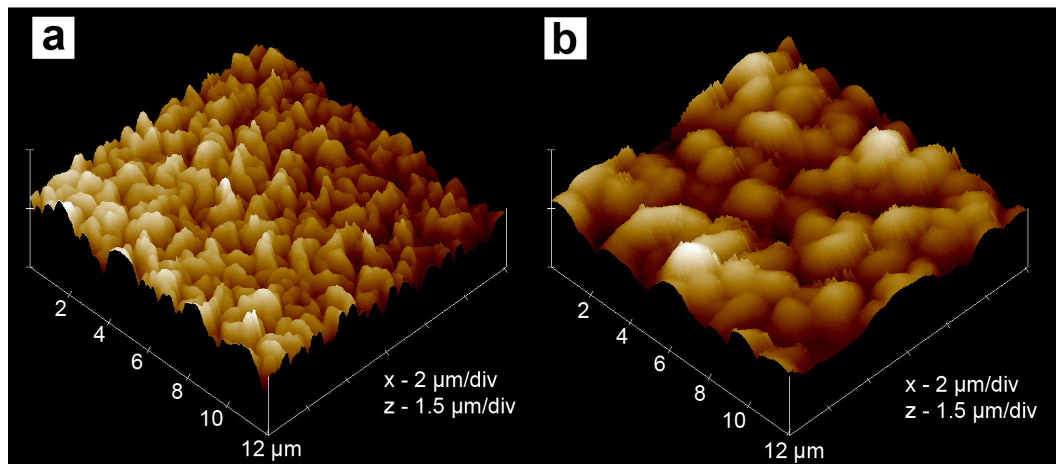

Figure 6.7. AFM micrographs of InSb surfaces irradiated with a) 1 MeV Au^+ ions at 1.25 × 10^{14} ions/cm^2 and b) 3 MeV Au^+ ions at 5 × 10^{13} ions/cm^2. Grid dimensions are marked in the figure.

fact that both ion energy and fluence directly affect the total energy deposition and dpa of the InSb target, it is difficult to separate the effects of the two parameters. However, the combined total effects of ion damage can be seen by comparing the porous layer thickness to the surface roughness of the samples. Figure 6.8 shows the porous layer thickness, t, compared to the surface roughness, R_t, where:

$$R_t = R_p - R_v \tag{6.1}$$

and R_p is the maximum peak height, while R_v is the maximum valley depth. The relatively linear relationship between the two parameters indicates that the evolution of the surface structures is a function of the expansion of the porous layer and is not directly related to either irradiation energy or fluence. Initial surface roughness measurements were made via AFM, but large amounts of noise in several of the AFM micrographs made the data unreliable. As a result, surface roughness data was obtained by manually measuring values for R_p and R_v from XSEM images. Raw surface roughness data for all measured InSb samples is included in Appendix 4, along with statistical analysis of the error involved in the measurements.

For very high-energy ions, surface sputtering and erosion become negligible, but surface modification can still occur due to electronic energy deposition and ionization by incoming ions. Numerous studies have shown that high-energy ion irradiation of amorphous solids results in viscous flow leading to anisotropic growth perpendicular to the ion beam direction, resulting in expansion of thin films normal to the ion beam and shrinkage parallel to the beam.[7-10] Of course, the case of high-energy ion irradiation of InSb is unique in that volume expansion of the porous layer actually results in a significant expansion of the surface parallel to the ion beam direction, as first reported by

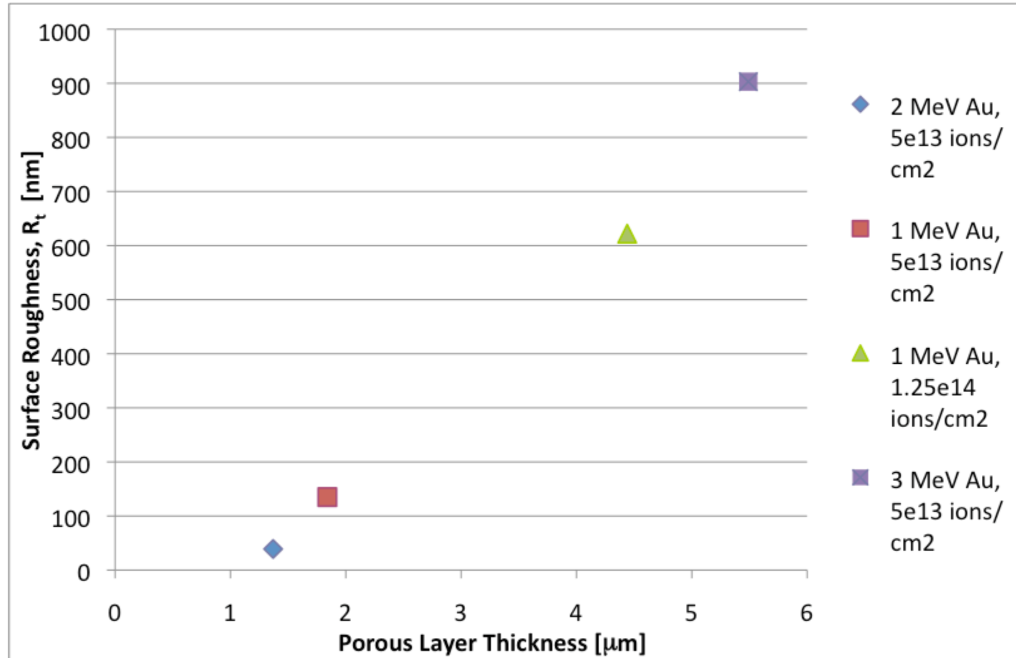

Figure 6.8. Porous layer thickness vs. surface roughness for InSb samples exhibiting both a porous layer and a discrete surface layer. Measurements made by XSEM.

Destefanis *et. al.* and shown in Figure 6.9.[11] Clearly, irradiation of InSb results in notable expansion of the porous layer outwards, in addition to growth of porosity into the substrate. Also, anisotropic growth of the surface layer covering the porous InSb region may be limited due to the relatively lower energy range of the experiments (E ≅ 5-15 keV/u) as compared to truly high energy ions (E ≥ 1 MeV/u).

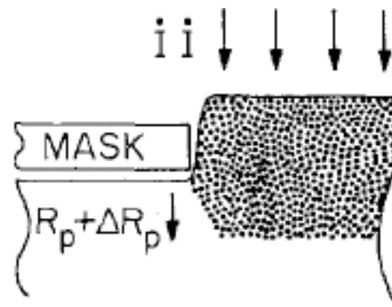

Figure 6.9. Schematic showing observed porous layer placement and outwards expansion of energetic ion implantation of InSb as reported by Destefanis *et. al.*[11]

Although the formation of the porous InSb network is clearly a result of ion irradiation effects, the behavior of the surface layer appears to be a function of mechanical stresses caused by the expansion of the porous layer, as evidenced by the relationship between t and R_t. Experiments have shown that given the proper set of stress conditions in surfaces, various film morphologies can result, from relatively simple buckled surfaces[12,13] to labyrinthine wrinkles[14,15] and bump-like clusters[16,17]. Complex wrinkle structures, in particular, have been observed to form in systems exhibiting a discrete surface film over a compliant substrate that in turn is attached to a rigid support.[15] Such formation is analogous to the irradiation-induced InSb surface, which exhibits a solid InSb film covering a porous fiber network that is in turn attached to a rigid, solid InSb substrate. Depending on the material composition and crystallinity, surface film thickness, and compliant layer thickness, either tensile or compressive stresses can be generated, leading to varying surface curvatures, roughnesses, and structure sizes.[16] Current theory predicting surface layer behavior is for amorphous systems only, and while TEM evidence showed a large number of nanocrystals in the InSb surface layer, their distribution and orientation indicates that the material is amorphized during ion irradiation. Visual data of plastic deformation typical of irradiated amorphous alloys lends credence to this assumption, showing evidence of necking in fibers that attach to the surface film (Figure 6.6a, Insert), and plastic deformation effects have also been seen in high-energy irradiated GaSb in the forms of surface film stretching, delamination, and peeling (see Section 4.1.2).

Additional insight into relaxation processes in the InSb system can be obtained by considering the radially-averaged power spectral density (PSD) of the sample surface:[16]

$$PSD = \left\langle \left| h(\vec{\lambda},t) \right|^2 \right\rangle_{|\vec{\lambda}|=\lambda} \quad (6.2)$$

where $h(\vec{\lambda},t)$ denotes the spatial Fourier transformation of the surface topography. In the long-time limit, the PSD shows a power-law behavior:

$$PSD \propto \frac{1}{\sum_{i=1}^{4} a_i \lambda^i} \quad (6.3)$$

where a_i is a constant and exponents for λ^i are characteristic of atomic surface processes. Based on the shape of the PSD curve, different roughening and smoothening mechanisms can be attributed to formation processes, including plastic flow, bulk diffusion, surface diffusion, and stochastic and non-stochastic roughening.[18] Figure 6.10 shows a log-log plot of PSDs, calculated from the InSb surfaces corresponding to Figure 6.4, as a function of spatial frequency. Figure 6.10 was derived by a visiting scholar in our research group, Dr. Kundar Li, by inputting the individual images of Figure 6.4 into the Matlab computer program, which identifies each image as a grid composed of pixels of varying contrast. PSD data points are then obtained for the image using a Matlab code included in Appendix 5, which directly outputs the graphs of Figure 6.10. For the 1 MeV Au^+-irradiated samples (Figure 6.10a) at 5 $\times 10^{13}$ ions/cm^2, λ^{-1} behavior characteristic of viscous flow dominated the relaxation processes, while λ^{-4} behavior characteristic of surface diffusion was only observed at large wavenumbers. With increasing fluence, the range dominated by λ^{-4} spread to lower frequencies, implying that curvature driven surface diffusion processes became more important. For the 3 MeV Au^+-irradiated samples (Figure 6.10b), λ^{-4} behavior dominated relaxation processes in the sample irradiated to 5 $\times 10^{13}$ ions/cm^2. With an increase of fluence to 1 $\times 10^{14}$ ions/cm^2, λ^{-4}

behavior dominated at low and high wavenumbers, while at intermediate wavenumbers, stochastic roughening processes dominated; samples irradiated to 2 ×10^{14} ions/cm^2 showed the same fundamental behavior. These increases in surface diffusion at higher ion fluence may help explain the size broadening effects seen in the samples shown in Figure 6.4d-6.4f, while stochastic roughening effects may be tied to sputtering behavior.

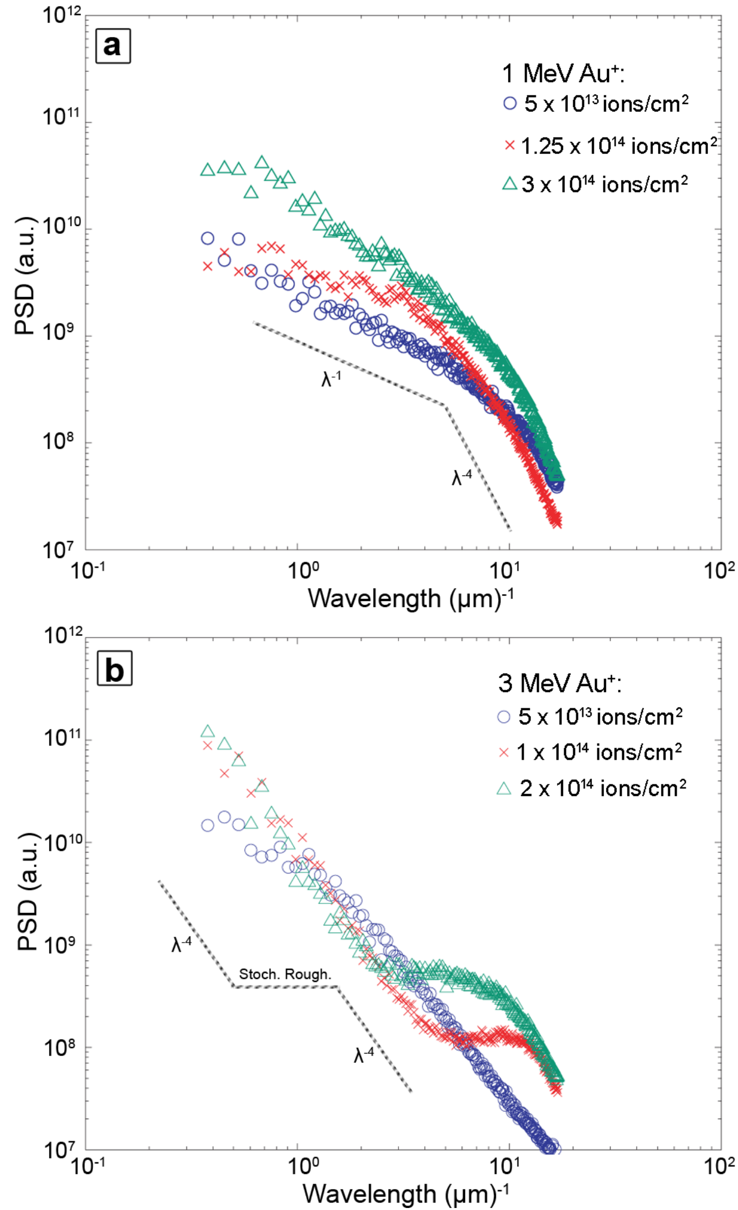

Figure 6.10. Log-log plot of power spectral densities (PSD) for irradiated InSb with a) 1 MeV Au^+ and b) 3 MeV Au^+ calculated from the images shown in Figure 6.4. λ^{-1}, λ^{-4}, and stochastic roughening trend lines are included.

6.2 FIB Irradiation of InSb

6.2.1 Nanocone Formation

Figure 6.11 shows the evolution of the InSb surface during irradiation with 30 keV Ga^+ ions. Although the surface initially develops a pockmarked appearance similar to that seen in irradiated GaSb or Ge (Figure 6.11a), continued irradiation results in the formation of semi-ordered nanocones on the material surface rather than the formation of nanofibers or nanoporous structures (Figure 6.11d).

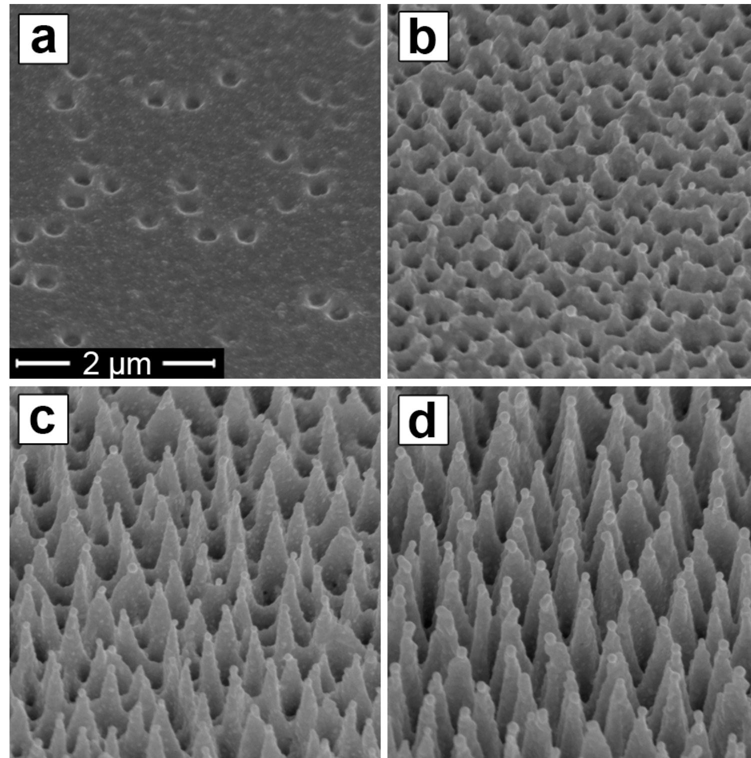

Figure 6.11. SEM images of InSb irradiated with 30 keV Ga^+ ions at normal incidence to fluences of a) 6.25×10^{15} ions/cm^2, b) 2.5×10^{16} ions/cm^2, c) 9.375×10^{16} ions/cm^2, and d) 1.875×10^{17} ions/cm^2. Images are shown at 45° from normal.

Many ion-induced surface structures can be explained through the BH model, which stipulates that when an ion beam is normally incident on a sample, surface topology differences result in preferential sputtering of low topography regions over high

regions, resulting in an instability that leads to the formation of periodic hillocks and depressions.[19] As the BH model is dependent upon sputtering, its effects are most prevalent under low ion energy irradiation conditions where sputtering is dominant. The periodic cone-shaped structures present on the irradiated InSb surface seem to represent surface sputtering effects as described by the BH model, although recent work suggests that the specific cone-shaped structures created are a result of combined sputtering and phase separation effects in III-V semiconductors.[20]

Bibliography

1. H. Weiss and H. Welker, Zur Transversalen Magnetischen Widerstandsänderung von InSb. *Z. Phys.* **138**, 322 (1954).

2. A. Rogalski, Infrared Detectors: Status and Trends. *Prog. Quantum Electron.* **27**, 59 (2003).

3. D. Kleitman and H. J. Yearian, Radiation-induced Expansion of Semiconductors. *Phys. Rev.* **108**, 901 (1957).

4. G. L. Destefanis and J. P. Gailliard, Very Efficient Void Formation in Ion Implanted InSb. *Appl. Phys. Lett.* **36**, 40 (1980).

5. S. M. Kluth, D. Llewellyn, and M. C. Ridgway, Irradiation Fluence Dependent Microstructural Evolution of Porous InSb. *Nucl. Instrum. Methods Phys. Res. B* **242**, 640 (2006).

6. N. Nitta, M. Taniwaki, Y. Hayashi, and T. Yoshiie, Formation of Cellular Defect Structure on GaSb Ion-implanted at Low Temperature. *J. Appl. Phys*. **92**, 1799 (2002).

7. E. Snoeks, A. Polman, and C. A. Volkert, Densification, Anisotropic Deformation, and Plastic Flow of SiO_2 During MeV Heavy Ion Irradiation. *Appl. Phys. Lett.* **65**, 2487 (1994).

8. A. Gutzmann, S. Klaumünzer, and P. Meier, Ion-beam-induced Surface Instability of Glassy $Fe_{40}Ni_{40}B_{20}$. *Phys. Rev. Lett.* **74**, 2256 (1995).

9. H. Trinkaus and A. I. Ryazanov, Viscoelastic Model for the Plastic Flow of Amorphous Solids Under Energetic Ion Bombardment. *Phys. Rev. Lett.* **74**, 5072 (1995).

10. A. Gutzmann and S. Klaumünzer, Shape Instability of Amorphous Materials During High-energy Ion Bombardment. *Nucl. Instrum. Methods Phys. Res. B* **127/128**, 12 (1997).

11. G. L. Destefanis, J. P. Belle, J. M. Ogier-Collin, and J. P. Gailliard, Molecular Effect in the Expansion of Ion Implanted InSb. *Nucl. Instrum. Methods* **182/183**, 637 (1981).

12. N. Matuda, S. Baba, and A. Kinbara, Internal Stress, Young's Modulus, and Adhesion Energy of Carbon Films on Glass Substrates. *Thin Solid Films* **81**, 301 (1981).

13. S. B. Iyer, K. S. Harshavardhan, and V. Kumar, Buckling Patterns in Diamond-like Carbon Thin Films. *Thin Solid Films* **256**, 94 (1995).

14. Z. Huang, W. Hong, and Z. Suo, Evolution of Wrinkles in Hard Films on Soft Substrates. *Phys. Rev. E* **70**, 030601 (2004).

15. Z. Huang, W. Hong, and Z. Suo, Nonlinear Analyses of Wrinkles in a Film Bonded to a Compliant Substrate. *J. Mech. Phys. Solids* **53**, 2101 (2005).

16. S. G. Mayr and K. Samwer, Model for Intrinsic Stress Formation in Amorphous Thin Films. *Phys. Rev. Lett.* **87**, 036105 (2001).

17. S. G. Mayr, K. Samwer, and R. S. Averback, Surface Kinetics During Growth and Ion Irradiation of Glassy Metal Films. *Scripta Mater.* **49**, 961 (2003).

18. W. M. Tong and R. S. Williams, Kinetics of Surface Growth: Phenomenology, Scaling, and Mechanisms of Smoothening and Roughening. *Annu. Rev. Phys. Chem.* **45**, 401 (1994).

19. R. M. Bradley and J. M. E. Harper, Theory of Ripple Topography Induced by Ion Bombardment. *J. Vac. Sci. Technol. A* **6**, 2390 (1988).

20. S. Le Roy, E. Barthel, N. Brun, A. Lelarge, and E. Søndergard, Self-sustained Etch Masking: A General Concept to Initiate the Formation of Nanopatterns During Ion Erosion, *J. Appl. Phys.* **106**, 094308 (2009).

Chapter 7

Ion Irradiation of Si

Silicon is an extremely abundant element that is the primary component of semiconductor devices, most notably integrated circuits or ICs, although by far the majority of refined silicon is used in smelting, aluminum manufacturing, and the production of chemicals and silicone products.[1] Since advances in silicon refining technology have made high purity silicon readily available, silicon has become the most widely used semiconductor due to its stability at high temperature and the high quality dielectric that forms from its native oxide. Consequently, silicon has become the most thoroughly studied semiconductor of the past several decades, making it all the more surprising that experimental evidence of ion irradiation-induced porous silicon has been so elusive. In this chapter, the effects of ion irradiation in Si are studied in high and low ion energy regimes.

7.1 High Energy Ion Irradiation

7.1.1 Porous Silicon from High Dose Irradiation

Irradiation of Si under similar irradiation conditions to those which produce porous Ge, GaSb, or InSb results in no observable changes to the sample microstructure. For example, Si samples irradiated at room temperature with 1 MeV Au^+ to a fluence of 1×10^{15} ions/cm^2 (11.0 dpa) resulted in flat, featureless surfaces that showed no observable

porosity in XSEM or XTEM images. However, in an experiment designed to produce a higher level of atomic damage than previous experiments, where Si was implanted with 9 MeV Au^{3+} ions (predicted ion range of 2.06 μm) to a fluence of 7.8×10^{16} ions/cm^2 (1016 dpa), limited porosity was visible after XTEM examination. Figure 7.1 shows a composite XTEM image of the irradiated region. Small voids (light regions) of about 20 to 80 nm in diameter are randomly distributed along the first 2.8 μm of the sample thickness, at which point there is a large distribution of Au precipitates (dark regions) of varying sizes; precipitate composition was confirmed by EDS analysis. Some larger voids are also present at the surface interface. In addition, SAED of the porous region showed that the material is still fully crystalline following ion irradiation. While BF TEM imaging was able to reveal distinct void clusters (Figure 7.1, Insert), the material as a whole does not contain the same level of porosity as that seen in other ion irradiated semiconductors.

The results of the EMSL Au^{+} and Au^{3+} implantations in Si indicated that porous structures may only form in Si at higher damage levels, due to implantation with high energy ions to high doses, or perhaps under high sample surface temperature conditions. To test both of these assumptions, tests were performed at MIBL using 280 keV Si^{+} ions (predicted ion range of 377 nm) implanted to very high fluence into Si. Although the MIBL implanter is capable of accelerating voltages of up to 400 kV, a voltage of 280 kV was used because it was at this voltage that the maximum possible beam current was obtainable with the Si source. Instead of scanning the beam, the beam was focused to a point about 3 mm in diameter on the Si target, allowing us to obtain a maximum possible

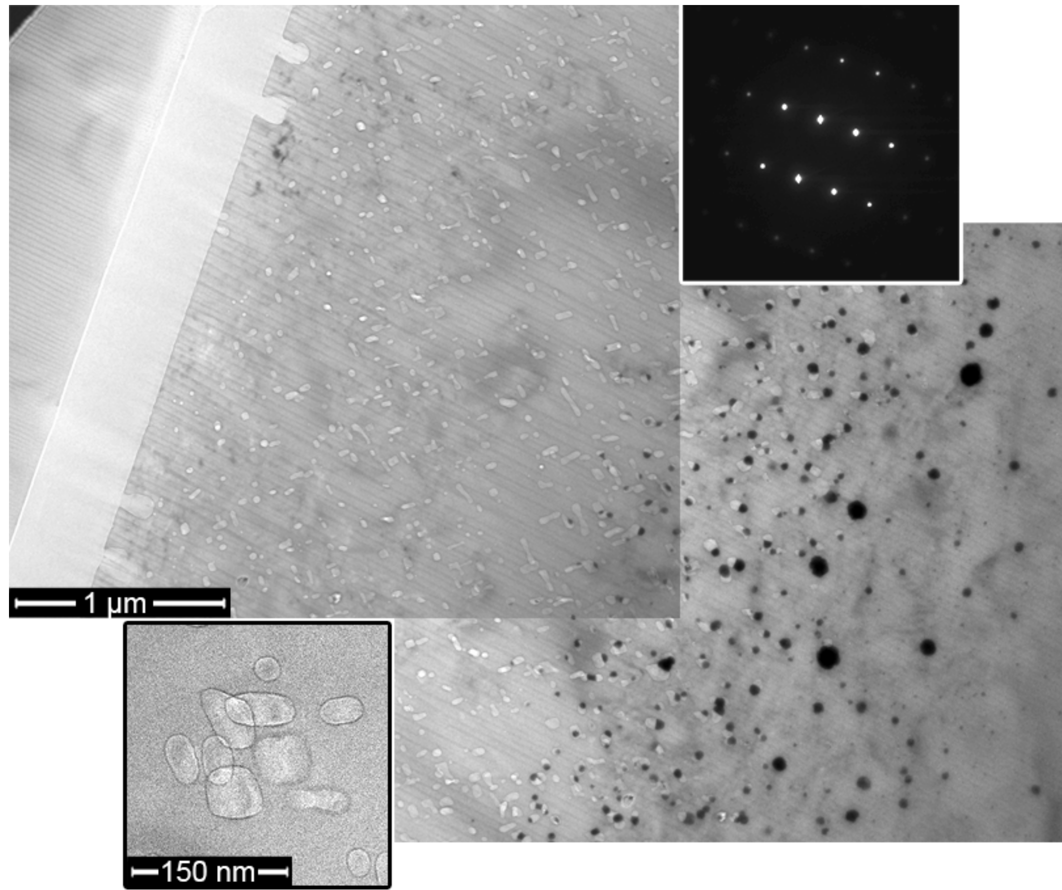

Figure 7.1. Composite XTEM image of Si irradiated with 9 MeV Au^{3+} to a fluence of 7.8 × 10^{16} ions/cm^2. Light regions represent voids, while dark regions represent Au precipitates. Insets show a SAED pattern of the surface region and a BF TEM image of a cluster of voids.

current density of about 300 μA/cm^2, thus maximizing ion flux and minimizing implantation time.

Irradiation of externally cooled samples (surface temperature of 170°C) with 280 keV Si^+ to ~ 8 × 10^{18} ions/cm^2 (~12800 dpa) was only marginally effective at formation of irradiation-induced porosity. Although the surface appeared slightly textured in plan-view SEM images, XSEM revealed only sporadic populations of pores 15 to 115 nm in diameter. However, Si samples irradiated at room temperature (surface temperature of ~450°C) showed clear evidence of void formation. Figure 7.2 shows plan view and

XSEM images of Si implanted to ~ 6 - 8 × 10^{18} ions/cm^2 (~9600 - 12800 dpa) at a surface temperature of 450°C. In the top-down image (Figure 7.2a), some pores can be seen to have intersected the surface, while other areas appear to show small breaks in the surface layer, similar to the craze-like openings visible in ion-irradiated GaSb (see Figure 3.4a). Although the majority of the surface in Figure 7.2a is flat, the secondary electron image appears wrinkled due to the effects of backscattered electrons, which are not scattered by void space. Figure 7.2b shows an XSEM image of the irradiated region, giving confirmation that the sample contains a porous layer beneath the continuous surface. Pores of 15 to 115 nm in diameter densely populate a well-defined band centered roughly 400 nm from the sample surface. The location of the pores matches up very well with TRIM predictions, which estimate the peak production of vacancies to occur at about 325 nm below the Si surface. More data on pore sizes is available in Appendix 1.

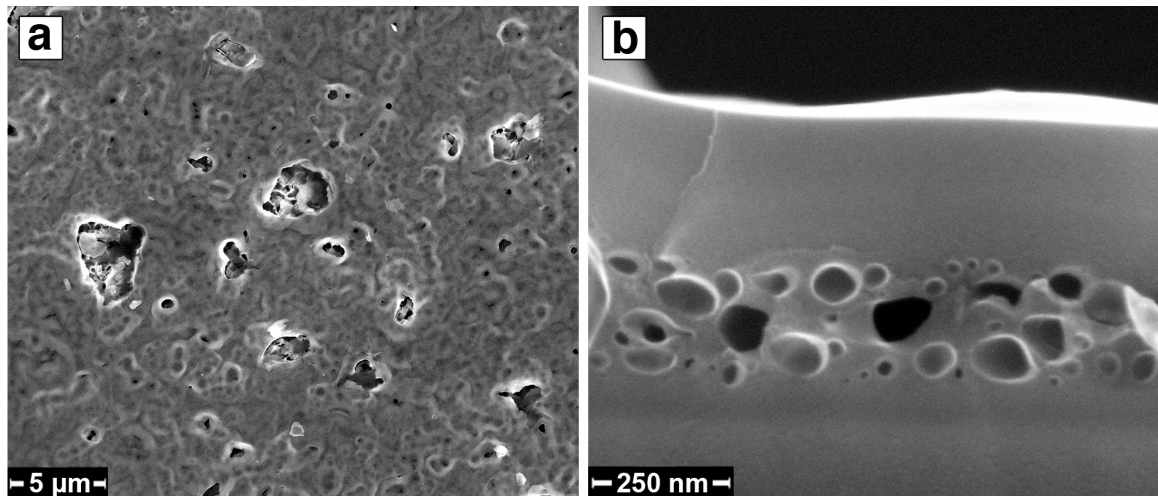

Figure 7.2. Si implanted with 280 keV Si^+ to ~ 6 - 8 × 10^{18} ions/cm^2 at a surface temperature of ~450°C. a) Plan view SEM imaging shows some sections where pores have broken free and are exposed to the surface, while the majority of the surface exhibits electron backscattering contrast. b) XSEM image showing pores tightly constrained beneath the surface.

In addition, XSEM imaging of the irradiated samples revealed unique nano-sized cave-like structures, as seen in Figure 7.3a. Immediately above and below the nanocave structures are thin porous regions, while within the cave regions themselves, there are distinct stalagmite- and stalactite-like structures spanning the height of the cave. Investigation of several of the nanocaves showed that the thickness of the nonporous surface layer, i.e. the distance from the sample surface to the start of the porous region, remained fairly constant over both the nanocave and purely nanoporous regions. Careful investigation of the nanocaves gives some insight into their formation. The flat bottom of the nanocaves, as seen in Figure 7.3a, is located near the end of the vacancy production curve as predicted by TRIM calculations, indicating that the caves are formed due to vacancy coalescence and swelling in the peak vacancy deposition region directly above, which results in outward expansion of the surface layer. The stalagmite- and stalactite-like structures correspond to the fibers in GaSb and InSb or the cell walls in Ge, resulting from material between pores that has been further confined due to massive void agglomeration. Visual evidence of crack-free surfaces and necking in the stalagmite- and stalactite-like structures indicates that the silicon sample is deforming plastically during the expansion and swelling of the nanocaves, similar to ion irradiated GaSb (Section 4.1.2), InSb (Section 6.1.2), and other ion irradiated amorphous materials.[2,3] A key difference in the Si samples, however, is that SAED of individual stalactite and stalagmite structures shows that the structure is single-crystalline (Figure 7.3b). Given the high sample temperature during the irradiation, the irradiated region does not amorphize, as the surface is clearly above the critical amorphization temperature of ~280°C in Si.[4] The lack of amorphization of the Si substrate is a clear difference between irradiation of

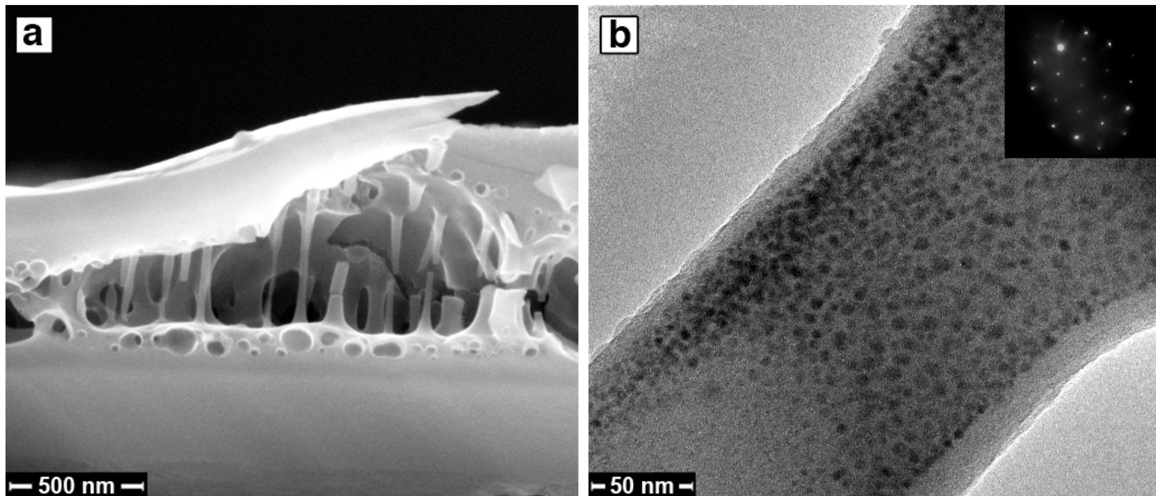

Figure 7.3. Images of Si nanocaves and related structures. a) XSEM image of a silicon nanocave formed by 280 keV Si^+ implantation to a fluence of ~ 8 × 10^{18} ions/cm^2 at 450°C. b) BF TEM image of an irradiation-induced Si stalactite, with corresponding SAED pattern (insert).

Si and the trio of Ge, GaSb, and InSb and could be a notable factor in the difference in irradiation conditions necessary for formation of porous structures in the four materials.

Irradiation of externally heated samples (surface temperature of 650°C) with 280 keV Si^+ to ~ 2 - 8 × 10^{18} ions/cm^2 resulted in the most obviously porous samples, with the highest level of porosity of the tested conditions. In these samples irradiated at higher temperature, porosity was more well developed even at lower fluences; samples irradiated to 2 × 10^{18} ions/cm^2 (3200 dpa) already exhibited significant subsurface porosity. Samples irradiated to higher fluences of 4 and 8 × 10^{18} ions/cm^2 (~6400 and 12800 dpa) resulted in higher overall void space and porous layers that had expanded fully to the surface, as shown in Figure 7.4. After high fluence irradiation to 8 × 10^{18} ions/cm^2, the Si surface began to evolve into a more intertwined, web-like structure similar to that seen in high fluence-irradiated GaSb and Ge (see Figures 4.4f and 5.4h). TEM SAED also confirms the samples' crystallinity.

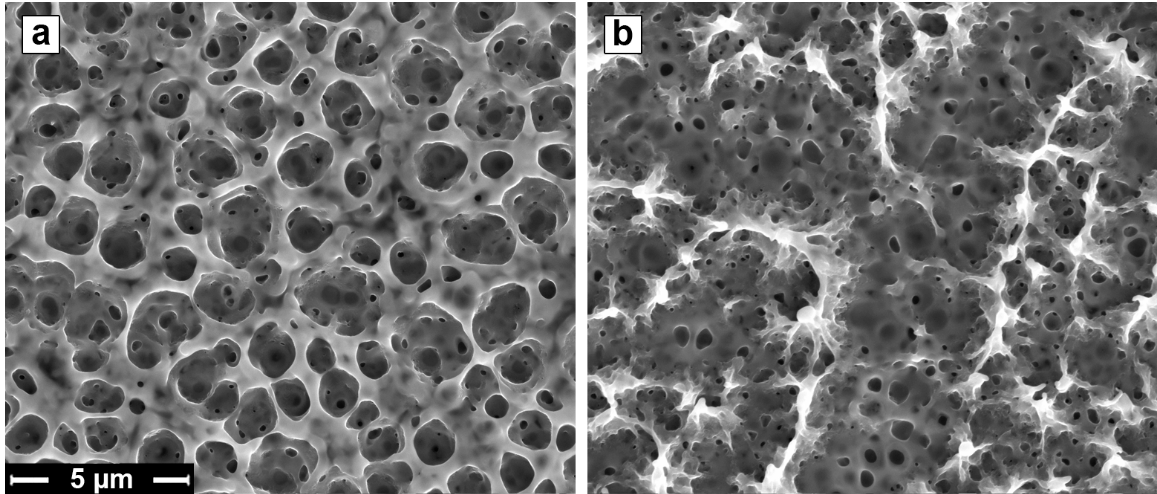

Figure 7.4. Plan view SEM images of Si implanted with 280 keV Si^+ to a) 4×10^{18} and b) 8×10^{18} ions/cm^2 with a surface temperature of ~650°C.

7.1.2 Effects of Sputter Shields on Formation of Porous Structures

High temperature (surface at about 650°C) implantations were performed on Si wafers with 36 nm thick SiO_2 and Si_3N_4 surface layers. Though 280 kV was the highest reasonable accelerating voltage for us to conduct our high dose implantations, 280 keV ions still cause a substantial amount of surface sputtering, hence the observed need to coat easily sputtered Si with much harder to sputter SiO_2 and Si_3N_4.

Overall, the presence of a sputter shield over the Si samples did not make a significant difference in terms of the resulting porous structure, although the irradiated samples did retain a distinct surface layer to higher fluences. Figure 7.5 shows plan view and XSEM images of Si with a 36 nm thick SiO_2 surface layer irradiated to ~ 8×10^{18} ions/cm^2. The plan view image shows that a majority of the surface still retains a flat surface, though backscattered electron contrast helps illustrate the porosity immediately underneath the surface. XSEM shows the presence of large pores, but none of the web-like structures seen in pure Si are yet visible, indicating that these surface degradation

effects may be due to sputtering mechanisms. SAED of the irradiated surface indicated that the porous region is fully amorphized, although the SiO_2 surface layer was amorphous prior to irradiation. Samples with Si_3N_4 surface layers exhibited very similar characteristics to those seen with SiO_2, namely surface layer stability at higher fluences, better pore definition at these same doses, and amorphous porous surface layers.

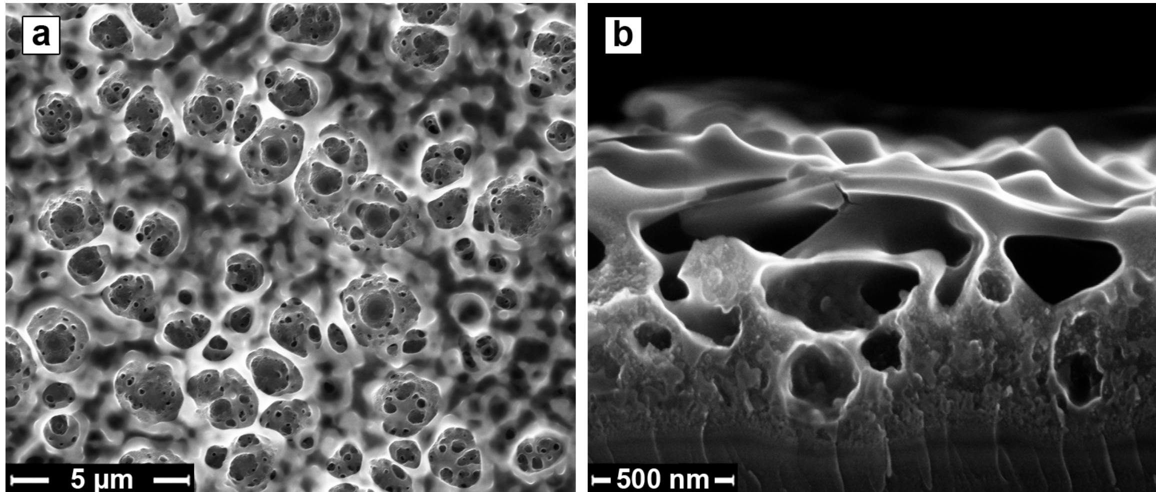

Figure 7.5. a) Plan view and b) XSEM images of Si with a 36 nm SiO_2 surface layer irradiated with 280 keV Si^+ to ~ 8×10^{18} ions/cm^2 at a surface temperature of ~650°C. Although the sputter shield resulted in the presence of a surface layer at higher ion dose, the resulting porous microstructure remains virtually unchanged from virgin Si samples.

7.2 FIB Irradiation of Si

7.2.1 Hole Milling and Ripple Formation

Room temperature 30 keV Ga^+ irradiations performed at ion beam currents of up to 250 μA/cm^2 to doses of up to 1×10^{18} ions/cm^2 all resulted in no observable change to the Si sample morphology. Though the samples clearly showed that some sputtering had occurred from the irradiated area, the sample surface was smooth and untextured, and XSEM and XTEM revealed no evidence of embedded porosity.

Given the lack of changes in the microstructure, another experiment was performed in which the damage conditions were maximized within the FIB. Using a current density of 15000 $\mu A/cm^2$ over an irradiated area of 100 μm^2, a Si sample was observed *in situ* at a progressively higher ion fluence, to a maximum of 5×10^{19} ions/cm^2 (~15000 dpa). Initially, only sputtering effects were visible in the milling of the surface. However, by the time the maximum ion dose was reached, a hole had been dug that exhibited strongly textured walls resembling steps, as shown in Figure 7.6. Although this behavior is in stark contrast with other ion irradiated semiconductors, the formation of the steps along the side of the FIB milled hole can be explained by ripple theory as described by the BH model.[5] Essentially, as the milling process continues and the hole grows deeper, ions sputtered from the bottom of the hole become more and more likely to be redeposited on the sides of the milled hole rather than to escape into free space. Therefore, eventually in the milling process, a steady state depth will be reached whereupon increased ion fluence will not result in increased hole depth. As this steady state is reached, the walls of the hole shift from being perpendicular to the ion beam direction to being at a angle to the ion beam. This results in glancing angle ion collisions on the trench walls, which leads to ripple formation as described by ripple theory and as seen in ion eroded Si.[6-8] EDS tests show that the particulates visible on the sides of the steps are Ga droplets, as seen in Figure 7.6b and in the literature.[9] Despite the formation of the ripple structures following high fluence implantation, no porosity was observable in the immediate irradiated region.

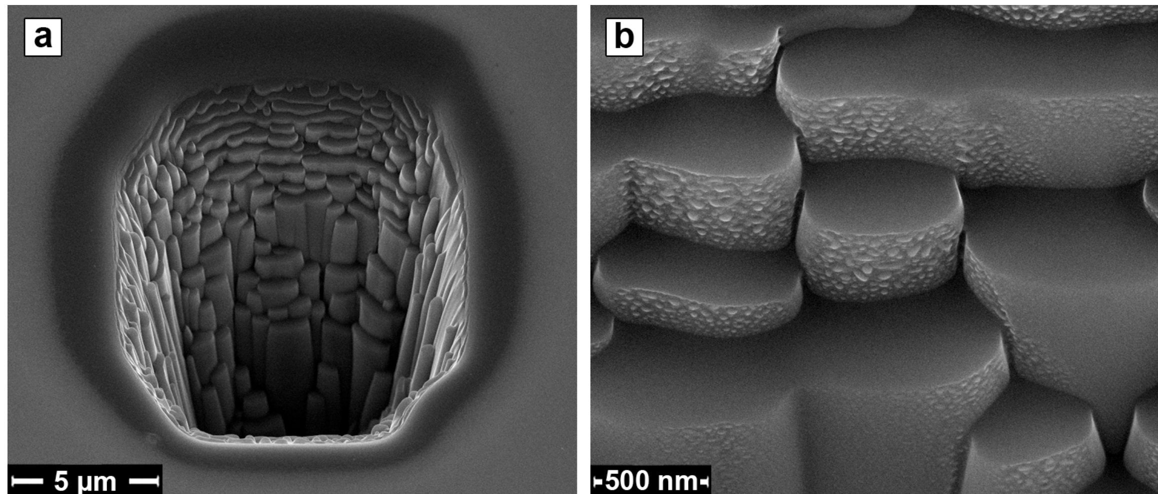

Figure 7.6. Ultra-high dose FIB milled Si. a) SEM image of a hole milled in Si following 30 keV Ga^+ irradiation to 5×10^{19} ions/cm^2. b) SEM closeup of the step/ripple morphology present on the trench walls. Both images are taken at an angle of 30° from the surface.

7.3 MEVVA Ion Irradiation

7.3.1 Surface Structure Formation and Analysis

Following MEVVA ion implantation,[10] the Si surface morphology begins to visibly evolve at a dose of about 5×10^{17} ions/cm^2. At this fluence, numerous surface pores have formed, and an increase in fluence to 1×10^{18} ions/cm^2 results in the formation of an intertwined, wall-like surface structure (Figure 7.7a,b). Cross-sectional imaging confirms that these changes in morphology purely affected the Si surface, as no additional porosity or morphological changes were visible (Figure 7.7c,d). Investigation of the irradiated samples via TEM reveals that, like Si samples implanted at higher temperature, the MEEVA-implanted samples were single crystal Si, although SAED patterns also show the presence of polycrystalline Co diffraction rings. XEDS analysis performed in the TEM reaveal an approximately 10:1 atomic ratio of Si to Co in the samples, as well as significant oxidation of the surface.

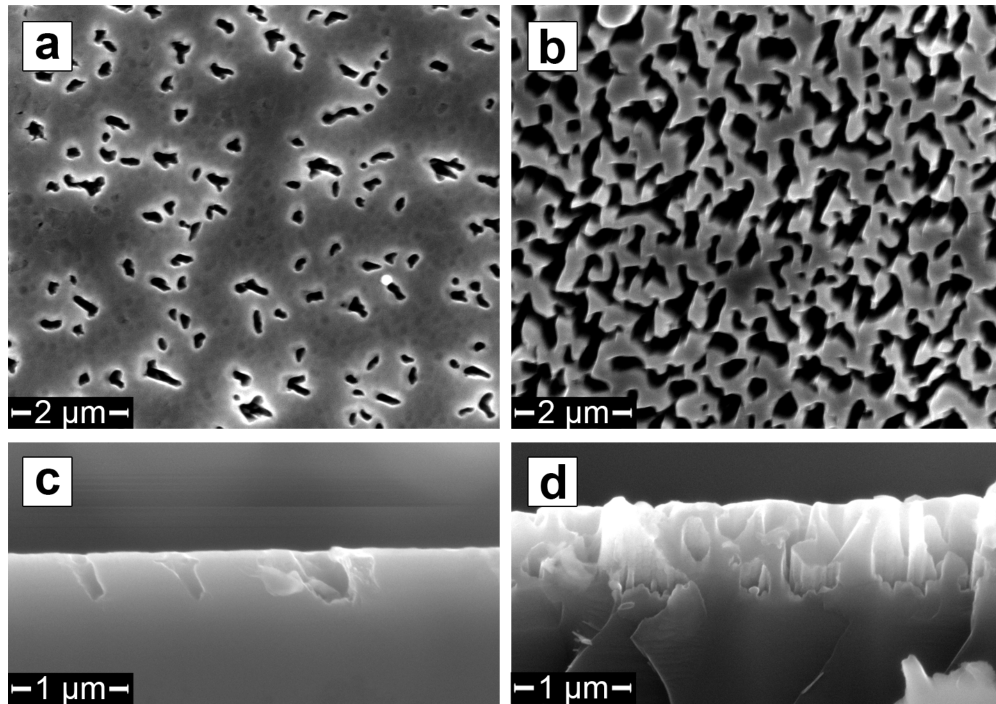

Figure 7.7. Plan view SEM images of 40 keV Co^+-irradiated (100) Si at fluences of a) 5 × 10^{17} ions/cm^2 and b) 1 × 10^{18} ions/cm^2. XSEM images are shown of the same samples in c) and d), respectively.

The dramatic differences between the samples prepared with 30 keV Ga^+ and 40 kev Co^+ are surprising given the similarities in ion energy and atomic number. Temperature could be an important difference between the two sets of experiments. While both FIB and MEVVA irradiations were performed at 50 μA/cm^2, the MEVVA broad-beam implantations would have resulted in significant heating of the sample surface (estimated at between 442 and 578°C for the various fluences),[11] which explains the presence of crystalline Si as seen in the TEM micrographs, while the FIB irradiations, which resulted from a total beam current of just 15 nA, could not cause significant heating of the sample surface. Nonetheless, while porosity was observed to increase with increased implantation temperature in the MIBL implantations, porosity was observed

even at lower sample temperatures, indicating that perhaps temperature is not a limiting factor in the formation of these structures.

Perhaps the formation of the wall-like surface morphology is actually a function of sputtering effects. While the MIBL implantations were performed with Si^+ ions, the MEVVA implantations were performed with Co^+, resulting in high concentrations of Co at the sample surface. Given the different sputtering rates of Co and Si, the new surface morphologies could be a result of preferential sputtering at the sample surface, although Co is only mildly more susceptible to sputtering than Si (2.35 Co atoms/ion compared to 2.00 Si atoms/ion in a 50/50 atomic % mixture of Si and Co).[12] Nonetheless, Fe^+ implantations performed on Si at MIBL, which showed somewhat similar surface morphologies as the Co^+ samples but also did not exhibit obvious porosity like the Si^+ implantations, give some credence to the idea that preferential sputtering may play a role in the formation of the structures.

Lastly, implantation angle may play a role in the structure formation. While the MEVVA samples were irradiated at an angle of 30°, the FIB samples were irradiated at perpendicular incidence. Although implantation angle wouldn't affect overall ability to form vacancies and pores, it has been shown that implantation angle is a crucial component in the formation of surface structures such as ripples and surface dots, as described in Section 1.1.2. Given the angular dependence of the surface holes formed via MEEVA implantation, as shown in Figure 7.7c, it seems likely that these structures are formed via some combination of angular- and sputtering-dependent mechanisms and cannot be considered to be due to bulk vacancy accumulation effects, indicating that ion

irradiation-induced porosity in Si will only form at high damage levels following implantation with high energy ions.

Bibliography

1. L. A. Corathers, Silicon. U.S. Geological Survey, Mineral Commodity Summaries (January 2009).

2. E. Snoeks, A. Polman, and C. A. Volkert, Densification, Anisotropic Deformation, and Plastic Flow of SiO_2 During MeV Heavy Ion Irradiation. *Appl. Phys. Lett.* **65**, 2487 (1994).

3. H. Trinkaus and A. I. Ryazanov, Viscoelastic Model for the Plastic Flow of Amorphous Solids Under Energetic Ion Bombardment. *Phys. Rev. Lett.* **74**, 5072 (1995).

4. F. F. Morehead, B. L. Crowder, and R. S. Title, Formation of Amorphous Silicon by Ion Bombardment as a Function of Ion, Temperature, and Dose. *J. Appl. Phys.* **43**, 1112 (1972).

5. R. M. Bradley and J. M. E. Harper, Theory of Ripple Topography Induced by Ion Bombardment. *J. Vac. Sci. Technol. A* **6**, 2390 (1988).

6. G. Carter and V. Vishnyakov, Roughening and Ripple Instabilities on Ion-bombarded Si. *Phys. Rev. B* **54**, 17647 (1996).

7. T. K. Chini, F. Okuyama, M. Tanemura, and K. Nordlund, Structural Investigation of keV Ar-ion-induced Surface Ripples in Si by Cross-sectional Transmission Electron Microscopy. *Phys. Rev. B* **67**, 205403 (2003).

8. A.-D. Brown, J. Erlebacher, W. L. Chan, and E. Chason, Transient Topographies of Ion Patterned Si(111). *Phys. Rev. Lett.* **95**, 056101 (2005).

9. J. C. Reiner, P. Nellen, and U. Sennhauser, Gallium Artefacts on FIB-milled Silicon Samples. *Microelectron. Reliab.* **44**, 1583 (2004).

10. Y. Zhang, T. Winzell, T. Zhang, I. A. Maximov, E.-L. Sarwe, M. Graczyk, L. Montelius, and H. J. Whitlow, High-fluence Co Implantation in Si, SiO_2/Si and Si_3N_4/Si Part III: Heavy-fluence Co Bombardment Induced Surface Topography Development. *Nucl. Instrum. Methods Phys. Res. B* **159**, 158 (1999).

11. Y. Zhang, T. Winzell, T. Zhang, M. Andersson, I. A. Maximov, E.-L. Sarwe, M. Graczyk, L. Montelius, and H. J. Whitlow, High-fluence Co Implantation in Si, SiO_2/Si and Si_3N_4/Si Part I: Formation of Thin Silicide Surface Films. *Nucl. Instrum. Methods Phys. Res. B* **159**, 142 (1999).

12. J. F. Ziegler, J. P. Biersack, and U. Littmark, *The Stopping and Range of Ions in Solids*. (Pergamon Press, New York, **1985)**. Also see: http://www.srim.org

Chapter 8

Analysis of Porous Network Formation and Growth

Thus far, background research on irradiation-induced nanostructures and void swelling in semiconductors has been discussed, classical void swelling mechanics and theory have been presented, and a vast array of experimental evidence of irradiation-induced bulk and surface structures has been studied in detail. While the previous chapters on GaSb, Ge, InSb, and Si have included some analysis of irradiation effects specific to each material, the focus of this chapter is on analysis of irradiation effects as a whole across all the implanted materials, and an effort will be made to analyze why the set of semiconductors that have been studied behave differently under ion irradiation both amongst themselves and compared to other material types.

8.1 Irradiation Parameter-related Effects

8.1.1 Influence of Ion Fluence

The effects of ion fluence are perhaps the easiest to quantify. Throughout all the materials studied, given a material that exhibited some porosity at a given dose, an increase in fluence led to the formation of a thicker, more porous layer. Porous layer thicknesses as a function of fluence for GaSb, InSb, and Ge irradiated with 1 MeV Au^+ ions are shown in Figure 8.1. Porous layer thicknesses were measured via XSEM; raw

data and statistical analysis of error involved in the measurement is included in Appendix 2. In all cases, the expansion of the porous layer is nearly a linear function of the implantation dose. Although Si was not included in Figure 8.1 due to a lack of porous layer formation in our experiments using 1 MeV Au^+ and a low number of data points available at any given set of constant irradiation conditions (temperature, ion energy, and flux), experimental observation of Si under ion irradiation showed that the material also became more porous at higher fluences, as discussed in Chapter 7.

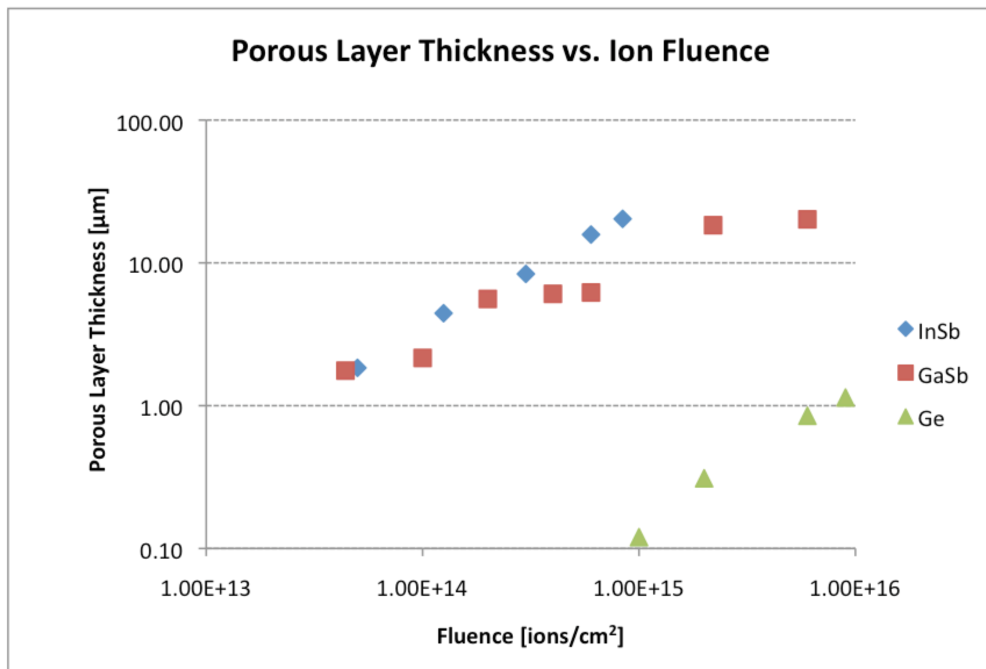

Figure 8.1. Log-log plot of porous layer thickness versus implantation ion fluence showing near linear relationships between the parameters. InSb, GaSb, and Ge were all irradiated with 1 MeV Au^+.

The linear expansion of the porous layer aligns well with the qualitative description of porous structure formation first described by Nitta *et. al.* and expanded upon in Section 4.1.1.[1] Fundamental to irradiation-induced void formation and growth is the accumulation of vacancies, which is caused by ion damage to the target material. By increasing ion fluence, one directly increases the atomic damage per unit area, resulting

in greater numbers of vacancies produced. Increasing the number of vacancies produced in a material does not necessarily result in larger vacancy concentrations in the material, as point defect recombination and vacancy diffusion to sinks rises in response to rising vacancy levels. However, increased vacancy diffusion to sinks, specifically voids, results in the formation of larger voids and a less dense, more expansive porous layer, explaining the relation seen in Figure 8.1.

Closely related to porous layer thickness is overall pore size, but defining and measuring pore size is a much more difficult task. When porosity levels are low and individual pores are visible, such as in the Si samples shown in Figure 7.2b, then pore sizes can be measured, and distributions of pore sizes can be obtained. However, ion-irradiated porous materials rarely exhibit individual pores, rather we see complex, interconnected porous networks. Once pores begin to coalesce and interact with one another, then individual pores can no longer be defined and measured, making it impossible to compare pore size and ion fluence. Measurement of the overall porosity or density of the porous layer is theoretically possible through ellipsometric porosimetry measurements, but even these techniques contain a high level of measurement error that is dependent on both material properties and pore size.[2,3] Similarly, XTEM could be used to obtain an estimate of sample porosity, but even in a TEM foil, porous and fibrous regions overlap, as exemplified in Figure 6.1a, making estimates of porosity inaccurate. Though quantitative results are difficult to obtain, visual observation of irradiated structures seems to indicate an increase in void space with increased ion fluence.

Although porosity may be difficult to measure, fiber or cell wall size is actually quite easy to obtain via SEM or TEM imaging. Figure 8.2 shows a plot of fiber

diameter/cell wall thickness versus ion fluence for GaSb, InSb, and Ge irradiated with 1 MeV Au^+. Although InSb did exhibit some reduction in fiber size at higher fluence, as shown in Figure 6.3, as a whole the materials exhibited no real statistically significant variation in wall or fiber size with increasing ion fluence. As with pore size, however, definition of terms is vitally important. Fiber or cell size can only be defined once the porous network has developed. For example, in the same Si samples in which we can measure and define pore size (Figure 7.2b), cell wall size is meaningless, as the system is still a solid matrix with individual pores. Therefore, the accurate conclusion is that in developed porous networks, ion fluence does not significantly alter fiber or cell wall size. Relationships between fiber or cell wall size, porous layer thickness, and ion fluence are also alternatively presented in Table 8.1. Data for Figure 8.2 and Table 8.1 is included in Appendix 1, which includes fiber and pore sizes of the irradiated materials, where applicable given the irradiation-induced microstructure.

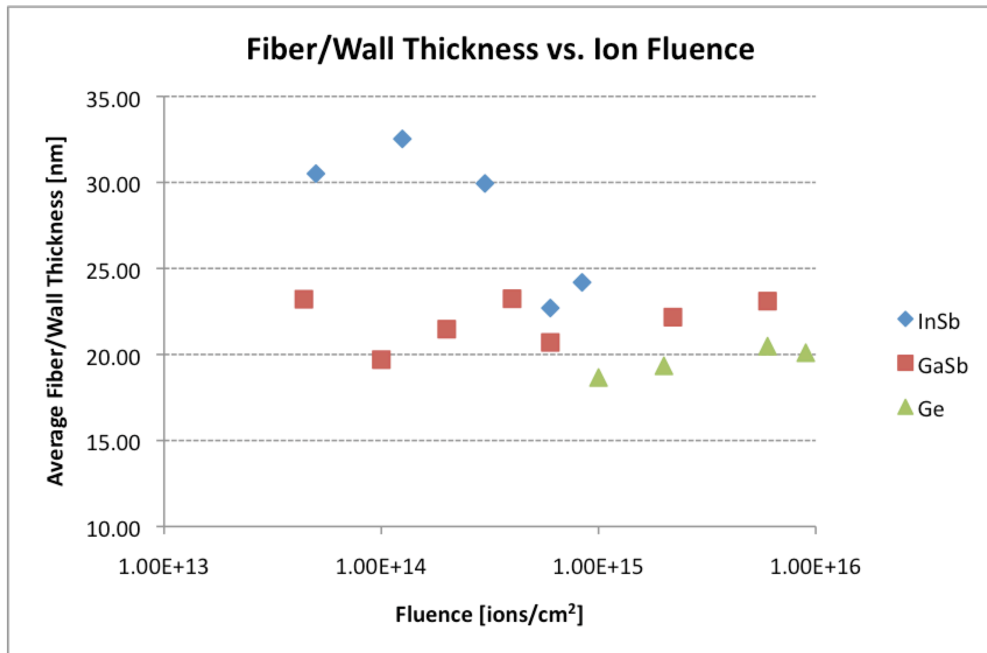

Figure 8.2. Fiber or cell wall thickness as a function of ion fluence for InSb, GaSb, and Ge irradiated with 1 MeV Au^+ ions.

Table 8.1. Porous layer thickness and fiber/cell wall thickness as a function of ion fluence in 1 MeV Au^{+}-irradiated InSb, GaSb, and Ge.

Ion Fluence [1 MeV Au^{+}/cm^{2}]	Average Porous Layer Thickness [μm]	Average Fiber/Wall Thickness [nm]
Ge		
1.00E+15	0.12	18.66
2.00E+15	0.31	19.34
6.00E+15	0.85	20.48
9.00E+15	1.14	20.10
GaSb		
4.4E+13	1.76	23.21
1.00E+14	2.16	19.70
2.00E+14	5.59	21.47
4.00E+14	6.07	23.24
6.00E+14	6.20	20.70
2.20E+15	18.36	22.17
6.00E+15	20.18	23.10
InSb		
5.00E+13	1.84	30.51
1.25E+14	4.44	32.53
3.00E+14	8.37	29.94
6.00E+14	15.79	22.70
8.40E+14	20.34	24.19

Also related to ion fluence are sputtering and ion species concentration. Although surface sputtering is not the primary driving force in the formation of irradiation-induced porous networks, as seen in the formation of deeply embedded porous networks in Ge,[4] it can affect the final structure, as seen the removal of surface layers in irradiated InSb (Section 6.1.2). Additionally, preferential sputtering may play a role in the development of the nanofiber morphology in irradiated GaSb and InSb, as both materials exhibit slight preferential sputtering of either Ga or In over Sb. For example, TRIM simulations of 1 MeV Au^{+} irradiation of GaSb and InSb predicted sputtering of 5.4 Ga/ion compared to 5.1 Sb/ion in GaSb and 6.9 In/ion compared to 6.4 Sb/ion in InSb.[5] Similarly, the accumulation of implanted ions at high fluence can lead to the formation of compounds or precipitates that change the morphology of the implanted material, as seen in the high

fluence Au^+-irradiated Si samples of Section 7.1.1, but self-ion implantation can be used to avoid unwanted precipitates in the porous network.

8.1.2 Influence of Atomic Number and Ion Energy

The proton number and energy of an ion both stongly influence the interaction cross-section of an ion with a solid, and as such, each parameter affects both the total damage transferred to the target material as well as the depth of peak vacancy production. To analyze the effects of these two parameters, the TRIM software was used to generate vacancy production curves as a function of ion energy and atomic number of the incident ion.[5] Figure 8.3 shows vacancy production curves in silicon for 1 MeV H^+, B^+, and Ru^+ ions, whose atomic numbers are 1, 5, and 44. The simulations show that an increase in ion number results in a corresponding decrease in the peak vacancy production depth, with H^+, B^+, and Ru^+ vacancy production peaks at 17.25, 1.7, and 0.26 μm, respectively. Similarly, peak vacancy production went up even more dramatically, increasing from 6×10^{-4} to 0.11 to 2.3 vacancies/ion-Å in H^+, B^+, and Ru^+.

Similar changes are visible from increases in ion energy. Figure 8.4 shows vacancy production curves in silicon from 10 keV, 100 keV, 1 MeV, and 10 MeV Si^+ ions. With each order of magnitude increase in ion energy, the peak vacancy production depth increases, from less than 10 nm at 10 keV to nearly 5 μm at 10 MeV. Although the peak vacancy production per ion per Å actually drops from 10 keV to 10 MeV, the total number of vacancies produced, obtained from integration of the vacancy production curve, increases drastically with increased ion energy, from roughly 140 vacancies/ion at 10 keV to 4900 vacancies/ion at 10 MeV. TRIM simulations also show a dramatic

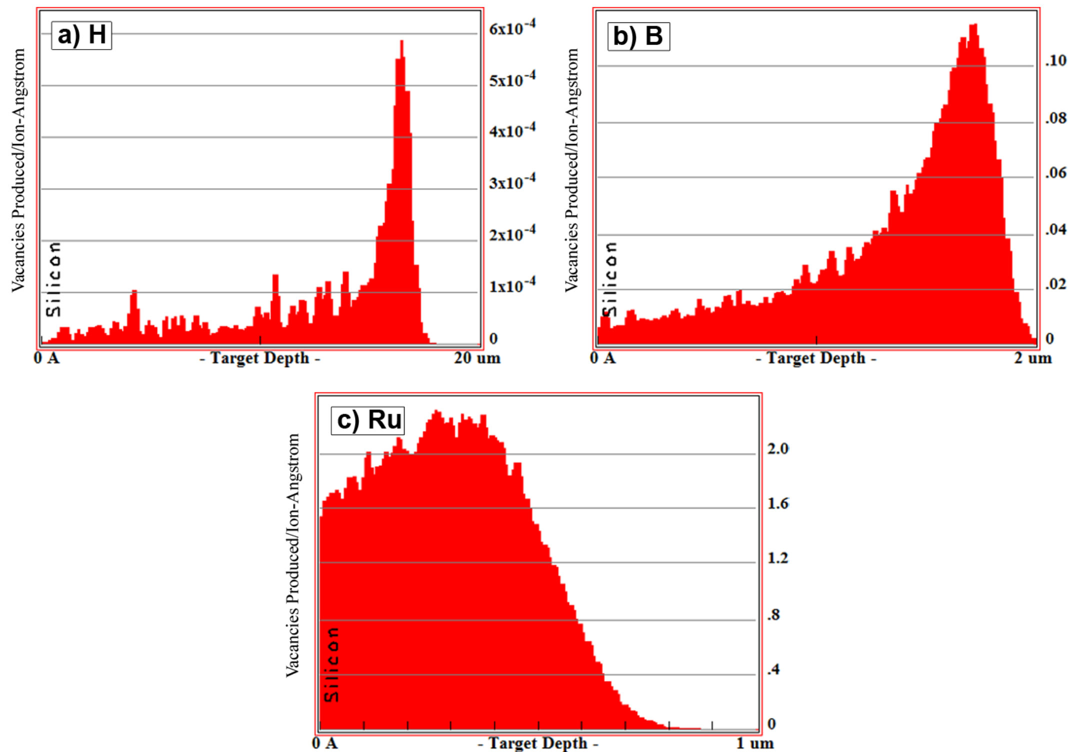

Figure 8.3. Vacancy production curves in silicon for 1 MeV a) H^+, b) B^+, and c) Ru^+ ions in terms of vacancies produced per ion per Å as a function of target sample depth. Note change in depth scale.

increase in electronic energy loss with increasing ion energy, from a peak of about 10 eV/Å at 10 keV to nearly 300 eV/Å at 10 MeV.

To summarize, increasing incident ion energy results in increased energy deposition in the sample, which results in a greater number of atomic collisions that lead to vacancy and interstitial formation, as well as greater interactions with electrons in the target. Increasing ion energy also results in a shift of the peak vacancy production region from the near surface deeper into the sample. Similarly, increasing atomic number also results in a net increase in vacancy production. While energy transfer in elastic collisions is at a maximum in collisions between particles of similar masses, vacancy production continues to increase for higher number ions due to the enlarged atomic interaction cross-section of ions with greater proton numbers. Because of their increased interaction cross-

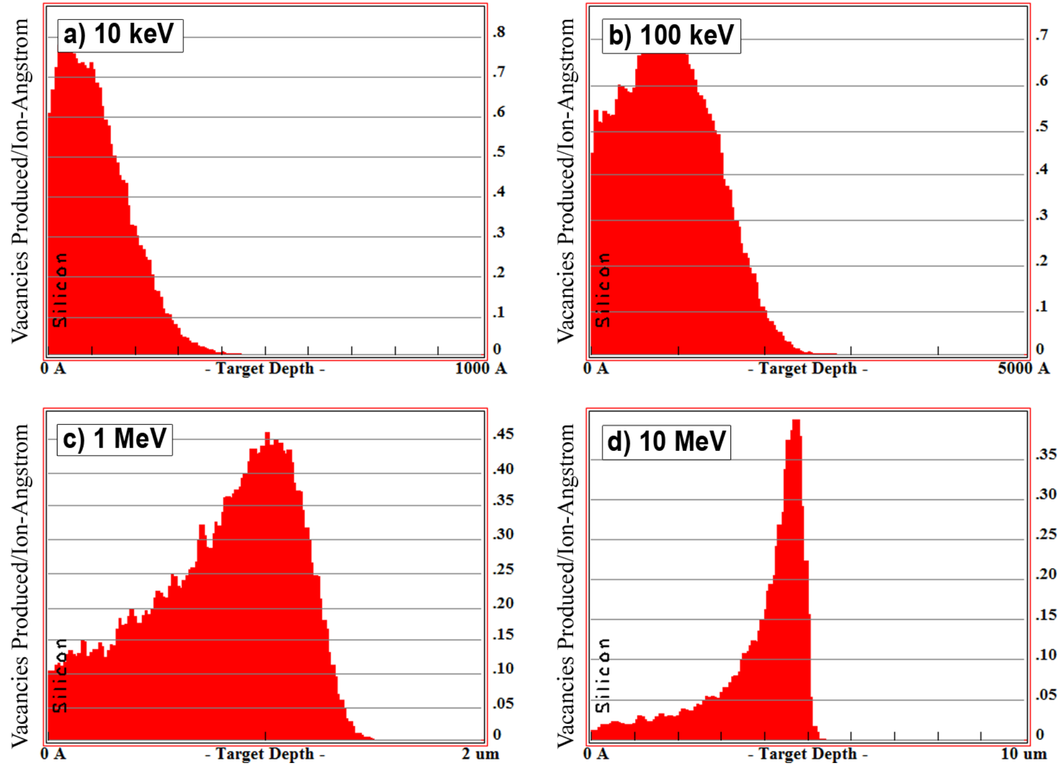

Figure 8.4. Vacancy production curves in silicon for 10 keV, 100 keV, 1 MeV, and 10 MeV Si^+ ions in terms of vacancies produced per ion per Å as a function of target sample depth. Note change in depth scale.

section, high atom number ions lose a greater percentage of their kinetic energy through atomic interactions rather than electronic interactions, leading to greater numbers of displacements. Increasing atomic number of the ion also has the effect of causing a shift of the peak vacancy production region closer to the sample surface, again due to a larger atomic interaction cross-section.

In addition to vacancy production, ion atomic number and energy also affect sputtering. Sputtering will be maximized with incident ions of low energies and high atomic numbers and minimized with ions of high energies and low atomic numbers. In general, fabrication of embedded porous layers is most efficient using high energy and

low atomic number ions at high fluence, which maximizes the depth of the peak vacancy production region while also minimizing surface sputtering.

8.1.3 Influence of Ion Flux and Implantation Temperature

Ion flux and implantation temperature are the hardest irradiation effects to quantify because the effects of the variables are dependent upon the materials properties of the target. Both ion flux and implantation temperature affect the kinetics of vacancy and interstitial production and diffusion. Figure 8.5, as presented by Olander after Weidersich's work,[6,7] shows point defect concentrations in irradiated nickel as a function of temperature and ion flux. Although the work was performed on a crystalline metal, the graphs have been modified by Olander to show the general features of the solution, such that numerical defect production rates and sink annihilation probabilities from Weidersich's work have been shown in qualitative terms. The general features of the figure should be similar for most solids and can give insight into the effects of temperature and flux in irradiated semiconductors. The plots show that vacancy concentration is high at low temperature, where diffusion coefficients are low and therefore vacancy removal processes, including recombination and diffusion to sinks, are slow. As temperature increases, recombination and annihilation processes accelerate, dropping the vacancy concentration. At higher temperatures, thermal production of vacancies dominates and, regardless of ion flux, the vacancy population approaches the equilibrium concentration. As would be expected, high ion fluxes result in higher equilibrium point defect concentrations, and high levels of defect sinks result in lower point defect concentrations.

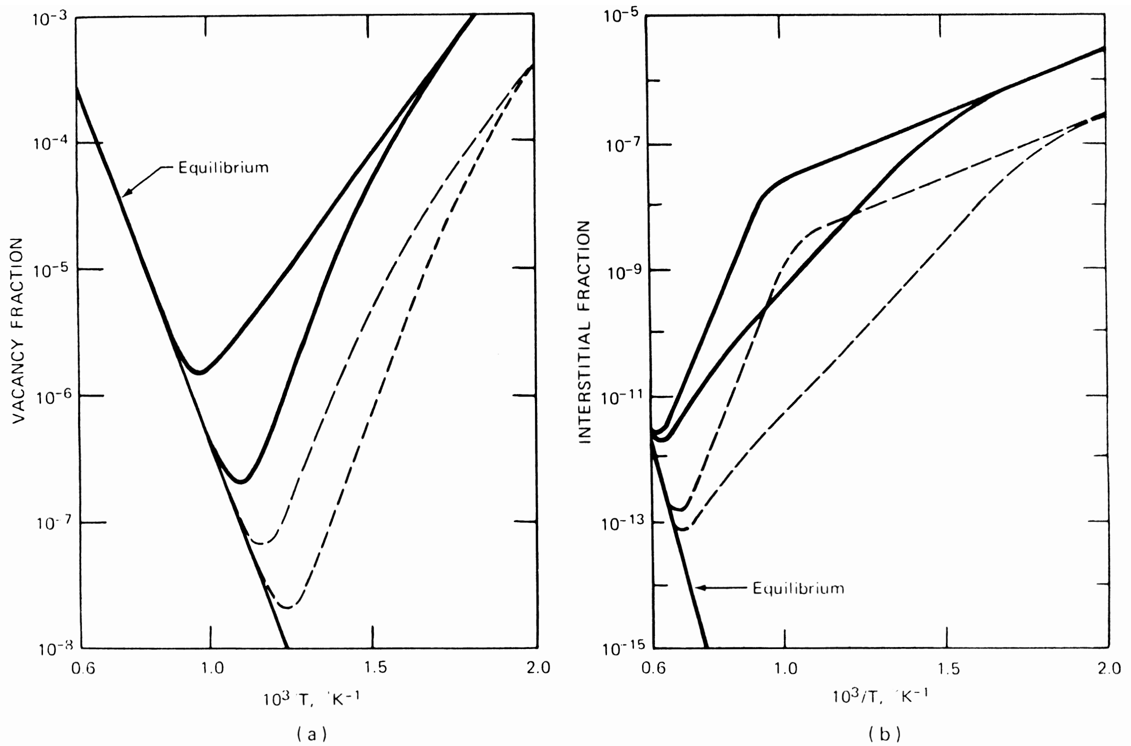

Figure 8.5. Steady-state point defect concentrations in an irradiated solid. Solid lines indicate a high ion flux and dashed lines indicate a low ion flux. Upper and lower lines represent conditions of low and high sink densities.[6]

Literature experiments on the temperature dependent formation of irradiation-induced porous InSb[8] and GaSb[9] show that porous network formation is suppressed at low and high temperatures, which matches trends seen in Figure 8.5. Since the key to formation of porous structures is not just in a high vacancy concentration but also in the ability of vacancies to agglomerate, void swelling is maximized when vacancy diffusion to sinks is maximized, which generally occurs at intermediate temperatures. At low temperatures, vacancies are immobile and cannot form voids, whereas at too high of temperatures, the substrate can accommodate a greater concentration of thermal vacancies and the irradiation-induced vacancies are better able to stay in solution. Although the impacts of temperature and flux can be generalized as shown in Figure 8.5,

the specific vacancy and interstitial concentrations in any particular material will vary with the diffusion rates of the point defects, which are temperature dependent.

8.2 Materials Parameter-related Effects

8.2.1 Melting Temperature, Bond Strength, and Displacement Energy

Since a material's melting temperature is primarily a function of bond strength, it makes sense that both parameters share the same trends when examined in conjunction with irradiated Si, Ge, GaSb, and InSb. Table 8.2 shows these four materials and lists their melting temperatures, bond dissociation energies (which are a measure of bond strength), and the minimum fluences at which porosity was observed when irradiated with 1 MeV Au^+ ions.[10] Both GaSb and InSb exhibited significant levels of porosity at the lowest tested ion fluence of 5×10^{13} ions/cm^2, and both have low melting temperatures and bond strengths. Ge possess a higher melting temperature and bond strength; it first developed porosity following irradiation to 1×10^{15} ions/cm^2. Si, meanwhile, has the strongest bonding of the tested materials and consequently was the most resistant to irradiation, first exhibiting porosity at 8×10^{16} ions/cm^2. In addition, irradiated Si samples only exhibited porosity at increased ion fluxes, indicating that both increased ion fluence and flux may be necessary for irradiation-induced porosity formation in materials with stronger atomic bonding. Table 8.2 also lists average displacement energies for each tested material, as derived in Section 3.5. As with both melting temperature and bond strength, average displacement energy decreases from Si to Ge to GaSb to InSb. Clearly, displacement energy is an important factor in the critical ion

flux and fluence levels required for porous network formation. Overall, the data shows that greater levels of porosity are formed in materials with weak interatomic bonding.

Table 8.2. Material bonding related data for Si, Ge, GaSb, and InSb.

Material	**Silicon**	**Germanium**	**GaSb**	**InSb**
Bonding Type	Covalent	Covalent	Covalent	Covalent
Bond Dissociation Energy [kJ/mol]	310	264.4	192	151.9
Bond Length (Sum of Covalent Radii) [pm]	222	244	261	271
Melting Point [K]	1687.15	1211.4	985.15	797.15
Average Displacement Energy [eV]	36	23	12.4 (Ga), 20.8 (Sb)	12.2 (In), 16 (Sb)
Minimum Fluence for Porosity [ions/cm^2]	8 x 10^{16}	1 x 10^{15}	5 x 10^{13}	5 x 10^{13}

8.2.2 Self-Diffusion Rates and Electron/Hole Mobility

Although self-interstitial and vacancy diffusion rates undoubtedly affect void formation and growth in irradiated semiconductors, it is very difficult to draw conclusions from comparison of experimental results and reported diffusion values for a number of reasons. First, diffusion data can be obtained via a number of different techniques, and different techniques can result in different data sets. Most importantly however is that different techniques are only accurate under specific temperature ranges. As a result, reported self-diffusion rates cover a broad range of temperatures,[10-15] though most tend to be reported at higher values of T/T_m, which does not correspond well with the near room temperature surface temperatures of the majority of our experiments. As a result, no definitive trends between observed changes in microstructure and diffusion rates could be made, though the relationship between the parameters is discussed in more qualitative detail in Section 8.3.3. Nonetheless, reliable electron and hole mobilities are obtainable from the literature.[10] Despite the observance of irradiation-induced porous structures only in semiconductor materials, no relationship appears to exist between

porous structure morphology and electron or hole mobility. Data sets from the literature are included in Table 8.3.

Table 8.3. Self-diffusion data and electron hole mobility data for Si, Ge, GaSb, and InSb.

	Silicon	**Germanium**	**GaSb**	**InSb**
Self Diffusion Frequency Factor, D_o [cm^2/s]	154	24.8	3200 (Ga), 34000 (Sb)	$6e^{-7}$ (In), 5.35^{e-4} (Sb)
Activation Energy for Diffusion [eV]	4.65	3.14	3.15 (Ga), 3.45 (Sb)	1.45 (In), 1.91 (Sb)
Diffusion Coefficient, D [cm^2/s]	$1e^{-11}$ - $1e^{-19}$	$1e^{-19}$ - $1e^{-22}$	$1e^{-15}$ - $1e^{-17}$ (Ga), $1e^{-18}$ (Sb)	-
Energy Gap at RT [eV]	1.12	0.67	0.67	0.163
Electron Mobility [cm^2/Vs]	1900	3800	4000	78000
Hole Mobility [cm^2/Vs]	500	1820	1400	750

8.3 Porous Network Formation Mechanics in Semiconductors

Thus far in this chapter, the effects of varying irradiation and materials parameters on irradiation-induced porous network formation have been discussed, but a fundamental question remains: what is unique about irradiated semiconductors that allows them to form porous structures during ion irradiation? In this section, possible formation mechanics for these porous networks will be discussed, with a focus on mechanics and effects specific to the studied materials.

8.3.1 Displacement Cascades and Material Amorphization

Traditional ion-solid displacement interactions are described in terms of Frenkel pairs, which can be created either by the incident ion, the primary knock-on atom (PKA), or by additional recoil atoms in the lattice. The sum of all collision events and displacements from a single PKA is commonly referred to as a collision cascade or displacement cascade. High defect densities are associated with high energy ions, especially near the end of range of the incident ion, where the ion's velocity is

sufficiently slow such that nearly every atomic interaction results in a displacement event. These high displacement density regions often result in the formation of a depleted zone, a region consisting of a vacancy rich core surrounded by increased interstitial density in the surrounding material lattice, but the size and stability of these regions are usually mitigated by Frenkel pair recombination.[16,17]

Also closely related to the concept of the collision cascade and the depleted zone is the thermal spike, which refers to the local increase in temperature of the region in which an incoming ion deposits the majority of its energy. For ions of higher energies and high atomic numbers, thermal spikes can easily increase local temperatures past the melting point, resulting in localized melting and disorder of small pockets within the target material. In elemental metal systems, the thermal spike does not result in amorphization, as the close-packed FCC, BCC, and HCP crystal structures, with packing factors of 0.74, 0.68, and 0.74, respectively, strongly favor regeneration into the perfect crystal structure. However, a key feature of Si, Ge, GaSb, and InSb is that they all have either the diamond cubic or zinc blende crystal structure, which has a packing factor of just 0.34, and all the materials are also covalently bonded. The relatively open nature of the diamond and zinc blende crystal structures allows them to incorporate numerous defects within their crystal structure, and the nature of their covalent bonding allows for formation of different bonds than in the original crystal structure following melting.[18] For example, nontetrahedral covalent bonds readily form in amorphous silicon over tetrahedral bonds present in crystalline silicon.[19] The combination of packing factor and covalent bonding makes defect annealing much slower in Si and other similar semiconductors than in metals. Molecular dynamics (MD) studies by Nordlund *et. al.*,

shown in Figure 8.6, show the difference in irradiation of Si and Ge versus the metals Al and Au.[20] While all four materials experience significant localized melting during the thermal spike, only Si and Ge retain significant atomic damage and disorder following irradiation.

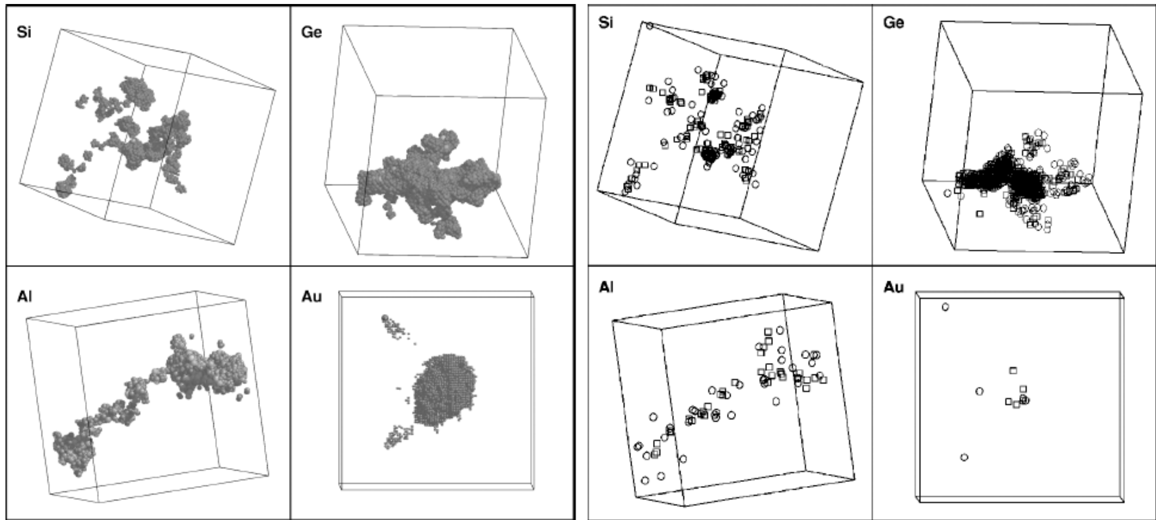

Figure 8.6. Molten zones in Si, Ge, Al, and Au caused by 10 keV lattice recoils (at left) and final defects created by the recoils (at right). Squares represent vacancies and circles interstitials. Amorphous zones appear as collections of vacancies and interstitials.[20]

Although crystal structure and bond type greatly influence the response of a material to ion irradiation, melting temperature also affects the damage region. Since the amount of damage resulting from a thermal spike depends on the size of the liquid region, materials with lower melting temperatures will experience greater damage than those with high melting temperatures. This explains the size of the amorphous regions for Si (T_m = 1687 K) and Ge (T_m = 1211 K) in Figure 8.6. Melting temperature arguments also support our experimental evidence showing the greatest amount of porous network growth in GaSb (T_m = 985 K) and InSb (T_m = 797 K), even under conditions of low ion fluence. The dependence of the size of the disordered zone on melting temperature also helps explain why void formation is more pronounced in silicon irradiations performed at

higher temperature. Due to the higher melting temperature of Si, a greater amount of energy is required to cause localized melting and disorder in the thermal spike region. By increasing the ambient temperature of the Si target, a lower amount of energy is necessary to be deposited in the thermal spike to cause amorphization, meaning that the probability of vacancy and interstitial cluster generation is increased, leading to greater void formation. In silicon, higher temperatures are also necessary for increased vacancy mobility, which allows significant diffusion of vacancies to voids and other defect sinks. However, increasing the ambient temperature of the irradiated Si samples also had the effect of raising the sample temperature above the critical amorphization temperature of Si, resulting in a lack of sample amorphization in porous Si samples irradiated at elevated temperature. The stable crystal structure of Si under irradiation at high temperature almost certainly plays a role in the extreme flux and fluence conditions required for production of irradiation-induced porous Si as compared to porous network formation in the other semiconductors. The reasons for this are discussed in the following section.

8.3.2 Vacancy Accumulation and Void Growth

The treatment of radiation damage in an amorphous material is fundamentally different that that of a crystalline material, as discussed in Section 1.3. While vacancies and interstitials are defined as missing and supplementary atoms in a crystal lattice, respectively, amorphous materials lack order, making the definitions of vacancies and interstitials incongruous. Instead, vacancies must be defined as atoms removed from an amorphous volume or as a decrease in amorphous region density, while interstitials can be defined as atoms instantaneously added to an amorphous region or as an increase in

amorphous region density. In 1985, Chaki and Li first performed molecular dynamics simulations in which they modeled self-interstitial and vacancy interactions in amorphous distributions of atoms represented by Voronoi polyhedra. Self-interstitial atoms were modeled by adding atoms to the simulation volume, and vacancies were modeled by removing atoms from the same volume. Results showed that while interstitials rapidly disappeared into the amorphous material by making small adjustments with neighboring atoms, vacancies took much longer to disappear, and simulations performed at lower temperature showed that vacancies would take even longer to disappear, helping to explain swelling in amorphous semiconductors.[21]

Although Chaki and Li's work helped explain the irradiation-induced vacancy excess in semiconductors, it did not explain the subsequent void growth and porous network formation seen in irradiated semiconductors. Void formation can, to some extent, be explained by the nature of high-energy irradiation. While traditional point defect theory assumes that Frenkel pairs are produced continuously and uniformly under ion irradiation, research has shown that defects produced in displacement cascades are highly segregated. This spatial segregation can remain after the end of the thermal spike, during which vacancies in the depleted zone coalesce while interstitials cluster in regions surrounding the cascade center.[22] The nature of collision cascades have been confirmed by MD simulations, as shown in Figure 8.6. In Nordlund *et. al.*'s simulations of damage from 10 keV recoil atoms in crystalline Si and Ge, roughly 10-15% of all defects were isolated interstitials, while less than 1% of the vacancies were isolated, a notable difference from irradiated metal samples. The remainder of the defects remained in the region of the collision cascade, resulting in a net balance of vacancies in the cascade core.

The reasons for such vacancy clustering were ascribed to the large volume of the molten zone caused by the energetic recoil, which allowed for nearly all damage being contained within the subsequent amorphous region while only very few energetic recoils were able to escape the molten region.[20] These vacancy rich cascade cores most likely serve as initial sites for void generation.

While irradiation-induced void growth in crystalline metals occurs primarily due to preferential absorption of interstitials at dislocations, leading to vacancy super-saturation, void formation, and swelling, void growth in amorphous materials is enabled by preferential absorption of interstitials within the amorphous matrix, which similarly leads to vacancy supersaturation, void growth, and swelling. This ability of the amorphous matrix to act as a sink for interstitials has been studied by Chaki and Li and more recently by Mayr and Averback, who performed MD simulations where Frenkel pairs were inserted into an amorphous Ge simulation cell.[23] In general, simulations showed that interstitials were absorbed rapidly into the amorphous matrix since they reduced covalent bonding energy, whereas vacancies did not reduce covalent bonding and thus remained localized. The delocalization of the point defects resulted in reduced recombination and enhanced vacancy agglomeration. Both Chaki and Li's and Mayr and Averback's simulations help explain why porous network formation occurs to such a high degree in materials that are amorphized by ion irradiation, such as Ge, GaSb, and InSb.

It should also be noted that while the majority of point defects in irradiated materials are created by atomic collisions, electronic interactions can also lead to the formation of vacancies in amorphous semiconductors. Fundamental work on the nature of amorphous semiconductors has shown that these materials can be characterized by

localized electron states, and recent work has shown that electron-phonon coupling in localized electron states is anomalously large.[24-26] There is growing evidence that in materials that exhibit high electron-phonon coupling, the temperature increase due to electronic interactions from high energy incident ions can adequately be described as a thermal spike, which can result in point defect production.[27,28] This explains experimental evidence of porous network formation in SHI-irradiated amorphous Ge,[29] but it also shows that vacancy production rates may be even higher in amorphous semiconductors than predicted by computer programs such as TRIM.

8.3.3 Stabilization of Nanostructure

As shown in Figure 8.2, most ion irradiation-induced porous networks seem to reach a saturation point at a certain ion fluence whereupon further irradiation does not result in significant changes to the fiber or cell wall size. Although this is by far the least studied aspect of the evolution of irradiation-induced porous networks, there is some consensus that the final structure wall size is a function of interstitial and vacancy diffusion rates in the material.[9,23] Obviously, as porosity increases in the target material, further production of point defects must take place in the cell walls. Interstitial production should proceed as normal, with interstitials being absorbed in the cell walls, causing atomic level relaxation of the material. At a certain cell wall thickness, however, vacancies produced in the cell wall will migrate to existing voids before they have time to combine with additional free vacancies in the cell wall. Because fiber and cell wall thicknesses have an intrinsic dependence on vacancy and self-interstitial diffusion rates in the target material, temperature will have a large influence on the final structure size.

Although this line of reasoning is very qualitative, it does match up fairly well with experimental data, in which Ge, GaSb, and InSb structures, which were all formed by room temperature irradiation, resulted in fiber and cell wall thicknesses of 15 to 30 nm, whereas Si structures, which formed at higher temperatures and under conditions of greater vacancy diffusivity, resulted in average cell wall thicknesses of over 40 nm.

In addition to diffusion kinetics, surface energy minimization may also influence the final structure size of irradiation-induced porous semiconductors. Similar to how carbon nanotubes have set chiralities that result in energetically favorable nanotube orientations, irradiation-induced nanofibers in GaSb and InSb may also form in a limited range of diameters due to energetically favorable configurations of their surfaces at those dimensions. *Ab initio* surface energy minimization computer simulations of irradiation-induced porous semiconductors were considered, and the idea was broached to several collaborators, but after careful consideration of the sizes of the structures involved, it was determined that the computing power required to perform the simulations was prohibitively large. While diffusion and surface energy considerations may play a role in the geometry of irradiation-induced porous structures, further analytical and computational work is needed in this area to produce a more comprehensive model relating material parameters to porous network morphology and fiber size.

Bibliography

1. N. Nitta, M. Taniwaki, Y. Hayashi, and T. Yoshiie, Formation of Cellular Defect Structure on GaSb Ion-implanted at Low Temperature. *J. Appl. Phys*. **92**, 1799 (2002).

2. G. E. Jellison, Oak Ridge National Laboratories. Personal Communication, August 17, 2009.

3. C. Boissiere, D. Grosso, S. Lepoutre, L. Nicole, A. B. Bruneau, and C. Sanchez, Porosity and Mechanical Properties of Mesoporous Thin Films Assessed by Environmental Ellipsometric Porosimetry. *Langmuir* **21**, 12362 (2005).

4. H. Huber, W. Assmann, S. A. Karamian, A. Mücklich, W. Prusseit, E. Gazis, R. Grötzschel, M. Kokkoris, E. Kossionidis, H. D. Mieskes, and R. Vlastou, Void Formation in Ge Induced by High Energy Heavy Ion Irradiation. *Nucl. Instrum. Methods Phys. Res. B* **122**, 542 (1997).

5. J. F. Ziegler, J. P. Biersack, and U. Littmark, *The Stopping and Range of Ions in Solids*. (Pergamon Press, New York, **1985)**. Also see: http://www.srim.org

6. D. R. Olander, *Fundamental Aspects of Nuclear Reactor Fuel Elements*. (Technical Information Center, Office of Public Affairs, Energy Research and Development Administration; USA, 1976).

7. H. Wiedersich, On the Theory of Void Formation During Irradiation. *Radiat. Eff.* **12**, 111 (1972).

8. M. Shaanan, R. Kalish, and V. Richter, Changes in InSb as a Result of Ion Implantation. *Nucl. Instrum. Methods Phys. Res. B* **7/8**, 443 (1985).

9. S. M. Kluth, J. D. Fitz Gerald, and M. C. Ridgway, Ion-induced Porosity in GaSb. *Appl. Phys. Lett*. **86**, 131920 (2005).

10. CRC Handbook of Chemistry and Physics, 87th ed., edited by D.R. Lide (Taylor and Francis, New York, 2006).

11. H. Bracht, E. E. Haller, and R. Clark-Phelps, Silicon Self-Diffusion in Isotope Heterostructures. *Phys. Rev. Lett.* **81**, 393 (1998).

12. H. D. Fuchs, W. Walukiewicz, E. E. Haller, W. Dondl, R. Schorer, G. Abstreiter, A. I. Rudnev, A. V. Tikhomirov, and V. I. Ozhogin, Germanium ^{70}Ge/^{74}Ge Isotope Heterostructures: An Approach to Self-diffusion Studies. *Phys. Rev. B* **51**, 16817 (1995).

13. H. Bracht, S.P. Nicols, W. Walukiewicz, J.P. Silveira, F. Briones, and E.E. Haller, Large Disparity Between Gallium and Antimony Self-diffusion in Gallium Antimonide. *Nature* **408**, 69 (2000).

14. D. L. Kendall and R. A. Huggins, Self-diffusion in Indium Antimonide. *J. Appl. Phys*. **40**, 2750 (1969).

15. F. H. Eisen and C. E. Birchenall, Self-diffusion in Indium Antimonide and Gallium Antimonide. *Acta Metall.* **5**, 263 (1957).

16. J. A. Brinkman, On the Nature of Radiation Damage in Metals. *J. Appl. Phys*. **25**, 961 (1954).

17. L. Pelaz, L. A. Marqués, and J. Barbolla, Ion-beam-induced Amorphization and Recrystallization in Silicon. *Appl. Phys. Rev.* **96**, 5947 (2004).

18. K. Nordlund and R. S. Averback, Point Defect Movement and Annealing in Collision Cascades. *Phys. Rev. B* **56**, 2421 (1997).

19. J. Tersoff, Empirical Interatomic Potential for Silicon with Improved Elastic Properties. *Phys. Rev. B* **38**, 9902 (1988).

20. K. Nordlund, M. Ghaly, R. S. Averback, M. Caturla, T. Diaz de la Rubia, and J. Tarus, Defect Production in Collision Cascades in Elemental Semiconductors and FCC Metals. *Phys. Rev. B* **57**, 7556 (1998).

21. T. K. Chaki and J. C. M. Li, Radiation Damage in an Amorphous Lennard-Jones Solid: A Computer Simulation. *Philos. Mag. B* **51**, 557 (1985).

22. C. H. Woo and B. N. Singh, Production Bias due to Clustering of Point Defects in Irradiation-induced Cascades. *Philos. Mag. A* **65**, 889 (1992).

23. S. G. Mayr and R. S. Averback, Ion-irradiation-induced Stresses and Swelling in Amorphous Ge Thin Films. *Phys. Rev. B* **71**, 134102 (2005).

24. P. W. Anderson, Model for the Electronic Structure of Amorphous Semiconductors. *Phys. Rev. Lett.* **34**, 953 (1975).

25. J. Dong and D. A. Drabold, Atomistic Structure of Band-tail States in Amorphous Silicon. *Phys. Rev. Lett.* **80**, 1928 (1998).

26. R. Atta-Fynn, P. Biswas, and D. A. Drabold, Electron-phonon Coupling is Large for Localized States. *Phys. Rev. B* **69**, 245204 (2004).

27. M. Toulemonde, C. Dufour, and E. Paumier, Transient Thermal Process After a High-energy Heavy-ion Irradiation of Amorphous Metals and Semiconductors. *Phys. Rev. B*

46, 14362 (1992).

28. C. Dufour, E. Paumier, and M. Toulemonde, Electron-phonon Coupling and the Sensitivity of Metals to Irradiation with Swift Heavy Ions. *Nucl. Instrum. Methods Phys. Res. B* **122**, 445 (1997).

29. W. Wesch, C. S. Schnohr, P. Kluth, Z. S. Hussain, L. L. Araujo, R. Giulian, D. J. Sprouster, A. P. Byrne, and M. C. Ridgway, Structural Modification of Swift Heavy Ion Irradiated Amorphous Ge Layers. *J. Phys. D: Appl. Phys.* **42**, 1 (2009).

Chapter 9

Materials Properties of Nanoporous Semiconductors

For over a century, it has been known that the size of a material can affect its properties, beginning with the work of Pawlow showing that a solid body's surface energy affects its melting point.[1] Since then, research has shown that a number of other material properties can be affected by material size, but the majority of recent research has focused on quantum confinement effects in semiconductors, notably Canham's work showing photoluminescence in nanoporous silicon.[2] Specifically, quantum confinement refers to spatial confinement of particles in a material, such as electrons and holes, that results in a size-dependent shift in the energetics of the material, such as a blue shift in bandgap of semiconductors with decreasing material size. For the purposes of this dissertation, however, the concept of quantum confinement is used to describe any change in material properties due to changes in material size at the nanoscale.

In this chapter, two case studies of quantum confinement effects in irradiation-induced porous semiconductors are studied. First, thermal annealing of irradiation-induced GaSb nanofibers is shown to result in the formation of distinct core-shell fibers, and the phase decomposition process is explained via thermodynamic arguments. Next, optical shifts and increases in photoluminescence are observed and discussed for irradiation-induced porous structures in GaSb, InSb, Ge, and Si. Finally, future

experiments to test additional properties of the quantum-confined semiconductors are presented, and practical applications for the nanoporous semiconductors are discussed.

9.1 Thermally-induced Phase Decomposition of GaSb

Because of quantum confinement and surface passivation effects at the nanoscale, nanoporous semiconductors have been targeted as ideal materials for many optoelectronic and photovoltaic devices, including solar cells,[3] but while porous Si has been the focal point of much of the recent research, porous GaSb also exhibits a shift in its optical spectra and could be useful for device fabrication.[4] However, irradiation-induced GaSb nanofibers are of mixed amorphous and nanocrystalline character, as shown in Figure 4.2, and research indicates that quantum confinement effects which produce changes in the luminescence properties of a material are often dependent upon the material's crystallinity.[5] In this section, we investigate the effects of thermal annealing on the crystallinity and composition of ion irradiation-induced GaSb nanofibers, and we comment on the unique chemical decomposition that is observed.

9.1.1 Core-Shell Nanofiber Analysis

General GaSb fiber morphologies are discussed in Section 4.1; Figure 9.1 presents a TEM analysis of as-formed GaSb nanofibers. BF imaging of the fibers performed in STEM mode showed relatively homogeneous fiber contrast dotted with some dark regions, likely indicating amorphous fibers containing small quantities of randomly oriented nanocrystals (Figure 9.1a). HRTEM imaging confirmed that there are some small nanocrystals present in the fibers (Figure 9.1b), but SAED analysis of the

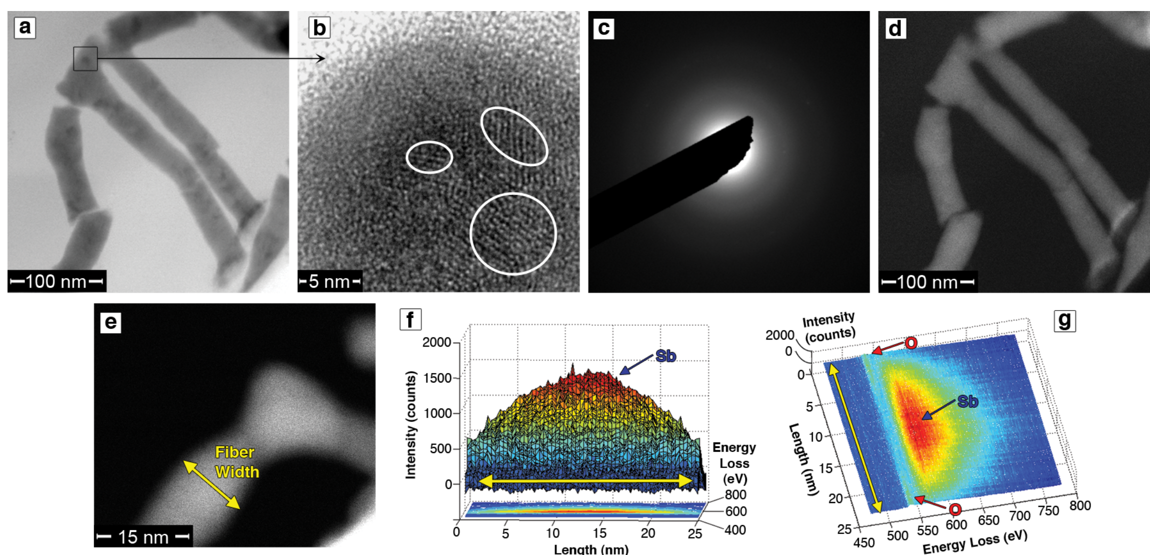

Figure 9.1. Crystallinity and composition of unannealed GaSb fibers. a) STEM BF imaging shows uniform contrast dotted with some small dark regions. b) HRTEM image of the region outlined in a) reveals several small nanocrystals. c) SAED of the fiber volume shows diffused halos indicating that the fibers are primarily amorphous. d) HAADF STEM generates uniform fiber contrast indicating that the fibers have uniform elemental distributions. e) HAADF image of a single fiber is shown. EELS line profiling of the fiber in e) reveals uniform elemental distributions throughout the fiber diameter, as exemplified in f and g. Uniform Sb distributions are shown, with noticeable O peaks evident in the outer surface of the fiber. Yellow arrows indicate the width of the scanned fiber in e, f, and g.

fiber mass indicated that the majority of the unannealed fibers were amorphous with only some discrete nanocrystallites enclosed (Figure 9.1c). HAADF imaging performed in STEM mode of the unannealed fibers showed no discernable contrast difference along the length or diameter of the nanofibers, indicating that the fibers were of uniform composition (Figure 9.1d). XEDS performed in TEM mode was used to map the distributions of Ga and Sb in the fibers. Elemental maps of Ga and Sb showed a uniform distribution of the two elements throughout the as-irradiated fiber volume. EELS performed in STEM mode confirmed the XEDS data, revealing an even distribution of Sb within the fibers, but EELS analysis also revealed some oxidation of the fibers' outer surface (Figure 9.1e-g). The even distributions of Ga and Sb throughout the fibers,

combined with the presence of oxygen at the fiber surface, suggests growth of solid GaO_x and SbO_y on the fiber surfaces due to exposure to air.

Results from the TEM analysis of the annealed GaSb fibers are shown in Figure 9.2. BF STEM imaging of the fibers showed strong, diverse diffraction contrast from the fiber cores but weak contrast from the outer shells, suggesting preferential crystallization of the cores over the shells (Figure 9.2a). HRTEM confirmed that the fiber cores were crystalline and that the shells remained amorphous (Figure 9.2b), while SAED verified that the majority of the fiber volume was polycrystalline (Figure 9.2c). The size of the crystalline cores varied slightly with the local diameter of the fiber, but on average, the crystalline core size measured about 17 nm, with the full fiber diameter averaging about 25 nm, slightly smaller than the unannealed fiber diameter of ~27 nm. This reduced size indicates a loss of either Ga or Sb from the fibers, although the change in size could also be due to fiber densification. Furthermore, the wavy morphology of the annealed fibers can be attributed to Rayleigh instability, which causes long fibers to eventually decay into spherical particles according to a periodic wavelength determined by the fiber radius and length.[6]

The presence of the core-shell nanofibers indicates that thermal annealing induced a fundamental change in the microstructure of the nanofibers. After annealing, HAADF STEM imaging showed a clear difference in contrast between the fiber cores and fiber shells, indicating a difference in composition between the two regions (Figure 9.2d). XEDS performed in STEM mode on a single annealed nanofiber yielded detailed elemental maps showing the precise positions of Ga and Sb within the nanofibers. Ga (Figure 9.2f) was detected over the whole of the fiber while Sb (Figure 9.2g) was

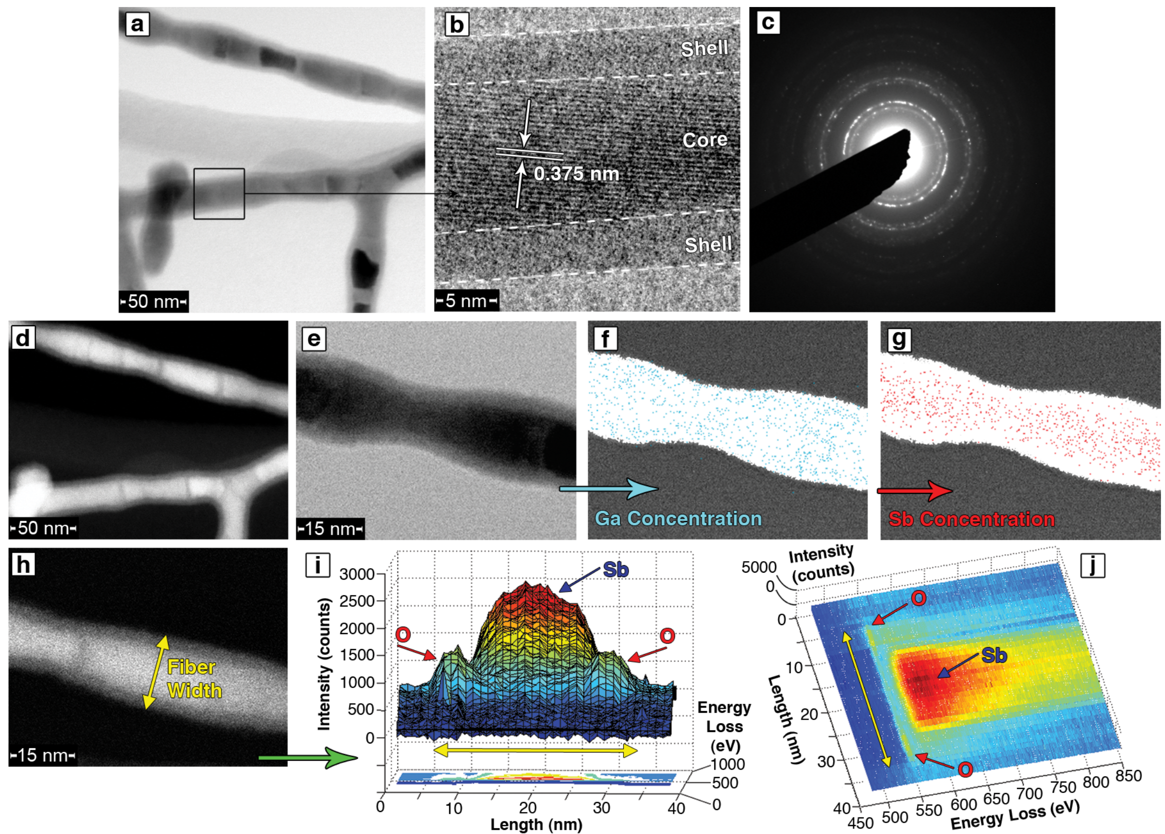

Figure 9.2. Crystallinity and composition of annealed GaSb fibers. a) BF STEM reveals crystalline differences between fiber regions. b) HRTEM of a single fiber shows distinct cores and shells. c) SAED of the fiber volume gives a distinct ring pattern, indicating primarily polycrystalline fibers. d) HAADF STEM also differentiates between the core and shell regions, indicating a difference in composition between the areas. e) XEDS maps in STEM mode show that f) Ga and g) Sb are separated into outer shell and inner core regions, respectively. h) A HAADF spectrum image of a single fiber is shown. i,j) EELS line profiling of the fiber in h) supports the XEDS data, yielding a relatively uniform Ga concentration from the fiber shell, but a sharp Sb concentration in the core region only, as seen in i. A noticeable oxygen peak is obtained from the shell region only, shown in i and j. Yellow arrows indicate the width of the scanned fiber in h, i, and j.

detected only from the fiber core. EELS performed in STEM mode was used to confirm the results from the XEDS elemental mapping experiments (Figure 9.2h-j). A line scan taken across the diameter of a fiber produced a fairly uniform Ga spectrum across the entire fiber width. Sb, however, was only detected from the section of the line map corresponding to the fiber core, thus suggesting that Sb exists exclusively in the fiber

core after annealing. A noticeable O peak was again detected in the outer shell region, indicating that the amorphous shell is composed of GaO_x.

Additionally, the polycrystalline SAED pattern of the annealed fibers was indexed to show a perfect rhombohedral Sb ring pattern. Measured d-spacing values matched computer-calculated values for the Sb crystal system remarkably well, with a maximum disagreement of less than 2%. Measured d-spacing values from the rhombohedral Sb ring pattern are shown in Table 9.1, and computer-calculated values obtained using the electron microscopy image simulation software EMS Online are included in Table 9.2. Figure 9.3 shows the electron diffraction pattern of the annealed nanofibers with rings corresponding to the diffraction patterns of Sb and GaSb superimposed over the original image. The SAED analysis confirms that the crystallites in the annealed fibers were rhombohedral Sb crystals rather than cubic GaSb. In addition, the lattice fringes from numerous HRTEM images of the annealed fibers were measured at 0.375 nm, as shown in Figure 9.2b, which correlates very closely with the spacing of the (100) and (010) planes in rhombohedral Sb, which have calculated lattice spacings of 0.373 nm. All the data, in conjunction with the elemental maps of Ga and Sb in the as-formed and annealed fibers, shows that the thermal annealing process causes Sb atoms in the fiber core to crystallize, while Ga atoms are expelled to the fiber shell region, where they organize into an amorphous GaO_x structure.

Table 9.1. Measured d-spacing values for ring pattern shown in Figure 9.3.

	Length, Center to Ring [pixels]	True Length, Center to Ring [cm]	d(hkl) [Å]
1)	102.5	0.163	3.788
2)	111.2	0.176	3.494
3)	127.3	0.202	3.051
4)	173.4	0.275	2.240
5)	182.6	0.290	2.127
6)	202.8	0.322	1.916
7)	212.0	0.336	1.832
8)	220.0	0.349	1.765
9)	248.8	0.395	1.561
10)	273.6	0.434	1.420

Table 9.2. Calculated d-spacing values for rhombohedral Sb.

	(h	k	l)	d(hkl) [Å]	Intensity
1)	0	0	3	3.758	3
2)	1	0	1	3.541	0.9
3)	0	1	2	3.111	100
4)	1	0	4	2.249	33.6
5)	1	1	0	2.154	31.7
6)	0	1	5	1.93	2.9
7)	0	0	6	1.879	5.3
7)	1	1	3	1.868	2.1
	0	2	1	1.84	0.1
8)	2	0	2	1.771	15.1
9)	0	2	4	1.555	8.4
	1	0	7	1.479	1.9
	2	0	5	1.437	0.9
10)	1	1	6	1.416	10

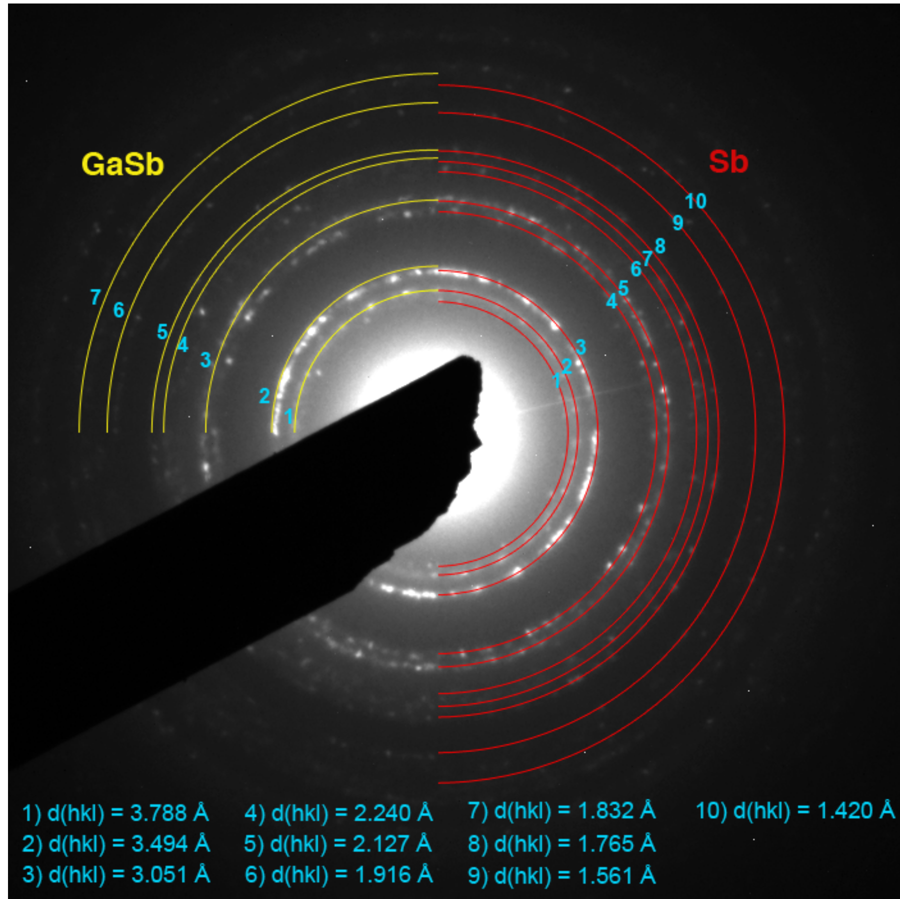

Figure 9.3. SAED pattern of the annealed GaSb nanofiber volume. Diffraction rings corresponding to rhombohedral Sb and cubic GaSb are superimposed over the pattern. Listed d-spacing values are for rhombohedral Sb.

9.1.2 Mechanism of Phase Decomposition

The complete chemical decomposition of the GaSb fibers during low temperature annealing goes against expected annealing results predicted by bulk GaSb thermodynamics. From the Ga-Sb phase diagram, shown in Figure 9.4, it can be seen that the ß phase, a 50-50 atomic percent mixture of Ga and Sb, is thermodynamically stable to a temperature of 709.6°C,[7] yet in our annealing experiments at 250°C, only 50% of the bulk melting temperature, complete elemental segregation occurred in the GaSb fibers. In the literature, annealing of bulk GaSb has shown normal behavior typical of III-V semiconductors. At low temperatures (250-400°C), annealing improves the atomic order of the crystal structure, while at higher temperatures (greater than 400°C), desorption and evaporation of Sb leads to the formation of Ga droplets in addition to the stoichiometric ß phase.[8]

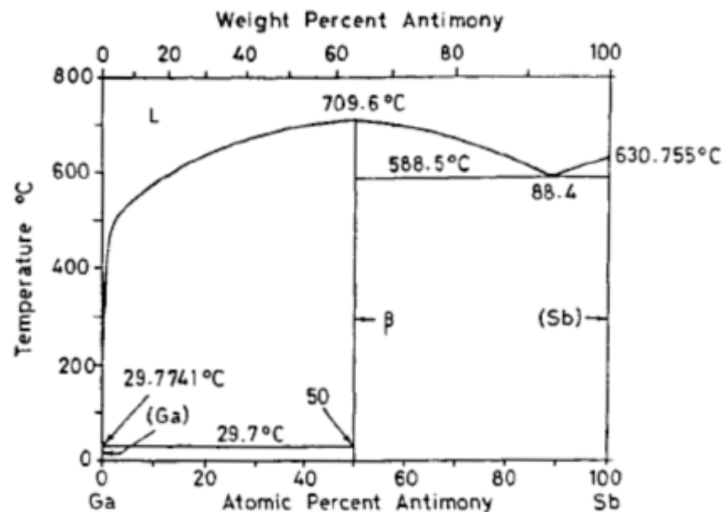

Figure 9.4. GaSb phase diagram, from Reference 7.

Early studies of ion-irradiated GaSb reported anomalous annealing behavior,[9] and Raman scattering measurements taken by Kim *et al.* showed that annealing of Ga^+ ion-implanted GaSb resulted in excitation of characteristic Sb peaks.[10] However, no TEM

experiments were completed, and the results were attributed to Sb desorption and out-diffusion effects in the material. In light of the new TEM data, these explanations are not sufficient to explain the resulting chemical decomposition of the fibers. The compositional changes in the nanofibers seem to be due to size-dependent effects that develop at the nanoscale. Research throughout the past century has shown that the size of an elemental particle affects its melting point, however research in nanoscale alloys is much more recent.[1,11,12] Studies have shown that nanosized alloy particles exhibit different phase diagrams than bulk alloys, specifically: melting temperatures are depressed, and phases that are normally present at specific alloy compositions may no longer be stable. The smaller the particle, the more exaggerated the thermodynamic changes.[13] Similarly, in structures larger than a couple hundred nanometers in size, the thermodynamic changes may be undetectable. Experiments in amorphous GaSb thin films of 200 to 1200 nm in thickness, for example, reported no anomalous annealing behavior.[14]

Abnormal nanoscale behavior has generally been attributed to two main phenomena. First, material properties will deviate when particles are of the same size as the characteristic lengths associated with the properties, and second, bulk material interactions will compete with interface and surface interactions in small particles.[15] In the case of this study, it would appear that the change in thermodynamic properties of the GaSb fibers would be a function of the latter effect. The decomposition of the GaSb nanofibers may be primarily a result of enhanced Sb volatility at the nanoscale. Elemental volatility is expected to be enhanced in nanostructures due to the Gibbs-Thomson effect, which essentially states that small particles with a high surface curvature exhibit a higher

effective vapor pressure, making them more volatile, due to increased surface effects in comparison to the particle volume. In addition, Sb has been shown to preferentially sublimate from GaSb surfaces at fairly low temperatures,[8] perhaps in part due to the much lower enthalpy of sublimation of Sb (ΔH_{sub} = 88 kJ/mol) than that of Ga (ΔH_{sub} = 259.5 kJ/mol).[16] XEDS and EELS data showing no Sb in the fiber shells supports the idea of high Sb volatility in the nanofibers. Keeping in mind that the outer shells of the fibers are likely composed of a mixture of GaO_x and SbO_y, the loss of Sb from the fiber surface would result in a metastable, oxygen-rich GaO_x shell. Due to an abnormally high relative diffusivity of Ga in GaSb,[17] Ga atoms in the core may be able to react with excess O at the shell interface, forming stable Ga_2O_3 in the shell and leaving only Sb atoms in the core, where they crystallize in the rhombohedral Sb phase. The Ga_2O_3, meanwhile, would remain in an amorphous state, due to the relatively high crystallization temperature of stable ß-Ga_2O_3.[18]

From our observations, the presence of O in the system seems to play a key role in the phase transformation process, as the oxidation of the GaSb nanofibers turns the material into a tertiary Ga-Sb-O system. To determine if the proposed core-shell formation mechanism is energetically favorable, the Gibbs free energy of the reaction:

$$4GaSb_{(s)} + 2Ga_2O_{3,(s)} + 2Sb_2O_{3,(s)} \rightarrow 4Sb_{(s)} + 4Ga_2O_{3,(s)} + Sb_{4,(g)} \quad (9.1)$$

was calculated using the following equations:

$$\Delta G_{rx} = \Sigma\Delta G_f^\circ{}_{, products} - \Sigma\Delta G_f^\circ{}_{, reactants} \quad (9.2)$$

$$\Delta G_f^\circ = \Delta H_f^\circ - T\Delta S^\circ \quad (9.3)$$

where ΔG_f° is the standard Gibbs energy of formation, ΔH_f° is the standard enthalpy of formation, T is the reaction temperature, and ΔS° is the standard entropy. Values for ΔH_f°

and $\Delta S°$ at elevated temperature were calculated by integration of the standard molar heat capacity, $C_p°$,[19] using reference values for $\Delta H_{298}°$ and $S_{298}°$ at standard conditions.[16,19,20] For Eq. 9.1 at 250°C, the Gibbs free energy is -413.7 kJ/mol, or -103.4 kJ/mol per mol of GaSb reactant, indicating that the transformation of the nanofibers into the core-shell configuration is energetically favorable. Of course, in our calculation we assume that the oxides are Ga_2O_3 and Sb_2O_3, when in truth our reactants consist of amorphous oxides, so we cannot use Eq. 9.1 as a true representation of the reaction. Calculation of the phase transformation assuming a reactant of Ga_2O instead of Ga_2O_3 results in a positive ΔG_{rx}, while assuming a reactant of Sb_2O_5 instead of Sb_2O_3 results in a more strongly negative ΔG_{rx}. Ultimately, however, this calculation serves to show that the proposed core-shell formation mechanism is feasible from a thermodynamic perspective.

Figure 9.5 presents a schematic of the proposed core-shell fiber formation process. Irradiation of GaSb occurs in vacuum, resulting in the formation of GaSb nanofibers, as shown in Figure 9.5a. Once the irradiated sample is removed from the implantation chamber and exposed to air, oxidation begins to occur at the fiber surface, as shown in Figure 9.5b. Given enough time, oxidation of both Ga and Sb is expected to occur. Formation of Ga_2O_3 ($\Delta G_f°$ = -998.4 kJ/mol) and Sb_2O_5 ($\Delta G_f°$ = -829.1 kJ/mol) is most energetically favorable, but Ga_2O ($\Delta G_f°$ = -128.4 kJ/mol) and Sb_2O_3 ($\Delta G_f°$ = -613.1 kJ/mol) may also form. During the annealing process, Sb evaporates from the shell, allowing Ga in the fiber core to react with excess oxygen in the shell, as shown in Figure 9.5c. By performing the annealing experiments in inert gas, no further oxidation was able to occur during the annealing process, showing that the core-shell formation process is not a result of oxidation. The loss of Sb from the shell is crucial in the formation of the

nanofibers, as it provides a driving force for the phase separation of the GaSb in the core. In addition, noticeable oxidation of the unannealed GaSb fibers provides additional evidence that the oxidation process itself does not cause phase separation.

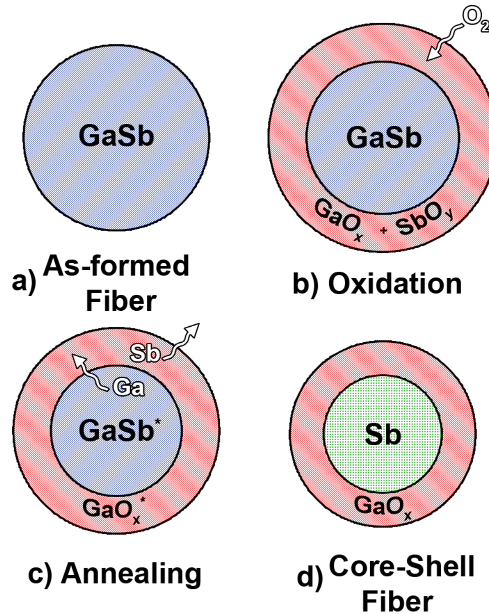

Figure 9.5. Schematic of the core-shell formation mechanism, shown by fiber cross-sections at different intervals of the process. a) Initially, the fibers are formed via irradiation in vacuum. b) After removal from the irradiation chamber, the nanofibers are exposed to air, causing them to oxidize, creating both GaO_x and SbO_x and slightly increasing the total fiber volume. c) During annealing, Sb volatilizes from the outer layer, and Ga in the core reacts with excess O in the shell. d) The final result is a core-shell nanofiber with a crystalline Sb core and an amorphous GaO_x shell. The * indicates transitional phases.

Although it is possible that the implanted ion species used to fabricate the GaSb fibers could act as a seed to cause elemental segregation during the annealing process, it is unlikely that the elemental segregation in the fibers is due to interference by the implanted ion species, as the same temperature-induced chemical degradation effect occurred in samples irradiated with 1 MeV Au^+ ions and in 150 keV Kr^+ ion-irradiated samples provided by Dr. Sha Zhu. Lastly, phase decomposition has been reported in

GaSb under very specific electron irradiation conditions, but only under simultaneous low-energy electron beam excitation (at 75 kV or less) and sample heating (at temperatures lower than 170°C), where a combination of thermal energy and electronic excitation can cause breakage of atomic bonds.[21,22] Our experiments, which used *ex situ* thermal annealing followed by TEM analysis, conclusively show that the phase decomposition we observed is thermally induced and is not a function of any analysis techniques.

Ultimately, the data suggests that the core-shell fiber formation process is a function of size-dependent oxidation, evaporation, and diffusion effects. Due to their small size, the GaSb fibers oxidize in air at room temperature to a proportionately high extent. Similarly during the annealing process, the small size of the fibers leads to a proportionately large loss of Sb through evaporation, even at very low temperature, leading to a fully Sb-depleted shell. Finally, the small size of the fiber core allows Ga to diffuse to the core-shell interface and react with excess O. This results in several size-dependent effects acting in unison to produce a unique nanoscale core-shell phase separation process.

9.2 Optical Properties of Nanoscale Semiconductors

The discovery of photoluminescence in nanostructured Si sparked a vast array of investigation into quantum confinement effects in semiconductors and has lead to research focused on engineering of everything from silicon lasers to electronic-photonic hybrid computers.[2,23,24] Given the inherently quantum confined nature of irradiation-induced porous semiconductors, these materials could provide a simple way for precision

fabrication of optical networks in semiconductor microdevices. In this section, the effects of irradiation-induced porosity on the photoluminescence of GaSb, Ge, InSb, and Si are discussed.

9.2.1 Changes in Luminescent Intensity

Luminescent intensity as a function of photon wavelength for various Ge, GaSb, InSb, and Si samples is shown in Figure 9.6. For Ge (Figure 9.6a), the highest increase in photoluminescence (PL) occurred in samples irradiated with 30 keV Ga^+ ions and later annealed. As shown earlier, irradiation of Ge results in amorphization in addition to fiber formation, and annealing results in recrystallization. While the PL spectrum of amorphous, irradiated Ge did not vary significantly from bulk crystalline Ge, the annealed, nanocrystalline Ge fiber structure showed a clear increase in PL intensity. In addition, the more porous, interconnected structure formed via 30 keV ion irradiation exhibited an increase in PL intensity, while the intensity for the more columnar, cellular structure formed in Ge irradiated with higher energy ions did not result in a PL increase. Experimental evidence and computer calculations show that increases in PL in Ge are due to both Ge oxide defects and size-dependent quantum confinement effects.[25]

GaSb (Figure 9.6b) seemingly exhibited opposite behavior to the Ge samples in that GaSb irradiated with 30 keV Ga^+ did not exhibit a large increase in PL intensity while samples irradiated with higher energy Sn^+ or Au^+ did see a significant increase. Of course, when comparing microstructures, we see that the GaSb nanofibers formed via high energy, high dose ion irradiation more closely resemble Ge structures formed at 30 keV, indicating that the small size of the nanofibers is responsible for the increases in PL

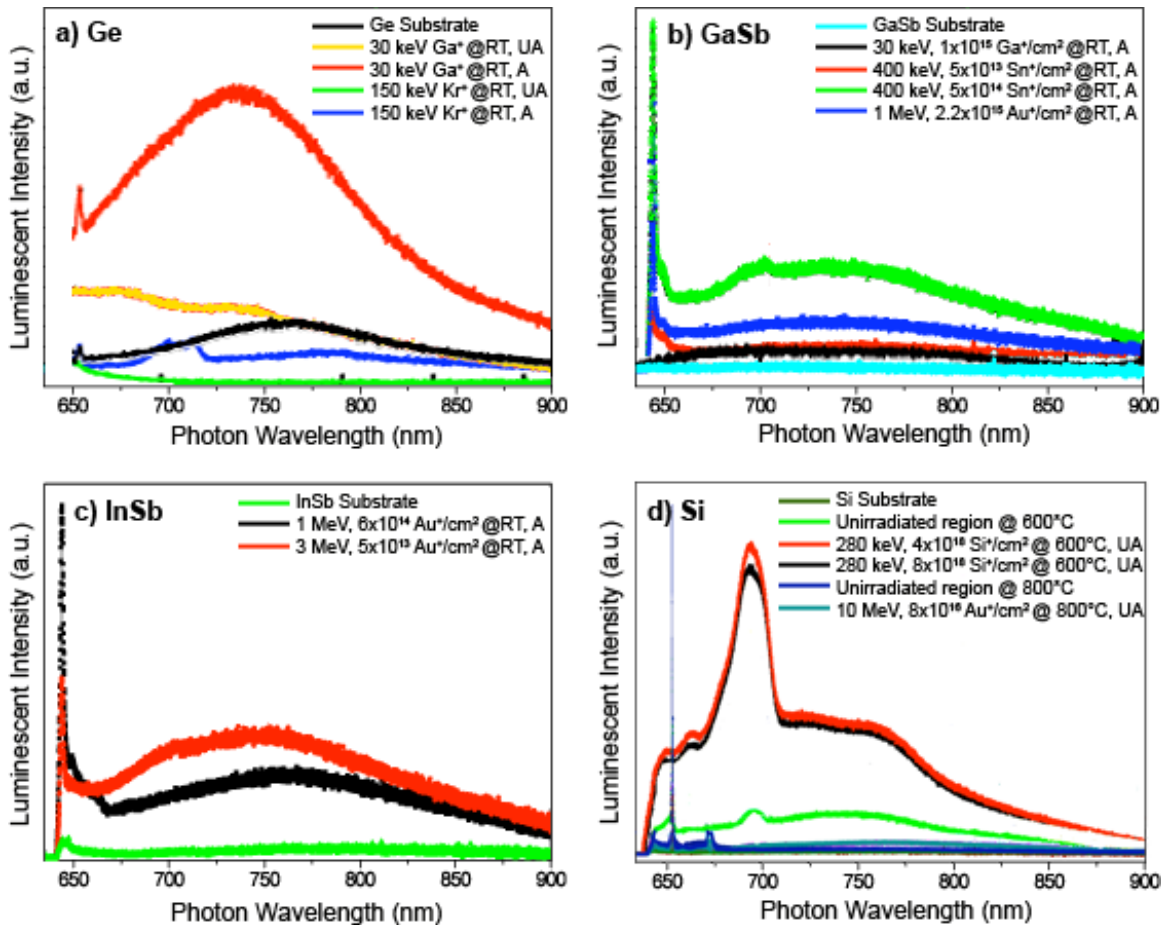

Figure 9.6. Luminescent intensity versus photon wavelength for irradiated a) Ge, b) GaSb, c) InSb, and d) Si samples. Luminescent intensity is given in arbitrary units. For each curve, ion energy, ion fluence, and irradiation temperature is given, where applicable and available. UA stands for unannealed, while A stands for annealed samples.

intensity. While PL increases across a broad range of photon energies were modest, several high energy samples exhibited a sharp peak at a photon wavelength of about 640 nm, which was not observed in previous experiments.[4] Similar results were seen in the InSb samples (Figure 9.6c), which of course had similar nanofiber morphologies to those in GaSb. Although quantum confinement effects can be assumed to be responsible for the sharp increase in PL intensity, no literature studies have been performed on PL of irradiation-induced InSb nanostructures.

In Si (Figure 9.6d), irradiation to lower ion fluences did not noticeably alter the PL intensity of the samples, which is to be expected because experimentation showed no change in morphology of these samples. However, Si irradiated with 280 keV Si^+ to fluences above 1×10^{18} ions/cm^2 exhibited noticeable changes in surface morphology and, correspondingly, showed a marked increase in PL intensity. All Si samples exhibited a sharp Raman peak at just over 650 nm. Changes in PL intensity in Si have been shown to be a function of both quantum confinement and surface passivation effects, as well as results of defect structures such as in Ge.[25,26]

Bibliography

1. P. Z. Pawlow, The Dependency of the Melting Point on the Surface Energy of a Solid Body. *Phys. Chem.* **65**, 1 (1909).

2. L. T. Canham, Silicon Quantum Wire Array Fabrication by Electrochemical and Chemical Dissolution of Wafers. *Appl. Phys. Lett.* **57**, 1046 (1990).

3. L. Stalmans, J. Poortmans, H. Bender, M. Caymax, K. Said, E. Vazsonyi, J. Nijs, and R. Mertens, Porous Silicon in Crystalline Silicon Solar Cells: A Review and the Effect on the Internal Quantum Efficiency. *Prog. Photovolt. Res. Appl.* **6**, 233 (1998).

4. Y. A. Danilov, A. A. Biryukov, J. L. Gonçalves, J. W. Swart, F. Iikawa, and O. Teschke, Photoluminescence and the Raman Scattering in Porous GaSb Produced by Ion Implantation. *Semiconductors* **39**, 145 (2005).

5. A. G. Cullis, L. T. Canham, and P. D. J. Calcott, The Structural and Luminescence Properties of Porous Silicon. *J. Appl. Phys*. **82**, 909 (1997).

6. F.A. Nichols and W.W. Mullins, Surface- (Interface-) and Volume-diffusion Contributions to Morphological Changes Driven by Capillarity. *Trans. Metal. Soc. AIME* **233**, 1840 (1965).

7. P. S. Dutta, H. L. Bhat, and V. Kumar, The Physics and Technology of Gallium Antimonide: An Emerging Optoelectronic Material. *J. Appl. Phys*. **81**, 5821 (1997).

8. M. Nouaoura, F. W. O. Da Silva, N. Bertru, M. Rouanet, A. Tahraoui, W. Oueini, J. Bonnet, and L. Lassabatere, Modification of GaSb (100) Surfaces Induced by Annealing Under Vacuum and Under Sb_4 and As_4 Flux. *J. Crystal Growth* **172**, 37 (1997).

9. S. J. Pearton, A. R. Von Neida, J. M. Brown, K. T. Short, L. J. Oster, and U. K. Chakrabarti, Ion Implantation Damage and Annealing in InAs, GaSb, and GaP. *J. Appl. Phys*. **64**, 629 (1988).

10. S. G. Kim, H. Asahi, M. Seta, J. Takizawa, S. Emura, R. K. Soni, S. Gonda, and H. Tanoue, Raman Scattering Study of the Recovery Process in Ga Ion Implanted GaSb. *J. Appl. Phys*. **74**, 579 (1993).

11. M. Takagi, Electron-diffraction Study of Liquid-solid Transition of Thin Metal Films. *J. Phys. Soc. Jpn.* **9**, 359 (1954).

12. P. R. Couchman and W. A. Jesser, Thermodynamic Theory of Size Dependence of Melting Temperature in Metals. *Nature* **269**, 481 (1977).

13. J. Weissmüller, P. Bunzel, and G. Wilde, Two-phase Equilibrium in Small Alloy Particles. *Scripta Mater*. **51**, 813 (2004).

14. J. H. Dias da Silva, J. I. Cisneros, M. M. Guraya, and G. Zampieri, Effect of Deviation from Stoichiometry and Thermal Annealing on Gallium Antimonide Films. *Phys. Rev. B* **51**, 6272 (1995).

15. G. Wilde, Nanostructures and Nanocrystalline Composite Materials – Synthesis, Stability and Phase Transformations. *Surf. Interface Anal*. **38**, 1047 (2006).

16. CRC Handbook of Chemistry and Physics, 87th ed., edited by D.R. Lide (Taylor and Francis, New York, 2006).

17. H. Bracht, S. P. Nicols, W. Walukiewicz, J. P. Silveira, F. Briones, and E. E. Haller, Large Disparity Between Gallium and Antimony Self-diffusion in Gallium Antimonide. *Nature* **408**, 69 (2000).

18. M. Zinkevich and F. Aldinger, Thermodynamic Assessment of the Gallium-oxygen System. *J. Am. Ceram. Soc.* **87**, 683 (2004).

19. M. Binnewies and E. Milke, *Thermochemical Data of Elements and Compounds, 2nd Ed.* (Wiley-VCH, Germany, 2002), p.p. 5, 544, 545, 741, 827-829.

20. A. M. Azad, R. Pankajavalli, and O. M. Sreedharan, Thermodynamic Stability of Sb_2O_3 by a Solid-oxide Electrolyte e.m.f Technique. *J. Chem. Thermodynamics* **18**, 255 (1986).

21. H. Yasuda, H. Mori, and J. G. Lee, Nonlinear Responses of Electronic-excitation-induced Phase Transformations in GaSb Nanoparticles. *Phys. Rev. Lett*. **92**, 135501 (2004).

22. H. Yasuda, H. Mori, and J. G. Lee, Electron-irradiation-induced Phase Separation in GaSb Nanoparticles. *Phys. Rev. B* **70**, 214105 (2004).

23. P. Ball, Let There be Light. *Nature* **409**, 974 (2001).

24. H. Rong, A. Liu, R. Jones, O. Cohen, D. Hak, R. Nicolaescu, A. Fang, and M. Paniccia, An All-silicon Raman Laser. *Nature* **433**, 292 (2005).

25. Y. M. Niquet, G. Allan, C. Delerue, and M. Lannoo, Quantum Confinement in Germanium Nanocrystals. *Appl. Phys. Lett.* **77**, 1182 (2000).

26. M. V. Wolkin, J. Jorne, P. M. Fauchet, G. Allan, and C. Delerue, Electronic States and Luminescence in Porous Silicon Quantum Dots: The Role of Oxygen. *Phys. Rev. Lett.* **82**, 197 (1999).

Chapter 10

Conclusions and Future Work

In this dissertation, experimental research on ion irradiation effects in Si, Ge, GaSb, and InSb has been performed and presented, analysis of the effects of varying irradiation parameters, environmental parameters, and materials properties on irradiation-induced nanostructure growth have been discussed, structure-specific mechanisms for porous network formation, evolution, and growth have been proposed, and a computational model has been developed as a starting point for modeling of porous network evolution in amorphous materials. In this chapter, conclusions are drawn from the work presented in the previous chapters, and future work that could further add to the current study is discussed.

10.1 Conclusions

Throughout the previous chapters, a great deal of experimental work was performed regarding the size, structure, and morphology of the irradiated semiconductors at different implantation conditions, and several important conclusions can be drawn from the data:

- Irradiation-induced voids can form in amorphous materials. The most prominent, expansive void networks formed in materials that amorphized either partially or

completely under ion irradiation. Although randomly oriented nanocrystals were present in some of the porous networks, the materials contained no recognizable long-range order, and as such, can be considered fully amorphous.

- Distinctly different irradiation-induced morphologies formed in the four tested materials: nanofibers in GaSb and InSb, cellular structures in Ge, and mesoporous and nanocave structures in Si. Despite performing various irradiation tests on each material using ions of different atomic numbers at varying acceleration energies and with a broad range of ion fluxes, the basic morphology of each material never changed dramatically. Overall, experiments indicate that fundamental differences in the irradiation-induced porous structures cannot be described solely by differences in dpa or temperature, which indicates that intrinsic materials properties of the target material play a large role in the porous network morphology. Nonetheless, similarities in these materials, such as in their bond and crystal structure, allow for some form of porous network formation, which distinguishes them from the vast maority of solids that do not form any porosity upon irradiation.
- Irradiaton-induced nanofiber and cell wall sizes tend to remain fairly constant across all experimental conditions; in particular, sizes tend to reach a steady state with increasing ion fluence. This indicates that not only does each material have a preferred irradiation-induced morphology, but each material also has a preferred structure size. While the reasons for this are not fully clear, surface energy minimization may play a role in the final diameter of irradiation-induced nanofibers.

- Porous layer thickness does not reach a steady state with increasing ion fluence, and no maximum layer thickness was observed for GaSb, InSb, and Ge. Although an increase in ion fluence does not necessarily result in increased void growth or swelling, the data unmistakably shows a continual growth in the porous layer with increased ion fluence and dpa, and the porous layer thickness far exceeds the projected ion range of the incoming energetic ions as predicted by TRIM, even when taking into account the decreased density of the resulting porous networks. This indicates that other factors besides ion irradiation-induced vacancy formation are important in porous layer growth, such as perhaps vacancy in-diffusion into the substrate.
- The homologous temperature of formation for porosity, or the ratio T/T_m at which porosity forms, is distinctly different for crystalline and amorphous materials. In crystalline metals, void swelling is typically maximized at homologous temperatures of around 0.5. For example, peak void swelling occurs in stainless steel, copper, and nickel at homologous temperatures of roughly 0.49, 0.57, and 0.51, respectively.[1-3] In Si, which remained crystalline during ion irradiation, void swelling was maximized at a temperature of about 650°C, equivalent to a homologous temperature of about 0.55. GaSb, InSb, and Ge, which were all amorphized by the ion irradiation process, all exhibited massive amounts of void swelling despite homologous irradiation temperatures of about 0.31, 0.38, and 0.25, respectively. This indicates that void swelling occurs at lower homologous temperatures in amorphous materials as compared to crystalline ones, and that the

semiconducting nature of the studied materials was not as important in porous network formation as the crystal structure. This conclusion is supported by a recent publication in which massive swelling was reported in an amorphous Si target irradiated with swift heavy ions at room temperature.[4]

- All the irradiation-induced porous semiconductor networks exhibited a distinct increase in photoluminescent intensity over the unirradiated bulk material within some range of excitation wavelengths. This is important because it indicates that quantum confinement effects that lead to increases in photoluminescence are not materials specific. Specifically, semiconductors with both direct and indirect bandgaps of varying band gaps and electron energies all exhibited some increase in photoluminescent intensity.

To summarize, several general conclusions can be drawn about irradiation-induced porous networks in semiconductors. Varying the irradiation and environmental conditions, such as ion energy, fluence, flux, can be used to tailor the porous layer thickness, depth, and degree of porosity, and sample temperature can be modified to maximize void swelling in the target material. However, porous layer morphology and fiber size cannot easily be changed and appear to be dependent on material properties. Porous network growth is easiest and most dramatic in amorphous or irradiation-amorphized semiconductors and occurs at lower homologous temperatures than void swelling in crystalline semiconductors or in metals. Finally, increased photoluminescent intensity seems to be a universal feature in nanostructured semiconductors, indicating that irradiation-induced porous networks may be useful for optoelectronic applications.

10.2 Future Work and Implications

Although Chapter 9 provided some insight into size-dependent materials property changes in porous materials, only a cursory investigation of these changes has been performed. Here, additional experiments intended to illuminate size-dependant properties of irradiation-induced porous materials are outlined, and some potential applications for the nanostructures are briefly discussed.

10.2.1 Future Experimentation

Although some thermal annealing tests were performed on GaSb, additional experiments are needed to better understand the effects of annealing on nanofibrous materials. Similar tests performed in InSb indicated that core-shell separation may not be confined to the GaSb system, although only one instance of core-shell InSb fibers was observed via TEM investigation. Although the mechanism proposed in Figure 9.3 may work for materials other than GaSb, it seems to be less effective in InSb. In addition, annealing may cause changes in microstructure morphology in other materials, including pure elements such as Ge. Preliminary results indicate that annealing of irradiation-induced porous Ge can, under the proper conditions, cause segregation of pores into semi-organized pore lattices. Several tests were performed at increasing annealing conditions, but not enough work has been completed to formulate a definitive model for the conditions responsible for pore migration and organization.

In addition to thermal and optical property measurements, mechanical properties of irradiation-induced nanofibers may also be different than in bulk samples. Nanoindentation studies of crystalline materials have shown large increases in yield

strength of nanopillars due to inhibited dislocation nucleation and motion in small volumes.[5,6] Although irradiation-induced nanofibers are either amorphous or nanocrystalline, they may nonetheless exhibit higher strength to volume ratios than bulk materials due to nanoscale strengthening effects. The difficulty in accurately measuring strengths of nanoporous materials during nanoindentation measurements, however, lies in uncertainty in the level of porosity of the samples. While techniques such as ellipsometric porosimetry could be used, assumptions must be made about the data that increase uncertainty in the final measurements. In addition to compressive yield strength tests, tensile and creep tests could provide further insight into mechanical properties of irradiation-induced porous materials.

Finally, further work is needed to elucidate the similarities and differences between porous silicon formed by ion irradiation and by chemical etching techniques. One of the primary reasons for extensive efforts trying to obtain porosity in silicon via ion irradiation was the knowledge that porous silicon could be formed through other techniques. The relative uniformity in the size and structure of chemically-etched porous silicon structures indicates that there is a driving force for creation of porous silicon of a distinct morphology. Despite forming porous silicon via ion irradiation, perfectly similar structures to that formed via chemical etching were not fabricated. Part of the problem may lie in the retained crystallinity of silicon under high temperature ion irradiation, as chemical etching does lead to amorphization of porous silicon.[7] Continued research into porous silicon formation in silicon, and in particular in fully amorphous silicon, is necessary for better understanding of pore formation mechanisms in silicon as a whole.

10.2.2 Potential Applications for Nanoporous Materials

Given the promising results of PL intensity tests, irradiation-induced porous semiconductors are prime candidates for electronic and photonic applications. Although such materials could be used for common photonic applications, such as waveguides and lasers, their uniqueness comes from their ability to be patterned easily, formed underneath solid surfaces, and have variable morphology that depends in part on the irradiation conditions. As previously noted, current technology involves use of chemical etchants to produce porous silicon.[8] While innovations in electrochemical etching, or anodization, that involve pre-irradiation of samples with He^{+} ions have allowed for more tunable etched porous silicon surfaces,[9] problems remain with any process that creates porosity through chemical etching. By purely using ion irradiation to create porous silicon and other porous semiconductors, etch masking and etching steps can be eliminated, reducing production costs, eliminating the use of dangerous chemicals, and allowing for fabrication of pores under previously deposited thin films.

Other potential applications for irradiation-induced porous materials are in catalysis and hydrogen storage due to their high surface area and large numbers of dangling bonds. In the case of catalysis, the porous layer could serve as a support structure for dispersed metal catalysts, a technique that has already shown promise in carbon-based systems.[10] Irradiated semiconductors may also have applications for hydrogen storage. Silicon dangling bonds in particular have been shown to react highly with hydrogen,[11] while other semiconductors, such as germanium, actually repel hydrogen from their dangling bonds.[12] If the processing of irradiation-induced porous structures in silicon can be improved to provide a higher void fraction and smaller void

sizes, then ion beam irradiation could have applications in processing materials for hydrogen storage. While ion irradiation has the critical shortcoming of being a purely near-surface process, innovative processing techniques could be used to create bulk porous material via ion irradiation, such as through irradiation of agitated silicon powders. While the ability of GaSb and InSb to store hydrogen has not been tested, use of either material in large-scale hydrogen storage processes would be prohibitively expensive due to the high costs of gallium and indium.

Another potential application for irradiation-induced porous semiconductors is in the fabrication of nanoscale chemical sensors. Due to their small size, nanoporous materials, as well as nanofibers and nanotubes, are potentially very useful in chemical detection. Detection of contaminant molecules is performed by reading changes in the resistance or capacitance of the sensor materials, which can result in sensors with detection thresholds of less than one part per million.[13] Although cost would not be an issue in the use of nanoscale chemical sensors due to the size of the devices created, the efficiency of porous semiconductor detectors is largely unknown, and irregularities in the porous network could make reliable detection difficult, especially since their performance would have to exceed that of carbon nanotubes to be useful.[14]

Bibliography

1. T. Kimoto, H. Shiraishi, and R. Watanabe, Void Swelling of Solution-annealed Type 316 Stainless Steel Under Long Time Proton Irradiation. *J. Nucl. Sci. Tech.* **19**, 202 (1982).

2. V. R. Barabash, A. A. Gervash, A. N. Naberenkov, E. V. Nesterova, V. V. Rybin and S. A. Fabritsiev, Microstructural Evolution and Swelling of Copper Alloys Under Irradiation. *J. Nucl. Mater.* **191-194**, 411 (1992).

3. N. H. Packan, K. Farrell, and J. O. Stiegler, Correlation of Neutron and Heavy Ion Damage I: The Influence of Dose Rate and Injected Helium on Swelling in Pure Nickel. *J. Nucl. Mater.* **78**, 143 (1978).

4. A. Hedler, S. Klaumünzer, and W. Wesch, Swift Heavy Ion Irradiation of Amorphous Silicon. *Nucl. Instrum. Methods Phys. Res. B* **242**, 85 (2006).

5. J. R. Greer and W. D. Nix, Nanoscale Gold Pillars Strengthened Through Dislocation Starvation. *Phys. Rev. B* **73**, 245410 (2006).

6. T. Zhu, J. Li, A. Samanta, A. Leach, and K. Gall, Temperature and Strain-Rate Dependence of Surface Dislocation Nucleation. *Phys. Rev. Lett.* **100**, 025502 (2008).

7. S. Shih, K. H. Jung, R.-Z. Qian, and D. L. Kwong, Transmission Electron Microscopy Study of Chemically Etched Porous Si. *Appl. Phys. Lett.* **62**, 467 (1993).

8. A. G. Cullis, L. T. Canham, and P. D. J. Calcott, The Structural and Luminescence Properties of Porous Silicon. *J. Appl. Phys*. **82**, 909 (1997).

9. E. J. Teo, M. B. H. Breese, A. A. Bettiol, D. Mangaiyarkarasi, F. Champeaux, F. Watt, and D. J. Blackwood, Multicolor Photoluminescence from Porous Silicon Using Focused, High-Energy Helium Ions. *Adv. Mater.* **18**, 51 (2006).

10. G. S. Chai, S. B. Yoon, J.-S. Yu, J.-H. Choi, and Y.-E. Sung, Ordered Porous Carbons with Tunable Pore Sizes as Catalyst Supports in Direct Methanol Fuel Cell. *J. Phys. Chem. B* **108***,* 7074 (2004).

11. J. Robertson, Deposition Mechanism of Hydrogenated Amorphous Silicon. *J. Appl. Phys*. **87**, 2608 (2000).

12. J. R. Weber, A. Janotti, P. Rinke, and C. G. Van de Walle, Dangling-bond Defects and Hydrogen Passivation in Germanium. *Appl. Phys. Lett.* **91**, 142101 (2007).

13. A. N. Shipway, E. Katz, and I. Willner, Nanoparticle Arrays on Surfaces for Electronic, Optical, and Sensor Applications. *Chem. Phys. Chem.* **1**, 18 (2000).

14. J. Kong, N. R. Franklin, C. Zhou, M. G. Chapline, S. Peng, K. Cho, and H. Dai, Nanotube Molecular Wires as Chemical Sensors. *Science* **287**, 622 (2000).

Appendix 1

Irradiation-induced Fiber, Cell Wall, and Pore Sizes

This appendix includes fiber diameter, cell wall thickness, and pore diameter measurements for irradiated samples. The parameters measured depend on the morphology of the irradiated system in question. Fiber diameter measurements were made on: GaSb and InSb irradiated with 1, 2, and 3 MeV Au^{+} ions at EMSL. Cell wall measurements were made on: Ge irradiated with 1, 2, and 3 MeV Au^{+} ions at EMSL. Pore size measurements were made on: Si irradiated with 9 MeV Au^{3+} ions at EMSL and 280 keV Si^{+} ions at MIBL. All measurements were taken from around the middle of the resulting porous layer thickness. No measurements were recorded near the end of the porous layer in samples irradiated with high-energy ions, such as the region shown in Figure 4.1d, due to the gradually changing size of the structures involved. Similarly, size measurement data sets were not collected for samples irradiated with low-energy ions at EMAL due to the rapidly changing morphologies observed under FIB irradiation at these conditions. All fiber, wall, and pore size values are given in nm, and the average, variance, and standard deviation for each data set are given.

Fiber diameter measurements:

Ion/Material	1 MeV, 4.4e13	1 MeV, 1e14	1 MeV, 2e14	1 MeV, 4e14	1 MeV, 6e14
Au^+ in GaSb	23.40	20.89	17.83	17.32	16.03
	29.81	22.57	21.48	24.05	19.43
	23.51	20.41	17.21	22.35	21.60
	23.85	15.09	20.70	22.83	18.55
	23.85	20.75	24.97	26.70	20.92
	22.38	21.73	24.69	19.63	19.84
	23.85	22.15	20.64	24.59	23.64
	22.38	23.06	22.72	17.93	17.60
	19.01	15.09	21.09	19.02	20.38
	25.42	26.21	23.51	24.05	22.42
	21.03	20.75	20.87	21.54	23.64
	25.20	16.00	21.60	24.73	22.83
	18.90	14.81	20.47	26.70	19.23
	28.80	19.36	23.62	30.43	20.38
	23.51	17.89	17.55	30.10	21.13
	22.38	19.57	18.22	17.73	20.92
	19.80	24.88	20.47	26.09	23.44
	23.62	17.26	20.02	17.80	21.81
	30.03	20.41	21.20	28.33	18.00
	24.75	16.77	23.73	25.68	21.40
	22.05	20.48	19.57	18.61	19.43
	21.93	20.41	17.83	20.72	20.92
	18.34	12.93	30.76	19.16	21.74
	22.16	23.48	22.55	27.99	20.24
	20.36	19.43	23.45	27.04	21.94
Average [nm]	23.21	19.70	21.47	23.24	20.70
Variance:	9.36	10.95	8.74	16.96	3.65
Standard Dev.:	3.06	3.31	2.96	4.12	1.91

Ion/Material	1 MeV, 1e15	1 MeV, 2.2e15	1 MeV, 6e15	2 MeV, 3.9e13	2 MeV, 8e13
Au^+ in GaSb	-	23.35	22.83	19.73	-
	-	18.87	20.86	26.16	-
	-	15.97	28.80	17.71	-
	-	29.04	23.85	13.15	-
	-	22.93	24.05	16.14	-
	-	24.80	24.12	19.58	-
	-	24.20	24.18	22.80	-
	-	23.05	20.79	18.83	-
	-	21.23	20.72	19.51	-
	-	21.05	21.67	23.92	-
	-	22.63	21.54	22.80	-
	-	24.50	26.63	22.20	-
	-	25.41	29.42	23.69	-
	-	17.79	19.90	19.06	-
	-	19.96	26.09	21.90	-

	-	21.66	18.00	24.29	-
	-	23.35	25.00	19.81	-
	-	22.44	28.94	24.29	-
	-	22.20	22.28	26.01	-
	-	23.17	21.20	31.24	-
	-	14.34	20.72	19.06	-
	-	22.02	16.17	26.98	-
	-	24.50	22.96	19.73	-
	-	23.41	25.48	15.84	-
	-	22.44	21.26	23.54	-
Average [nm]	-	22.17	23.10	21.52	-
Variance:	-	9.32	10.79	15.91	-
Standard Dev.:	-	3.05	3.29	3.99	-

Ion/Material	**2 MeV, 1.4e14**	**2 MeV, 2.4e14**	**3 MeV, 5.1e13**	**3 MeV, 1e14**	**3 MeV, 2e14**
Au^+ in GaSb	22.51	25.06	20.04	17.13	27.12
	27.83	20.26	20.58	23.33	22.57
	24.38	25.06	20.04	30.24	24.27
	22.58	22.13	18.48	23.33	18.31
	17.70	22.51	24.36	24.19	21.27
	25.81	26.03	19.44	26.21	19.90
	23.03	26.41	17.52	22.03	29.76
	25.43	27.98	20.28	23.40	23.62
	25.21	33.91	19.02	21.60	19.86
	24.16	21.91	20.04	22.17	20.37
	22.36	25.36	15.66	22.46	28.64
	24.38	19.65	24.96	17.06	18.56
	20.48	17.85	19.80	20.59	26.33
	22.28	17.10	25.86	18.43	24.23
	24.31	26.78	21.66	21.60	23.51
	21.98	20.26	18.66	27.86	21.81
	24.08	20.26	28.20	20.37	25.03
	21.46	33.38	20.16	22.03	18.42
	16.80	23.33	16.86	27.07	20.66
	24.68	19.28	23.10	24.19	28.93
	23.48	21.68	22.02	25.05	12.46
	22.28	22.88	26.58	22.46	18.20
	21.91	22.96	23.34	18.36	20.98
	21.08	13.95	22.02	25.56	22.61
	36.98	26.03	20.04	21.09	21.70
Average [nm]	23.49	23.28	21.15	22.71	22.36
Variance:	13.57	20.95	9.50	10.43	15.73
Standard Dev.:	3.68	4.58	3.08	3.23	3.97

Ion/Material	**1 MeV, 5e13**	**1 MeV, 1.25e14**	**1 MeV, 3e14**	**1 MeV, 6e14**	**1 MeV, 8.4e14**
Au^+ in InSb	28.98	24.36	30.17	23.33	23.41
	30.18	32.06	26.99	24.53	26.11
	28.98	32.51	30.17	21.08	25.06

	31.67	37.59	26.84	21.23	25.06
	29.28	35.12	26.99	21.91	26.63
	39.14	20.48	28.81	22.36	28.06
	26.29	38.95	29.49	23.11	21.08
	27.79	22.65	28.43	24.38	21.91
	33.15	28.62	32.98	22.96	23.03
	33.16	39.33	30.02	23.56	27.53
	37.05	34.16	30.63	24.01	25.51
	31.67	36.92	27.60	24.38	24.31
	30.18	31.17	35.03	22.88	22.28
	29.28	33.33	30.33	24.23	23.33
	29.28	32.15	31.54	20.26	25.06
	33.46	32.36	32.22	24.23	24.16
	24.20	35.58	29.49	19.13	20.86
	24.80	32.81	25.70	26.33	21.08
	25.10	34.01	28.20	22.88	24.01
	41.53	34.98	28.43	21.08	24.61
	26.59	38.94	36.85	23.11	21.46
	29.28	29.75	29.49	25.36	23.48
	27.85	37.44	30.17	24.31	24.83
	32.27	29.90	31.54	16.95	26.78
	31.67	28.03	30.40	19.88	25.21
Average [nm]	30.51	32.53	29.94	22.70	24.19
Variance:	17.87	24.47	6.42	4.49	4.09
Standard Dev.:	4.23	4.95	2.53	2.12	2.02

Ion/Material	2 MeV, 5e13	2 MeV, 1.2e14	2 MeV, 2e14	3 MeV, 5e13	3 MeV, 1e14	3 MeV, 2e14
Au^{+} in InSb	22.27	19.20	22.88	19.13	20.86	21.98
	20.11	18.45	21.68	26.86	27.08	22.96
	18.06	19.50	19.73	21.08	19.80	25.36
	25.52	21.91	27.16	23.03	21.76	20.11
	23.60	19.13	17.78	29.41	20.26	28.36
	26.49	21.08	20.93	25.06	20.93	22.43
	21.79	18.53	17.70	22.51	23.48	21.23
	20.71	21.08	18.23	20.48	22.73	21.08
	24.80	23.78	23.78	20.86	23.48	21.08
	26.49	23.48	23.03	27.01	19.43	22.88
	22.27	22.36	17.93	28.81	21.91	20.93
	31.78	20.03	20.71	21.91	19.80	18.75
	28.53	18.75	21.08	23.11	21.08	19.80
	30.34	22.96	33.16	20.56	19.80	18.75
	22.75	21.91	27.53	23.41	27.53	25.06
	30.10	22.43	19.88	16.28	23.78	19.13
	15.89	23.33	19.65	22.88	20.71	19.13
	28.89	21.46	23.41	26.41	20.93	20.11
	23.36	23.78	21.08	19.88	19.13	21.91
	28.53	24.31	25.21	21.91	21.08	21.01
	30.34	18.23	20.11	22.06	26.03	20.93
	17.82	22.06	19.13	21.08	22.73	19.80
	23.24	22.43	15.75	22.06	23.78	21.46
	29.26	22.13	26.78	19.35	14.78	19.80
	26.97	24.76	19.88	24.31	21.76	25.51

Average [nm]	24.80	21.48	21.77	22.78	21.79	21.58
Variance:	19.08	3.98	15.11	9.75	7.29	5.66
Standard Dev.:	4.37	1.99	3.89	3.12	2.70	2.38

Cell wall thickness measurements:

Ion/Material	**1 MeV, 1e15**	**1 MeV, 2.2e15**	**1 MeV, 6e15**	**1 MeV, 9e15**	**2 MeV, 2.9e14**
Au^+ in Ge	15.33	27.02	16.80	19.67	-
	25.92	34.14	20.04	23.91	-
	20.08	16.43	15.00	14.27	-
	15.33	17.62	16.68	14.40	-
	16.60	16.43	23.88	16.20	-
	17.70	14.15	30.00	20.31	-
	27.11	12.96	19.44	31.63	-
	12.96	17.70	12.72	18.64	-
	15.33	14.15	24.72	16.46	-
	16.43	27.02	18.60	15.17	-
	14.15	18.81	15.84	18.64	-
	30.58	16.52	23.88	19.67	-
	15.33	16.43	23.88	36.13	-
	14.15	22.36	20.04	19.29	-
	16.43	16.52	20.04	19.93	-
	18.81	15.33	20.16	27.26	-
	16.43	18.81	21.72	27.26	-
	15.33	21.18	18.36	16.46	-
	27.02	18.81	18.60	12.99	-
	15.33	25.92	22.20	16.07	-
	12.96	17.62	20.04	19.29	-
	23.55	22.36	22.68	20.83	-
	15.33	19.99	28.44	16.20	-
	32.95	17.70	20.16	24.81	-
	15.33	17.62	18.00	16.97	-
Average [nm]	18.66	19.34	20.48	20.10	-
Variance:	32.53	23.73	15.64	31.66	-
Standard Dev.:	5.70	4.87	3.96	5.63	-

Ion/Material	**2 MeV, 7.7e14**	**2 MeV, 1.7e15**	**3 MeV, 3.9e14**	**3 MeV, 1.05e15**	**3 MeV, 2.32e15**
Au^+ in Ge	-	20.05	-	23.36	17.74
	-	15.13	-	21.75	15.94
	-	18.49	-	24.98	23.08
	-	18.31	-	17.51	18.27
	-	17.53	-	20.73	17.74
	-	17.17	-	28.68	18.80
	-	13.33	-	16.61	19.85
	-	16.03	-	19.24	16.69
	-	25.87	-	21.72	17.82
	-	16.45	-	18.36	19.85
	-	16.69	-	21.81	26.09

	-	20.83	-	18.96	20.08
	-	11.10	-	18.36	13.61
	-	21.37	-	19.56	16.69
	-	18.37	-	21.72	15.71
	-	16.03	-	21.96	15.64
	-	18.37	-	21.72	15.64
	-	21.67	-	21.72	13.76
	-	9.30	-	23.40	18.80
	-	15.91	-	32.76	18.80
	-	15.91	-	18.60	17.82
	-	12.12	-	17.40	19.92
	-	13.45	-	24.24	18.50
	-	13.69	-	20.04	17.74
	-	14.77	-	21.72	18.80
Average [nm]	-	16.72	-	21.48	18.14
Variance:	-	13.23	-	12.85	7.09
Standard Dev.:	-	3.64	-	3.58	2.66

Pore diameter measurements:

Ion/Material	9 MeV Au^{3+}, 7.8e16	280 keV Si^+, 8e18, 170°C	280 keV Si^+, 8e18, 450°C	280 keV Si^+, 2e18, 650°C	280 keV Si^+, 8e18, 650°C
Au^{3+} and Si^+ in Si	24.16	28.25	79.21	192.08	448.29
	21.48	32.99	60.46	58.22	353.45
	24.16	30.43	200.12	93.04	101.16
	40.60	38.79	202.22	33.61	57.81
	31.88	34.58	44.10	200.48	422.70
	66.11	34.65	31.80	75.63	274.88
	66.11	54.16	58.36	533.61	149.63
	41.95	79.40	75.16	461.58	84.30
	26.85	12.96	49.05	163.87	266.14
	48.32	14.46	56.71	60.62	196.00
	47.32	114.50	29.85	76.83	307.39
	29.19	97.25	24.30	278.51	176.73
	50.00	37.66	20.55	305.52	159.57
	52.01	39.25	17.85	317.53	67.74
	52.01	23.58	16.80	1397.36	302.57
	44.63	23.58	34.50	217.29	121.03
	57.38	14.09	72.91	108.64	309.50
	17.79	12.66	108.76	142.26	392.29
	21.48	84.67	31.20	101.44	510.91
	26.85	54.99	31.20	153.06	424.21
	80.27	14.46	19.20	509.00	226.10
	28.43	18.31	17.85	540.22	161.07
	23.41	47.76	56.26	183.67	177.03
	18.39	90.47	73.06	231.09	127.05
	53.51	18.83	32.70	473.59	360.38
Average [nm]	39.77	42.11	57.77	276.35	247.12
Variance:	295.47	856.43	2421.70	80026.64	17201.29
Standard Dev.:	17.19	29.26	49.21	282.89	131.15

Appendix 2

Porous Layer Thicknesses

This appendix includes porous layer thickness measurements for samples irradiated with 1, 2, and 3 MeV Au^+ ions at EMSL. Only Ge, GaSb, and InSb are included, as EMSL irradiations of Si did not result in well-developed porous layers in Si. GaSb samples irradiated with 1 MeV Au^+ to 1×10^{15} ions/cm^2 and 2 MeV Au+ to 8×10^{13} ions/cm^2 were not included, as the sample surfaces were damaged during sample transport and preparation. Selected MIBL Si^+ irradiations of Si which produced measureable porous layer thicknesses are also included. Porous layer thickness was not tested for low-energy implantations performed at EMAL. All values are given in μm, and the average, variance, and standard deviation for each data set are given.

Ion/Material	**1 MeV, 1e15**	**1 MeV, 2.2e15**	**1 MeV, 6e15**	**1 MeV, 9e15**	**2 MeV, 2.9e14**
Au^+ in Ge	0.12	0.31	0.81	1.08	0.00
	0.13	0.32	0.86	1.11	0.00
	0.12	0.34	0.83	1.11	0.00
	0.12	0.31	0.83	1.13	0.00
	0.14	0.31	0.86	1.16	0.00
	0.13	0.31	0.89	1.08	0.00
	0.11	0.32	0.83	1.20	0.00
	0.12	0.28	0.89	1.16	0.00
	0.14	0.23	0.87	1.13	0.00
	0.12	0.31	0.87	1.16	0.00
	0.11	0.34	0.87	1.16	0.00
	0.12	0.34	0.82	1.16	0.00
	0.13	0.31	0.83	1.20	0.00
	0.12	0.32	0.83	1.11	0.00
	0.11	0.30	0.86	1.18	0.00
	0.12	0.32	0.82	1.16	0.00
	0.13	0.29	0.83	1.13	0.00
	0.13	0.35	0.84	1.16	0.00

	0.12	0.31	0.81	1.16	0.00
	0.14	0.30	0.82	1.16	0.00
	0.11	0.31	0.88	1.16	0.00
	0.10	0.32	0.86	1.18	0.00
	0.11	0.34	0.83	1.13	0.00
	0.12	0.31	0.88	1.13	0.00
	0.13	0.31	0.86	1.16	0.00
Average [um]	0.12	0.31	0.85	1.14	0.00
Variance:	0.00	0.00	0.00	0.00	0.00
Standard Dev.:	0.01	0.02	0.02	0.03	0.00

Ion/Material	**2 MeV, 7.7e14**	**2 MeV, 1.7e15**	**3 MeV, 3.9e14**	**3 MeV, 1.05e15**	**3 MeV, 2.32e15**
Au^+ in Ge	0.00	0.07	0.00	0.04	0.12
	0.00	0.08	0.00	0.05	0.13
	0.00	0.08	0.00	0.05	0.12
	0.00	0.10	0.00	0.04	0.14
	0.00	0.09	0.00	0.05	0.16
	0.00	0.10	0.00	0.06	0.14
	0.00	0.08	0.00	0.06	0.16
	0.00	0.07	0.00	0.03	0.15
	0.00	0.07	0.00	0.07	0.16
	0.00	0.07	0.00	0.05	0.14
	0.00	0.09	0.00	0.04	0.12
	0.00	0.08	0.00	0.05	0.14
	0.00	0.08	0.00	0.06	0.15
	0.00	0.07	0.00	0.04	0.15
	0.00	0.08	0.00	0.05	0.15
	0.00	0.08	0.00	0.05	0.14
	0.00	0.05	0.00	0.04	0.11
	0.00	0.09	0.00	0.05	0.14
	0.00	0.08	0.00	0.05	0.14
	0.00	0.08	0.00	0.04	0.17
	0.00	0.09	0.00	0.05	0.15
	0.00	0.08	0.00	0.04	0.09
	0.00	0.08	0.00	0.05	0.13
	0.00	0.10	0.00	0.04	0.12
	0.00	0.07	0.00	0.04	0.13
Average [um]	0.00	0.08	0.00	0.05	0.14
Variance:	0.00	0.00	0.00	0.00	0.00
Standard Dev.:	0.00	0.01	0.00	0.01	0.02

Ion/Material	**1 MeV, 4.4e13**	**1 MeV, 1e14**	**1 MeV, 2e14**	**1 MeV, 4e14**	**1 MeV, 6e14**
Au^+ in GaSb	1.76	2.08	3.77	5.95	6.27
	1.76	2.16	3.64	5.83	6.27
	1.78	2.20	3.62	5.93	6.13
	1.76	2.14	3.57	5.87	6.13
	1.77	2.18	3.60	5.90	6.13
	1.76	2.14	3.54	6.34	6.19

	1.76	2.21	3.66	6.37	6.17
	1.76	2.18	3.48	6.19	6.13
	1.76	2.14	3.56	6.34	6.13
	1.75	2.20	3.63	6.25	6.08
	1.76	2.21	3.62	6.28	6.25
	1.75	2.20	3.59	6.37	6.18
	1.76	2.15	3.63	6.28	6.23
	1.74	2.17	3.60	6.15	6.39
	1.76	2.17	3.52	6.12	6.27
	1.77	2.17	3.60	6.21	6.22
	1.75	2.18	3.57	6.15	6.22
	1.76	2.20	3.56	5.93	6.22
	1.78	2.13	3.57	5.87	6.39
	1.76	2.14	3.57	5.90	6.36
	1.76	2.18	3.57	5.96	6.13
	1.76	2.14	3.57	5.96	6.17
	1.76	2.15	3.60	5.93	6.13
	1.77	2.18	3.59	5.90	6.08
	1.76	2.14	3.60	5.85	6.08
Average [um]	1.76	2.16	3.59	6.07	6.20
Variance:	0.00	0.00	0.00	0.04	0.01
Standard Dev.:	0.01	0.03	0.05	0.19	0.09

Ion/Material	**1 MeV, 1e15**	**1 MeV, 2.2e15**	**1 MeV, 6e15**	**2 MeV, 3.9e13**	**2 MeV, 8e13**
Au^+ in GaSb	-	18.36	20.50	2.51	-
	-	18.26	20.37	2.50	-
	-	18.67	20.25	2.51	-
	-	18.31	20.19	2.60	-
	-	18.46	20.25	2.47	-
	-	18.31	20.25	2.50	-
	-	18.11	20.06	2.44	-
	-	18.41	20.06	2.46	-
	-	18.06	20.25	2.50	-
	-	18.41	20.25	2.54	-
	-	18.31	20.19	2.50	-
	-	19.43	20.06	2.52	-
	-	18.16	20.00	2.47	-
	-	18.46	20.12	2.52	-
	-	18.31	20.19	2.52	-
	-	18.11	20.12	2.56	-
	-	18.67	20.05	2.49	-
	-	18.31	20.04	2.40	-
	-	17.91	19.82	2.47	-
	-	18.41	20.19	2.45	-
	-	17.95	20.50	2.45	-
	-	18.36	20.19	2.49	-
	-	18.26	20.25	2.51	-
	-	18.67	20.25	2.51	-
	-	18.36	20.06	2.47	-
Average [um]	-	18.36	20.18	2.49	-

Variance:	-	0.09	0.02	0.00	-
Standard Dev.:	-	0.30	0.15	0.04	-

Ion/Material	**2 MeV, 1.4e14**	**2 MeV, 2.4e14**	**3 MeV, 5.1e13**	**3 MeV, 1e14**	**3 MeV, 2e14**
Au^+ in GaSb	4.30	6.69	3.80	7.87	8.32
	4.25	6.59	3.78	8.19	8.32
	4.20	6.59	3.78	8.22	8.19
	4.15	6.59	3.69	8.22	8.32
	4.00	6.56	3.80	8.07	8.49
	4.16	6.69	3.81	8.04	8.36
	4.23	6.59	3.80	7.94	8.42
	4.20	6.66	3.81	8.04	8.36
	4.06	6.46	3.67	8.07	8.36
	4.21	6.46	3.77	8.09	8.42
	4.15	6.56	3.72	7.92	8.52
	4.20	6.66	3.80	7.94	8.56
	4.26	6.59	3.75	7.97	8.46
	4.21	6.46	3.73	7.99	8.46
	4.25	6.63	3.72	7.97	8.52
	4.15	6.66	3.76	7.92	8.59
	4.28	6.63	3.77	8.02	8.49
	4.28	6.59	3.80	7.99	8.62
	4.10	6.56	3.69	7.97	8.56
	4.11	6.73	3.73	7.92	8.52
	4.18	6.49	3.71	8.02	8.39
	4.25	6.66	3.76	7.92	8.56
	4.20	6.66	3.73	8.07	8.36
	4.15	6.66	3.81	8.04	8.49
	4.15	6.66	3.78	7.94	8.16
Average [um]	4.19	6.60	3.76	8.01	8.43
Variance:	0.01	0.01	0.00	0.01	0.01
Standard Dev.:	0.07	0.08	0.04	0.09	0.12

Ion/Material	**1 MeV, 5e13**	**1 MeV, 1.25e14**	**1 MeV, 3e14**	**1 MeV, 6e14**	**1 MeV, 8.4e14**
Au^+ in InSb	1.81	4.50	8.45	16.01	20.47
	1.91	4.39	8.37	15.85	20.28
	1.82	4.36	8.52	15.85	20.66
	1.78	4.62	8.52	15.85	20.56
	1.89	4.31	8.24	15.80	20.28
	1.87	4.27	8.71	15.85	20.19
	1.87	4.45	8.33	15.61	20.00
	1.82	4.34	8.52	15.74	20.28
	1.83	4.37	8.52	16.06	20.56
	1.87	4.43	8.43	15.85	20.66
	1.82	4.64	8.52	15.85	20.47
	1.88	4.34	8.43	15.85	20.19
	1.84	4.34	8.33	15.74	20.47
	1.87	4.70	8.52	15.69	20.75
	1.78	4.44	8.05	15.85	20.47
	1.85	4.46	8.24	15.90	19.91

	1.84	4.38	8.33	16.01	20.28
	1.90	4.45	8.43	15.90	20.75
	1.78	4.50	8.33	15.74	19.89
	1.83	4.38	8.52	15.58	20.28
	1.87	4.43	8.14	15.64	20.19
	1.85	4.50	8.33	15.58	20.37
	1.79	4.40	7.95	15.53	20.19
	1.78	4.45	8.24	15.64	20.19
	1.86	4.62	8.14	15.80	20.09
Average [um]	1.84	4.44	8.37	15.79	20.34
Variance:	0.00	0.01	0.03	0.02	0.06
Standard Dev.:	0.04	0.11	0.17	0.14	0.24

Ion/Material	**2 MeV, 5e13**	**2 MeV, 1.2e14**	**2 MeV, 2e14**	**3 MeV, 5e13**	**3 MeV, 1e14**	**3 MeV, 2e14**
Au^+ in InSb	1.36	8.66	14.48	5.57	11.50	19.00
	1.35	8.56	14.70	5.30	11.75	18.50
	1.35	8.61	13.77	5.52	11.75	18.75
	1.32	8.77	13.77	5.42	11.75	19.12
	1.31	8.39	14.20	5.53	11.37	18.87
	1.33	8.45	13.27	5.44	12.37	18.50
	1.34	8.56	13.56	5.43	11.75	19.25
	1.35	8.66	14.41	5.43	12.13	19.25
	1.32	8.61	13.84	5.32	11.63	18.75
	1.30	8.66	13.84	5.38	11.50	18.75
	1.31	8.66	13.56	5.58	12.37	18.75
	1.30	8.61	13.56	5.72	11.63	19.50
	1.31	8.61	13.56	5.28	11.87	18.58
	1.35	8.66	13.91	5.65	11.50	19.00
	1.34	8.77	13.56	5.77	11.75	19.30
	1.31	8.39	13.91	5.66	12.25	18.75
	1.41	8.56	14.34	5.71	12.13	19.37
	1.40	8.66	13.91	5.37	11.50	19.00
	1.41	8.61	13.99	5.64	11.63	18.37
	1.42	8.56	14.13	5.61	11.87	19.12
	1.40	8.45	14.13	5.41	12.13	19.50
	1.38	8.61	14.41	5.36	11.37	18.87
	1.39	8.45	13.77	5.52	11.75	18.25
	1.43	8.66	14.20	5.34	11.75	19.12
	1.44	8.56	13.27	5.45	11.66	18.87
Average [um]	1.36	8.59	13.92	5.50	11.79	18.92
Variance:	0.00	0.01	0.14	0.02	0.08	0.11
Standard Dev.:	0.04	0.10	0.38	0.14	0.29	0.34

Ion/Material	**280 keV, 8e18, 450°C**	**280 keV, 2e18, 650°C**	**280 keV, 8e18, 650°C**
Si^+ in Si	0.49	1.24	1.31
	0.40	1.27	1.26
	0.21	1.23	1.25
	0.23	1.20	1.27

	0.22	1.13	1.25
	0.21	1.23	1.33
	0.36	1.15	1.33
	0.32	1.15	1.29
	0.46	1.14	1.27
	0.59	1.15	1.37
	0.45	1.04	1.30
	0.29	0.97	1.27
	0.20	0.92	1.23
	0.17	0.88	1.18
	0.18	0.94	1.25
	0.40	1.02	1.22
	0.36	0.93	1.20
	0.28	0.88	1.12
	0.26	1.03	1.27
	0.26	1.09	1.25
	0.41	0.97	1.27
	0.69	1.03	1.25
	0.59	1.24	1.23
	0.54	1.14	1.24
	0.47	1.07	1.18
Average [um]	0.36	1.08	1.25
Variance:	0.02	0.02	0.00
Standard Dev.:	0.15	0.12	0.05

Appendix 3

Analysis of GaSb Surface Layers at Increasing Ion Fluence

In Section 4.1.2, the GaSb surface layer is analyzed in Figure 4.4 as a function of ion fluence following 1 MeV Au^+ irradiation. While the images shown in Figure 4.4 were chosen to show the various features observed at each ion fluence, the images do not all fully reveal the overall surface morphology of the samples. Here, additional SEM images and analysis are included to better describe the overall irradiated surface.

Initially, the GaSb surface is shown to exhibit small breaks in the surface at an ion fluence of 1×10^{14} ions/cm^2, as shown in Figure 4.4a. Figure A3.1 shows a lower magnification SEM image of the same surface. The surface breaks are quite visible and clearly tend to be long and straight, but the majority of the surface appears to be flat and featureless. With an increase in fluence to 4×10^{14} ions/cm^2, larger openings appear in the sample surface. Figures 4.4b and 4.4c focus on small-scale breaks in the surface, to illustrate the interface between the fibers, surface, and void space. Figures A3.2 and A3.3 show lower magnification images of the surface, showing that, in general, the surface removal is fairly widespread, though the size of surface openings varies dramatically, from gaps of several hundred nanometers in length to well over 1 mm. With an additional increase in ion fluence to 6×10^{14} ions/cm^2, the surface is almost entirely removed, as shown in Figure 4.4d and in greater scope in Figure A3.4. Eventually, the surface is

removed entirely, as shown in Figures 4.4e and 4.4f, which accurately represent the overall surface morphology of samples irradiated to a fluence of 6×10^{15} ions/cm^2.

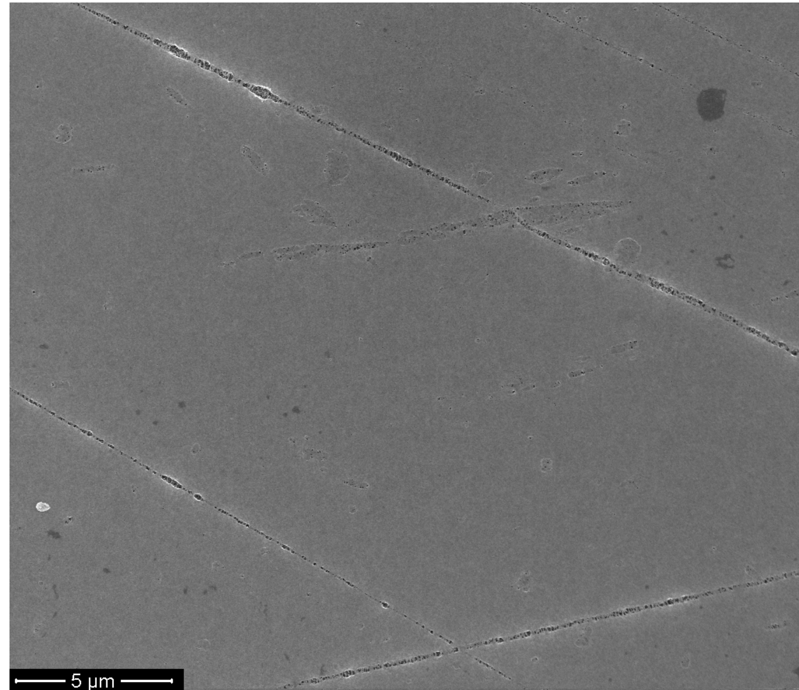

Figure A3.1. Plan-view SEM image of GaSb irradiated with 1 MeV Au^+ to an ion fluence of 1×10^{14} ions/cm^2.

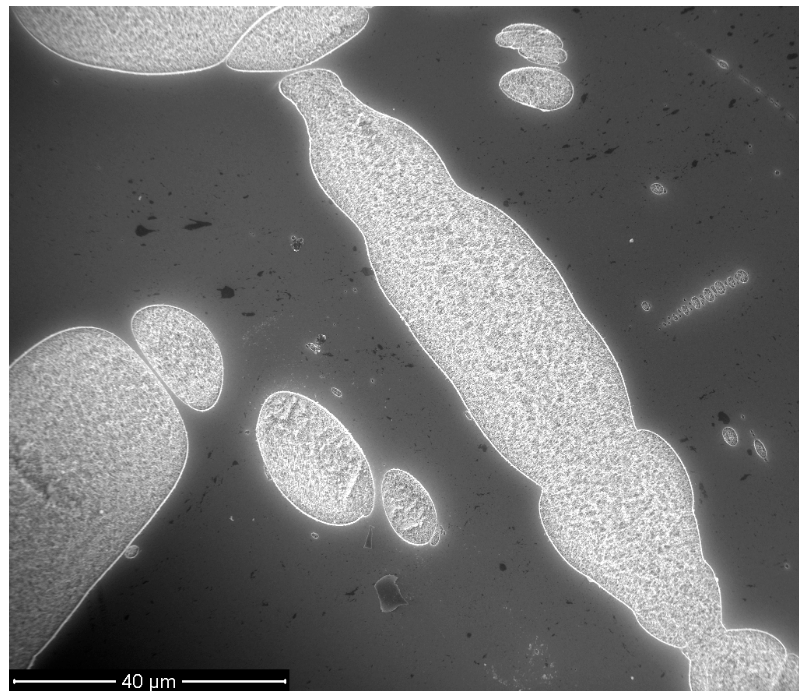

Figure A3.2. Plan-view SEM image of GaSb irradiated with 1 MeV Au^+ to an ion fluence of 4×10^{14} ions/cm^2.

Figure A3.3. Plan-view SEM image of GaSb irradiated with 1 MeV Au^+ to an ion fluence of 4×10^{14} ions/cm^2.

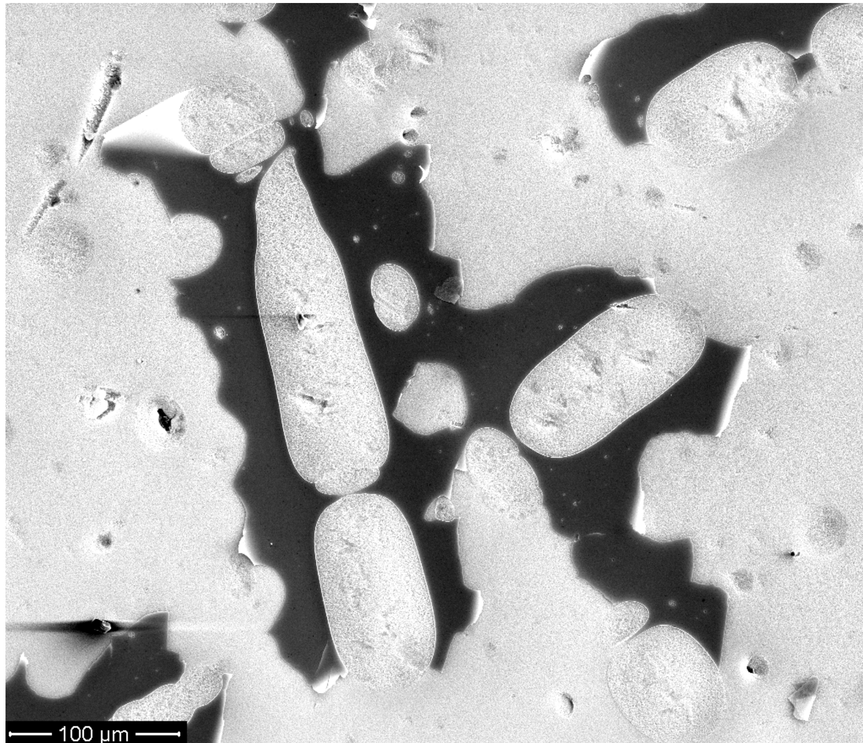

Figure A3.4. Plan-view SEM image of GaSb irradiated with 1 MeV Au^+ to an ion fluence of 6×10^{14} ions/cm^2.

Appendix 4

Surface Roughness Measurements of Ion Irradiated InSb

In Section 6.1.2, Figure 6.8 shows the porous layer thickness, t, compared to the surface roughness, R_t, of high-energy Au^+ irradiated InSb samples. R_t is defined as R_p-R_v, where R_p is the maximum peak height and R_v is the maximum valley depth of peaks and valleys in the irradiated sample surface. Measurements for t, R_p, and R_v were made from XSEM images of the samples. Here, the data sets from the analyzed samples are included, along with the average, variance, and standard deviation of each data set. As R_t is a function of R_p and R_v, its standard deviation is taken as the larger of either R_p or R_v.

InSb	Rp [um]	Rv [um]	t [um]
2 MeV, 5e13	1.360	1.338	1.360
	1.356	1.347	1.353
	1.356	1.319	1.347
	1.353	1.319	1.322
	1.360	1.319	1.313
	1.341	1.297	1.331
	1.350	1.306	1.338
	1.363	1.313	1.353
	1.338	1.313	1.320
	1.335	1.306	1.303
	1.400	1.400	1.313
	1.426	1.400	1.303
	1.426	1.384	1.313
	1.434	1.384	1.347
	1.426	1.376	1.344
	1.434	1.392	1.309
	1.434	1.376	1.409
	1.417	1.384	1.400
	1.442	1.400	1.409
	1.442	1.392	1.417

	1.400	1.400	1.400
	1.426	1.384	1.376
	1.426	1.392	1.392
	1.409	1.376	1.426
	1.417	1.367	1.442
	1.417	1.351	1.392
	1.400	1.367	1.434
	1.400	1.342	1.392
	1.409	1.353	1.398
	1.434	1.384	1.384
	1.441	1.392	1.394
Average [um]:	1.399	1.360	1.366
Variance:	0.001	0.001	0.002
Standard Deviation:	0.036	0.034	0.043

InSb	Rp [um]	Rv [um]	t [um]
1 MeV, 5e13	1.979	1.812	1.808
	1.950	1.795	1.912
	1.921	1.791	1.816
	1.963	1.762	1.783
	1.917	1.757	1.887
	1.921	1.766	1.870
	1.896	1.691	1.875
	1.938	1.804	1.820
	1.938	1.779	1.829
	1.942	1.770	1.875
	1.904	1.816	1.825
	1.917	1.745	1.883
	1.938	1.820	1.841
	1.938	1.787	1.866
	1.925	1.790	1.783
	1.893	1.742	1.851
	1.917	1.801	1.842
	1.909	1.809	1.901
	1.884	1.809	1.776
	1.926	1.809	1.826
	1.942	1.759	1.867
	1.909	1.751	1.851
	1.909	1.801	1.792
	1.909	1.759	1.784
	1.934	1.767	1.859
	1.926	1.801	1.843
	1.884	1.776	1.793
	1.851	1.842	1.893
	1.901	1.801	1.851
	1.901	1.767	1.801
	1.893	1.794	1.859
Average [um]:	1.918	1.783	1.841

Variance:	0.001	0.001	0.001
Standard Deviation:	0.026	0.030	0.038

InSb	Rp [um]	Rv [um]	t [um]
1 MeV, 1.25e14	4.510	4.026	4.502
	4.585	4.085	4.393
	4.635	3.852	4.360
	4.455	4.077	4.620
	4.493	3.927	4.310
	4.335	4.118	4.268
	4.560	4.052	4.452
	4.570	4.043	4.343
	4.710	4.002	4.369
	4.643	3.827	4.427
	4.497	3.576	4.643
	4.519	3.864	4.343
	4.660	3.785	4.343
	4.702	3.868	4.702
	4.444	3.921	4.444
	4.477	3.851	4.460
	4.516	3.900	4.383
	4.432	3.849	4.449
	4.599	3.733	4.500
	4.299	3.916	4.383
	4.383	3.916	4.432
	4.432	3.650	4.500
	4.432	3.999	4.402
	4.533	3.967	4.449
	4.449	3.766	4.616
	4.417	3.999	4.516
	4.466	3.982	4.333
	4.533	3.750	4.567
	4.666	3.883	4.338
	4.650	3.883	4.368
	4.599	3.849	4.516
Average [um]:	4.523	3.901	4.443
Variance:	0.011	0.016	0.011
Standard Deviation:	0.105	0.127	0.106

InSb	Rp [um]	Rv [um]	t [um]
3 MeV, 5e13	5.649	4.833	5.566
	5.649	4.417	5.300
	5.583	4.449	5.516
	5.533	4.700	5.416
	5.666	4.666	5.533
	5.649	4.316	5.436
	5.533	5.083	5.433
	5.400	5.017	5.433

	5.450	4.446	5.317
	5.550	5.161	5.383
	5.716	4.798	5.583
	5.383	4.572	5.716
	5.332	4.644	5.283
	5.416	4.626	5.649
	5.750	4.803	5.767
	5.714	4.356	5.660
	5.714	4.340	5.714
	5.410	4.626	5.374
	5.732	4.626	5.642
	5.714	4.250	5.608
	5.500	4.356	5.410
	5.161	4.911	5.356
	5.500	4.677	5.518
	5.418	4.608	5.338
	5.536	4.590	5.446
	5.590	4.428	5.595
	5.446	4.749	5.608
	5.467	4.770	5.613
	5.696	4.600	5.238
	5.410	4.358	5.503
	5.500	5.014	5.374
Average [um]:	5.541	4.638	5.494
Variance:	0.020	0.057	0.020
Standard Deviation:	0.142	0.239	0.142

Appendix 5

Power Spectral Density Data Acquisition

Included in this appendix is the Matlab computer code used to obtain plots shown in Figure 6.9. The code takes an input of a plan-view SEM image of the irradiated InSb surface, completes a fast Fourier transform of the image, and calculates PSDs from the data. Plots are the direct output of the code; raw data is not outputted.

Matlab code:

```
Y=fft2(x520);
qw=Y.*conj(Y);
r=1:400;
pr=zeros(1,400);
n=zeros(1,400);
for kx=1:400
   for ky=1:400
      for k=1:400
         if(k==floor(sqrt(kx^2+ky^2)))
            pr(k)=pr(k)+qw(kx,ky);
            n(k)=n(k)+1;
         end
      end
   end
end
prr=pr./n;
loglog((5:400)/5000,prr(5:400))
```